OPERABILITY AND PERFORMANCE OF ROTATING DETONATION ENGINES

by

Ian V. Walters

A Dissertation

Submitted to the Faculty of Purdue University

In Partial Fulfillment of the Requirements for the degree of

Doctor of Philosophy

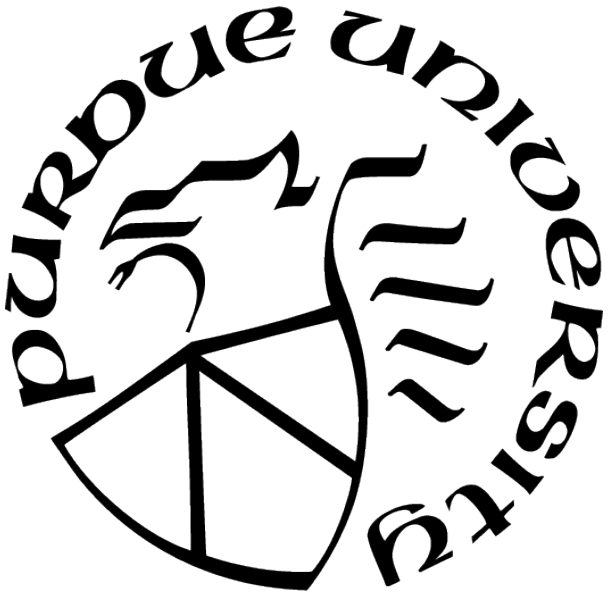

School of Aeronautics and Astronautics

West Lafayette, Indiana

August 2021

THE PURDUE UNIVERSITY GRADUATE SCHOOL
STATEMENT OF COMMITTEE APPROVAL

Dr. Carson D. Slabuagh, Chair

School of Aeronautics and Astronautics

Dr. Rohan M. Gejji

School of Aeronautics and Astronautics

Dr. Stephen D. Heister

School of Aeronautics and Astronautics

Dr. Timothée L. Pourpoint

School of Aeronautics and Astronautics

Dr. Carlo Scalo

School of Mechanical Engineering

Approved by:

Dr. Gregory A. Blaisdell

To my wife Madeline

ACKNOWLEDGMENTS

I first want to express my sincere gratitude to my advisor Prof. Carson Slabaugh for the opportunity to join his research group and work on a fascinating project. Contributing to the development of a new (credible) thermodynamic cycle is rare opportunity that I have greatly enjoyed. An internship coworker was prescient in his warning that it is easy to start having fun as a Masters student and unwittingly end up with a doctorate. However, this still would not have been possible without Prof. Slabaugh's willingness to let me continue my work remotely for the second half of my program. For that, I will be forever grateful. I further thank him for his support and guidance, despite my occasional obstinance and favored role of provocateur in design reviews.

I have also appreciated the guidance and encouragement from Prof. Steve Heister. Though he claims to be most useful as a cheerleader on experiments, his unique insights into the underlying physics, frequent role as an internal reviewer of my work, and reminders to not lose sight of the end goal of advancing the technology to the engine have proved invaluable. I greatly appreciate the assistance of Prof. Carlo Scalo in the modeling component of this work and have benefited immensely from his expertise and patience when working with an experimentalist on simulations. I also thank Prof. Timothée Pourpoint for persistent reminders to remember the fundamentals, whether in class or committee.

Dr. Rohan Gejji has gone above and beyond the expectations of a committee member and colleague, providing immense help in all stages of research, serving as a sounding board for ideas (and complaints), and letting me crash at his house during visits. I am thankful for his friendship throughout this endeavor.

Special thanks are accorded to the Zucrow staff members, particularly Scott Meyer for managing the chaos of lab with his own special brand thereof, Andrew Pratt for his contributions to experiment and facility development, and Rob McGuire for bailing me out from poor design and planning more times than I can count.

I am particularly grateful to the Slabaugh research group members for the support and collegiality over the years, and for continuing to include me as I worked remotely. Their friendship has made school and research much more enjoyable. Regional trips and late

nights testing, playing games, and commiserating with John Philo, Dr. Timo Buschhagen, Jenna Humble, Mark Frederick, Alexis Harroun, Kyle Schwinn, Aaron Lemcherfi, Ethan Plaehn, Dr. David Stechmann, Dr. Brandon Kan, Dr. Robert Zhang, and Dr. Dasheng Lim are not to be forgot.

Finally, I would like to thank my family, and particularly my wife, Madeline. Her inexhaustible support and encouragement have been foundational, and her immense patience despite my frequent aloofness is to be commended.

TABLE OF CONTENTS

LIST OF TABLES

LIST OF FIGURES

LIST OF SYMBOLS

A	combustor cross-sectional area, m^2
c_p	specific heat, $J/(kg \cdot K)$
CR	backpressure nozzle contraction area ratio
EAP	Equivalent Available Pressure, MPa
F, F_g	gross thrust (corrected for base pressure), kN
F_B	combustor bluff body base drag, kN
G	mass flux, $kg/(m^2 \cdot s)$
k	pressure decay time constant, s^{-1}
M	Mach number
$\dot{m}$	mass flowrate, kg/s
MW	molecular weight, $kg/kmol$
p_c	mean chamber pressure, MPa
p'	mean chamber pressure fluctuation amplitude, MPa
p	pressure, MPa
R	specific gas constant, $J/(kg \cdot K)$
R_u	universal gas constant, $J/(kmol \cdot K)$
T	temperature, K
T_3	combustor inlet temperature, K
u	flow velocity, m/s
V_z	axial velocity, m/s
V_θ	azimuthal velocity, m/s
$Y_{O_2}^{Ox}$	mass fraction of oxygen in oxidizer
$Y_{H_2}^{F}$	mass fraction of hydrogen in fuel
$r - z - \theta$	global, RDE coordinate system
$x - y$	local, PIV coordinate system
γ	ratio of specific heats
θ_+/θ_-	$+/-\theta$ propagating wave location
θ_{CA}	counter-rotating wave mode cycle phase angle

θ_{AA}	counter-rotating wave mode annulus phase angle
λ	detonation cell size
ϕ	equivalence ratio

Subscripts

ad	adiabatic flame condition
CJ	Chapman-Jouguet
e	combustor exit plane
P	products
R	reactants
$t, 0$	total
∞	ambient
3	reactant manifold
3.1	reactant injection throat
3.2	pre-combustion
4	post-combustion
8	nozzle exit throat

ABSTRACT

Rotating Detonation Engines (RDEs) provide a promising avenue for reducing greenhouse gas emissions from combustion-based propulsion and power systems by improving their thermodynamic efficiency through the application of pressure-gain combustion. However, the thermodynamic and systems-level advantages remain unrealized due to the challenge of harnessing the tightly coupled physics and nonlinear detonation dynamics inherent to RDEs, particularly for the less-detonable reactants characteristic of applications. Therefore, a RDE was developed to operate with natural gas and air as the primary reactants at elevated chamber pressures and air preheat temperatures, providing a platform to study RDEs with the less-detonable reactants and flow conditions representative of land-based power generation gas turbine engines. The RDE was tested with two injector configurations in a broad, parametric survey of flow conditions to determine the effect of operating parameters on the propagation of detonation waves in the combustor and delivered performance. Measurements of chamber wave dynamics were performed using high-frequency pressure transducers and high-speed imaging of broadband combustion chemiluminescence, while thrust measurements were used to characterize the work output potential.

The detonation dynamics were first studied to characterize RDE operability for the target application. Wave propagation speeds of up to 70% of the mixture Chapman-Jouguet detonation velocity and chamber pressure fluctuations greater than 4 times the mean chamber pressure were observed. Supplementing the air with additional oxygen, varying the equivalence ratio, and enriching the fuel with hydrogen revealed that combustor operability is sensitive to the chemical kinetics of the reactant mixture. While most test conditions exhibited counter-rotating detonation waves within the chamber, one injector design was able to support single wave propagation. A thermodynamic performance model was developed to aid analysis of RDE performance by making comparisons of net pressure gain for identical flow conditions. While the injector that supported a single wave operating mode better followed the trends predicted by the model, neither injector achieved the desire stagnation pressure gain relative to the reactant manifold pressure. Application of the model to a generic RDE revealed the necessity of normalizing any RDE performance parameter by the driving sys-

tem potential and identified the area ratio between the exhaust and injection throats as the primary parameter affecting delivered pressure gain. A pair of test conditions with distinct wave dynamics were selected from the parametric survey to qualitatively and quantitatively analyze the exhaust flow using high-speed particle image velocimetry. A single detonation wave with an intermittent counter-rotating wave was characterized in the first test case, while a steady counter-rotating mode was studied in the second. The velocity measurements were phase averaged with respect to the instantaneous wave location to reveal contrasting flowfields for the two cases. The total pressure and temperature of flow exiting the combustor were computed using the phase-resolved velocity measurements along with the measured reactant flowrate and thrust to close the global balance of mass and momentum, providing an improved method of quantifying RDE performance. Finally, a reduced order model for studying RDE operability and mode selection was developed. The circumferential detonation wave dynamics are simulated and permitted to naturally evolve into the quasi-steady state operating modes observed in RDEs. Preliminary verification studies are presented and areas for further development are identified to enable the model to reach a broader level of applicability.

The experimental component of this work has advanced understanding of RDE operation with less-detonable reactants and developed improved methods for quantifying RDE performance. The accompanying modeling has elucidated the design parameters and flow conditions that influence RDE performance and provided a framework to investigate the factors that govern RDE mode selection and operability.

1. INTRODUCTION

1.1 Motivation

Development of efficient energy conversion systems that produce minimal greenhouse gases and pollution remains a principal challenge of modern engineering. The 2020 National Academies of Science, Engineering, and Medicine report, *Advanced Technologies for Gas Turbines*, projects that electrical power demand will grow by 50% in the next two decades [1]. Furthermore, the total number of commercial aircraft is predicted to double in this same timeframe. Despite significant reductions in the cost of wind and solar photovoltaic power generation and correspondingly increased rates of adoption, it is unlikely that these renewable energy sources will be able to meet the growing, global energy demand. A complete transition to entirely renewable energy sources may prove difficult, as electricity storage technologies are unable to provide the requisite storage capacity or density. Future energy strategy will necessarily use renewable sources in concert with combustion systems, which satisfy these requirements and benefit from existing infrastructure. For example, renewable energy sources may be used to generate hydrogen or synthetic hydrocarbons, which can be used for energy storage and subsequently burned in a combustion system [1]. The projection of Fig. 1.1 confirms the continued role of combustion technologies, and indicates that they will remain a significant component of the global energy mix, with expected growth of 20%. It is therefore necessary to optimize combustion-based energy conversion technologies to achieve the objectives of efficiency and cleanliness.

Modern propulsion and power systems, such as gas turbine and rocket engines, have achieved high combustion and overall thermal efficiencies as a result of decades of incremental development and engineering such that few opportunities remain for significant improvements. As a result, the gas turbine combined cycle power plant is the most efficient energy conversion system, with modern systems approaching 65% overall efficiency [1]. That is, greater than 60% of the chemical energy contained within the fuel is converted to electricity delivered to an outlet. The progression of research, development, and deployment over the past 5 decades is illustrated in Fig. 1.2. The bottom panel displays the steady increase in combined cycle efficiency, which has begun to approach a plateau near the noted 65%.

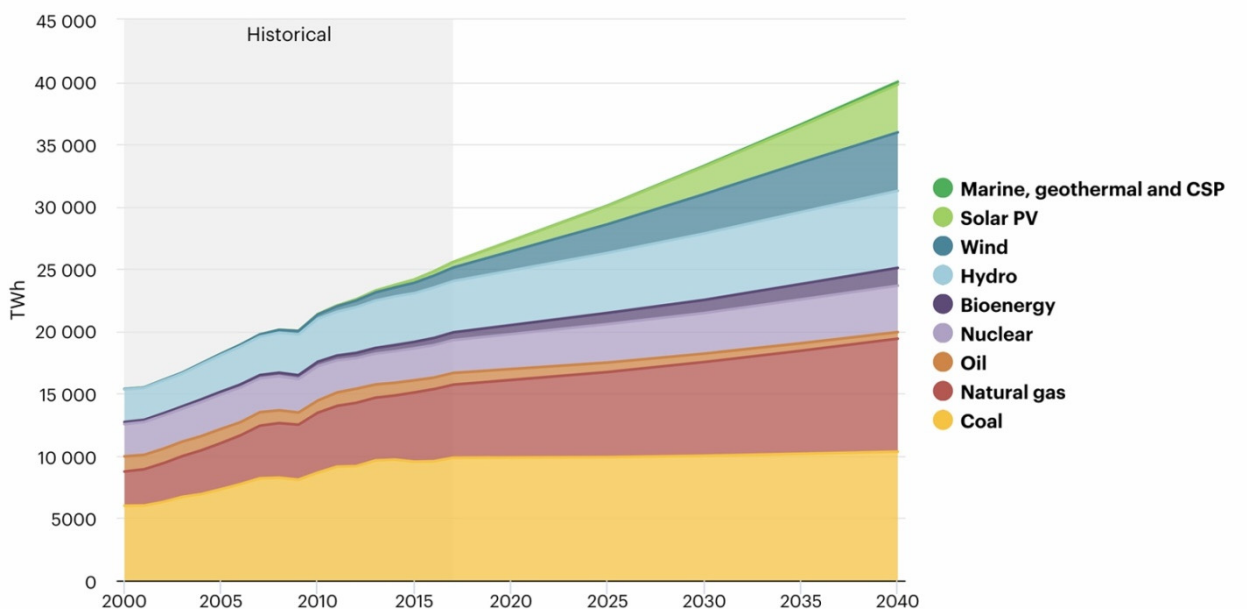

Figure 1.1. Historical global electricity generation and New Policies Scenario projection from International Energy Agency categorized by technology [1].

However, further improvements are critical in achieving the desired reductions in greenhouse gas emissions, given the continued growth of gas turbines for power generation shown by the growth in electricity generated using natural gas in Fig. 1.1. Gas turbine engines currently comprise one-third of energy generation capacity in the United States, such that an efficiency gain of 1% produces a reduction in emissions equivalent to installing tens of thousands of wind turbines [1]. The *Advanced Technologies for Gas Turbines* report therefore sets a goal of increasing the efficiency of combined cycle power plants to 70% by 2030, and 50% for simple cycles [1].

Historically, combined cycle efficiency gains have largely been enabled by steady increases in the allowable temperature of combustion gases entering the first stage of the turbine, the turbine inlet temperature, illustrated in the top panel of Fig. 1.2. While the efficiency of an ideal Brayton cycle is typically set by the pressure ratio, increasing the gas turbine pressure ratio in a combined cycle power plant reduces the power output of the bottoming steam cycle, elevating the importance of the turbine inlet temperature [1]. The top panel of Fig. 1.2 also identifies the contributions of specific technologies towards increases in turbine inlet temperature. The improvements, and hence improvements in gas turbine efficiency, have

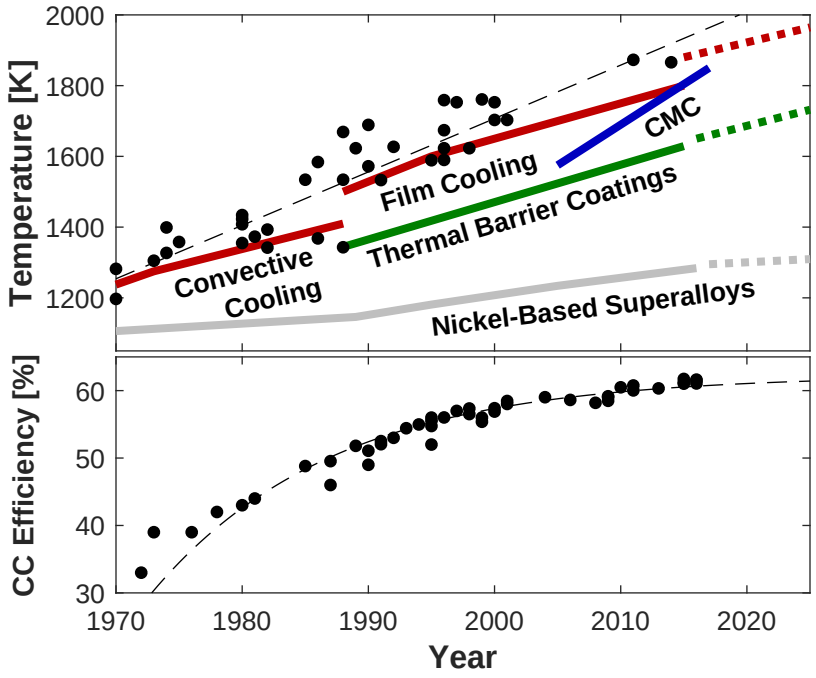

Figure 1.2. Evolution of gas turbine combined cycle turbine inlet temperature and efficiency over time.

principally been enabled by advances in turbine blade thermal management and materials science. Despite this emphasis, combustion remains the primary source of entropy generation within gas turbines. Textbook exergetic analysis indicates that 30% of the fuel exergy is destroyed during combustion in a combined cycle power plant, twice as much as is destroyed in all other major components combined. Therefore, future gas turbine systems could benefit immensely from the development of combustion technologies that reduce this dominant loss mechanism. The *Advanced Technologies for Gas Turbines* report addresses this by identifying "unconventional thermodynamic cycles" as one area of research that may be necessary to achieve the stated objective of 70% combined cycle and 50% simple cycle efficiency [1]. Of the technologies identified in the report, Pressure Gain Combustion most directly addresses the noted deficiencies of combustion in propulsion and power applications. Pressure Gain Combustion (PGC) is an unsteady process wherein gas expansion is constrained during heat addition to produce a total pressure rise, which corresponds with increased energy availability or decreased entropy generation. By directly addressing the dominant source

of exergy destruction in gas turbines, PGC could provide a step-change advance in cycle efficiency and jump above the trendline of Fig. 1.2.

1.2 Background

In a typical gas turbine or rocket combustor, the reaction front proceeds as a deflagration, which propagates at a subsonic velocity through the diffusion of heat and intermediate chemical species. The process is classified as constant pressure combustion, though in practice it produces a total pressure loss across the combustor. In contrast, combustion in PGC systems either occurs at constant volume to produce a pressure rise, or via a detonation wave. Detonation waves are a shock-coupled reaction front where the pressure and temperature rise from a leading shock causes the reactant mixture to autoignite after a short induction period. The expansion due to heat addition then provides the thrust necessary to support the leading shock. The dominant physical mechanisms in a detonation are then advection and reaction chemistry, producing combustion fronts that propagate between 1-3 km/s in gaseous mixtures [2]. A timescale disparity between the reaction chemistry and gas expansion processes constrains the reactions such that they effectively occur at constant volume conditions. Hence the desired total pressure increase is achieved, so long as the detonation is not stationary in the reference frame of the propulsion or power device [3].

While a range of PGC technologies have been proposed, including wave rotor combustors [4], pulse jets, and Pulse Detonation Engines (PDE) [5], [6], the Rotating Detonation Engine (RDE) [6]–[9] has emerged as the most promising architecture. Rotating detonation engines were initially studied in the late 1950s and early 1960s by Voitsekhovskii in Russia [10] and by Nicholls in the United States [11], but have become the focus of contemporary PGC research due to the perceived advantages over other concepts. In a RDE, one or multiple detonation waves propagate transverse to the flow of incoming reactants, commonly in an annular chamber. The noted ranges of detonation wave velocities (1-3 km/s) and typical research combustor diameters (0.05-0.3 m) result in wave circumscription frequencies that vary between 1-50 kHz. The concept then retains the fundamental unsteadiness characteristic of PGC devices, but the high cycle frequencies produce a quasi-steady flow that could

permit drop-in replacement of the combustor in existing engine architectures. The closed-loop geometry further requires a single ignition and deflagration-to-detonation transition during engine startup and is geometrically similar to existing combustor designs, mitigating disadvantages of other PGC systems.

A number of challenges remain before the distinct thermodynamic and system-level advantages of PGC as implemented using a RDE can be realized, many of which are related to the fundamental unsteadiness of the cycle. High pressures behind the detonation wave front locally modulate reactant injection as it circumscribes the combustion chamber and, at the extreme, induce backflow of combustion products into the injection system. The injection system dynamic response must then be tuned to introduce and mix sufficient fresh reactants prior to the arrival of the subsequent wave to sustain its propagation. The dynamic injection results in a highly turbulent, inhomogeneous flow field through which the detonation wave must propagate, far removed from the quiescent, homogeneous mixtures of classical detonation theory [2]. Rotating detonation engines are observed to operate in a number of different modes, defined by the number, direction, and strength of the detonation waves [9]. No reliable method for predicting the operating mode, and hence whether the combustor can operate at all, has been established. While RDEs are frequently considered quasi-steady devices due to natural aerodynamic valving of the inflow, the exhaust flow is highly unsteady and transonic, with shocks extending from the detonation front into the exhaust plume. This is likely to challenge integration efforts, as turbines and nozzles are traditionally designed for a steady inflow condition and fixed pressure ratio. Finally, research-grade RDEs typically operate with readily detonable reactants such as hydrogen-air or methane-oxygen with near-atmospheric mean chamber pressures. Extending RDE operation to reactants and operating conditions traceable to the intended applications remains challenging, particularly as applications often require less-detonable reactants. All of these challenges are exacerbated in low-loss designs required for a fielded system. As a result, no RDE in the open literature has achieved the desired stagnation pressure gain relative to the reactant supply.

1.3 Objectives

To begin addressing the challenges identified above, a combustor and associated test stand were developed with the goal of studying RDEs in the application of terrestrial power generation systems. Gas turbines for power production commonly use natural gas as their fuel, which presents challenges for RDEs because methane, the primary constituent, does not readily detonate in air. The combustor therefore serves as a platform for studying RDE operation with less-detonable reactants. Primary research objectives included assessing the ability of the combustor to operate across a wide range of flow conditions and quantifying the delivered performance in terms of the net stagnation pressure gain (or loss). The combustor was designed to operate with natural gas and air, mean chamber pressures up to 2.0 MPa, and air inlet temperatures of 700 K for traceability to the target application. The RDE was then tested in a broad, parametric survey of flow conditions and combustor geometry to identify the sensitivity of operability and performance to the selected parameters. The report of these efforts is structured as follows:

1. Chapter 2 first reviews the combustor design, including the development of two, distinct injector concepts. The operability is then assessed by considering the strength and consistency of detonation wave dynamics as the flow condition parameters are independently varied.

2. Chapter 3 focuses on the performance of rotating detonation engines. A thermodynamic model is formulated to identify which factors govern RDE performance and evaluate different approaches to its experimental quantification. The delivered combustor performance is next quantified using thrust measurements and compared to the model results across the same range of flow conditions studied in Chapter 2.

3. Chapter 4 analyzes the RDE exhaust plume flow and performance using high-speed Particle Image Velocimetry applied at the combustor exit plane. The velocity measurements are analyzed in conjunction with simultaneously-acquired pressure and imaging of the combustor annulus to examine the instantaneous and phase averaged flow dy-

namics. Finally, a framework for deriving quantitative performance estimates from the measurements that improves on the methods used in Chapter 3 is presented.

4. Chapter 5 develops a model for studying RDE operability. The reduced-order model tracks the circumferential detonation wave dynamics in a manner that permits natural evolution of the diverse wave modes observed in RDEs with sufficient fidelity to permit direct comparison with experiments. The model description and preliminary verification studies are presented.

5. Chapter 6 summarizes the key contributions of this research effort.

The insights gained from these efforts are expected to contribute to development of a RDE that demonstrates a positive net pressure gain.

2. OPERABILITY OF A NATURAL GAS-AIR ROTATING DETONATION ENGINE

This chapter has been previously published in the Journal of Propulsion and Power [12].
DOI: https://doi.org/10.2514/1.B37735

2.1 Introduction

Modern gas turbine engines are the result of decades of incremental technology development, resulting in few remaining opportunities for step-changes in engine performance. Development and adoption of pressure-gain combustion (PGC) systems provides a promising avenue for achieving this desired performance increase. State-of-the-art systems use constant pressure, deflagrative combustion, which results in a total pressure loss due to non-isentropic effects. A PGC device realizes a cycle-averaged total pressure increase by an unsteady combustion process where gas expansion is constrained during heat addition [13]. This results in a more efficient thermodynamic cycle as it produces greater energy availability for the same heat release [8], [14]. Detonation based combustion systems provide one method of attaining PGC because the chemical reactions occur faster than surrounding gas expansion. The timescale disparity results in combustion that is constrained and occurs at near-constant volume conditions. A detonation is also capable of providing higher rates of heat release because it propagates at velocities several orders of magnitude higher than a deflagration. Engine concepts that leverage these advantages will realize systems-level benefits via smaller combustors, in addition to efficiency gains.

The rotating detonation wave combustor (RDWC) configuration shows significant promise for realizing detonation-based PGC. In an RDWC, detonation waves are formed by a single deflagration-to-detonation transition during engine startup via direct initiation or by natural azimuthal instabilities in the combustor [15], [16]. One or more detonation waves then propagate transverse to the flow of incoming reactants, typically in an annular chamber. The configuration permits a quasi-steady flow device, where incoming reactants are naturally valved by high pressures behind the detonation wave. The RDWC features a conventional

feed system that relies on high injection pressure drops or fluidic valving (temporary cessation of injection due to the high pressure waveform) to permit operation at frequencies of order 1-10 kHz for airbreathing combustors. The quasi-steady flow due to high cycle frequencies and annular geometry eases integration with continuous flow turbomachinery systems and permits reuse of existing engine architectures.

Recent research has considered application of the RDWC to a range of propulsion systems, including turbojets, high speed air-breathing combustors, and rockets [7], [16]–[21]. However, these studies are typically conducted at laboratory-scale conditions and with propellant combinations that readily detonate, such as hydrogen or ethylene with air or methane with oxygen. There has been comparatively less investigation of RDWCs for land based power generation applications, where the poor detonability of the common propellant combination, natural gas and air, presents unique challenges.

Several researchers have recently worked to demonstrate RDWC operation with less detonable propellants relevant to power generation systems. Bykovskii [22]–[24] conducted an extensive study of airbreathing RDWC operation with syngas mixtures, with specific emphasis on combustor scaling. Further work with their 500 mm RDWC studied methane-hydrogen mixtures at pressures up to 1.5 MPa and found that hydrogen fractions greater than $Y_{H_2}^F = 30\%$ supported operation with continuous spinning detonation waves. However, decreasing the hydrogen content to $Y_{H_2}^F = 16\%$ resulted in waves propagating in both directions, referred to as a "Continuous Multifront Detonation," while further decreases resulted in external combustion. Roy *et al.* [25], [26] similarly studied natural gas-hydrogen airbreathing RDWC operation in a 150 mm combustor, but found it was only able to support detonation with $Y_{H_2}^F > 85\%$. While preheating the air to 480 K and operating at above-atmospheric chamber pressures of 0.3 MPa produced more robust operation, it failed to expand the range of operable natural gas concentrations. This was attributed to significant increases in the chemical induction time and thereby detonation cell size as the natural gas concentration increased, until the cells outgrew their combustor hardware scale. Given the limited scope of present research, there is a need to investigate operation of an RDWC with natural gas-air propellants at combustion chamber conditions relevant to land based power generation ($p_c = 1 - 2\ MPa,\ T_3 = 600 - 800\ K$) to explore the potential for this application.

Key obstacles to the realization of RDWC cycle benefits include nonideal detonation propagation, dynamic injection, unsteady mixing, and parasitic loss mechanisms. Development of design methodologies for scaling combustors from laboratory flow conditions and propellants to those found in gas turbine engines for power generation is currently intractable due to the nonlinear coupling between the injection fluid mechanics and reaction chemistry, which is highly sensitive to the geometry of the combustion device. It is therefore necessary to study RDWC systems with reactants and combustor operating conditions representative of this application, where demonstrating operation has remained challenging. The present study seeks to understand how the dynamic injection, mixing, and chemical kinetic processes that occur in RDWCs affect engine operation for the reactants and flow conditions of land-based power generation gas turbines. A combustor was developed to study detonation wave dynamics using a combination of integral and time-resolved techniques. Operability of the device was tested with natural gas and air propellants, chamber pressures up to 2 MPa, and air preheat temperatures up to 800 K.

2.2 Experiment Description

2.2.1 RDWC Test Article

A combustor was developed to demonstrate and investigate RDWC operation with natural gas and air propellants. The RDWC is designed to operate with a mean chamber pressure up to 2 MPa and permits variation of propellant flowrates, stoichiometry, propellant types, system backpressure, and air pre-heat temperature up to 800 K. The combustor geometry is depicted in the cross sectional view of Fig. 2.1. The combustion chamber outside diameter is 228 mm, the annular gap is 19 mm, and the length is 130 mm. The combustor was tested with two distinct injector designs. In both configurations, the oxidizer is fed axially through a slot at the head end of the chamber, while fuel is injected from orifices downstream of the oxidizer throat. Further details of the injection system are discussed in Section 2.2.3.

A thrust stand with requisite propellant supply systems was installed at the Maurice J. Zucrow Laboratories [27], [28] to provide a test platform for the combustor. The test platform can supply up to 10 kg/s of non-vitiated, heated air to the test article with com-

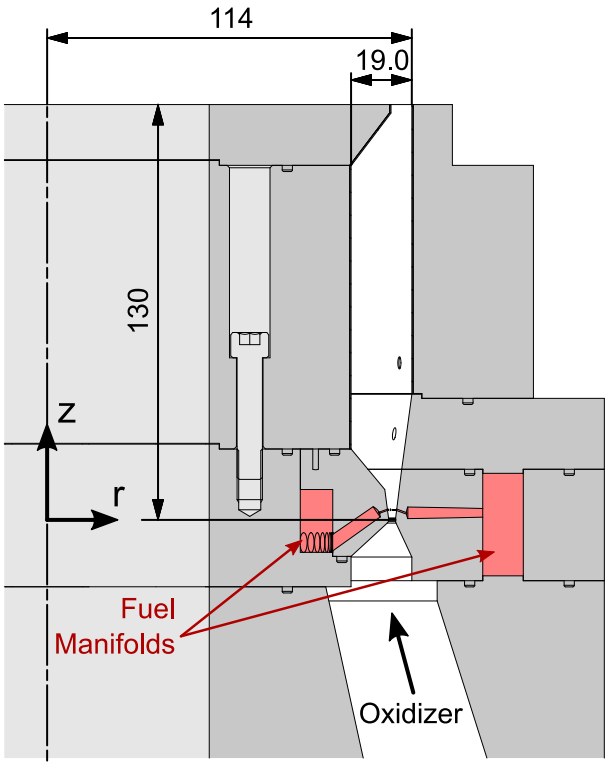

Figure 2.1. Cross section of RDWC test article with major dimensions labeled (in mm).

mensurate flows of natural gas, gaseous oxygen, nitrogen, cooling water, and other gaseous fuels. Oxygen can be independently injected into the air flow to increase the mass fraction of oxygen in the oxidizer flow, $Y_{O_2}^{Ox}$, from 23.2% (air) to 40%. Increasing the oxygen content of the oxidizer can be necessary to increase the range of operability for less detonable propellants. Natural gas is sourced from a local pipeline, while oxygen and other gaseous fuels are supplied by manifolds of high-purity cylinders. The natural gas composition is taken as a monthly average of the mole fraction of major species reported by the distributor (CH_4 92.4%, C_2H_6 6%, N_2 1%, CO_2 0.3%, C_3H_8 0.3%) [29].

The mass flow rates of fuel and oxidizer are metered by critical flow venturi nozzles (CFVNs) that conform to ISO specifications [30]. Upstream pressure and temperature are monitored throughout each test to compute mass flow rates. The pressure ratio across each CFVN is typically high enough to maintain a choked condition, but a throat pressure tap is also installed to CFVNs at risk of unchoking to permit calculation of mass flow rates at all conditions. The thermophysical properties of all fluids were computed using the NIST

Reference Fluid Thermodynamic and Transport Properties Database (REFPROP) [31]. This permits a fully real-gas treatment for computation of mass flow rates, acoustic velocities, and other thermodynamic data. Natural gas was treated as a mixture of the above constituents for both flowrate and stoichiometry calculations.

Uncertainty of mass flow rates, and subsequently operating conditions, are computed using the Kline-McClintock method of uncertainty propagation [32]. Error analysis included precision and bias of flow measurements, as well as uncertainty of natural gas composition, CFVN throat diameter, computed CFVN discharge coefficient, and critical flow function. Total uncertainty of each mass flow rate is approximately 0.8% with a 95% confidence interval. This results in a typical uncertainty in operating conditions of 0.5% of mass flux, 0.9% of equivalence ratio, and 0.1% of mass fraction of oxygen in the main oxidizer flow.

A pre-detonator device generates a detonation wave which is injected into the chamber and initiates combustion of the main propellants [33]. The pre-detonator feeds hydrogen and oxygen through a 4.6 mm tube closed at its head end by a spark plug. Spark discharge initiates a combustion front which then transitions to a detonation wave via a Shchelkin spiral integral to the tube wall. After a short, chaotic transient, limit-cycle operation establishes with one or more rotating detonation heads in the main combustor. Propellant flows are established prior to ignition to reduce transient effects of valve actuation, regulator response, and manifold priming. Combustion is terminated by replacing the fuel flow with an inert gas purge. Without active cooling measures, the test duration is limited to approximately 1 s because of the high thermal power density.

2.2.2 Cell Size Analysis

The propellant combination of natural gas-air presents unique challenges for use in an RDWC because the primary fuel constituent, methane, is difficult to detonate due to slow combustion kinetics that result in a large detonation cell size. As shown in Fig. 2.2, the detonation cell size of methane, denoted λ, is approximately 300 mm at atmospheric pressure and temperature. The detonation cell size has been widely used in RDWC preliminary design and interpretation of test results, where common heuristic design guidelines dictate that the

cell size serves as a minimum characteristic dimension of an RDWC chamber [7], [16], [26], [34]. However, cell sizes are based on measurements of detonation propagation through perfectly premixed reactants with idealized boundary conditions, while a detonation in an RDWC propagates through highly turbulent reactants with strong mixture fraction gradients and ill-defined boundary conditions. It is then unclear whether cell-forming transverse waves exist in an RDWC. As a result, their role in supporting propagation of the detonation front and the applicability of the cell size as a scaling parameter is not apparent.

Despite the differences in flow physics and boundary conditions between canonical configurations and RDWCs, several experiments have observed trends in combustor operability with cell size [7], [26], [34], which suggests that application of the cell size may still provide insight as an approximate scaling parameter. Prior studies in detonation channels have shown that the transverse waves in a cellular detonation front facilitate propagation of unstable detonations [2], [35]. The complex flow field found in RDWCs will inevitably produce an unstable detonation, which suggests that the transverse waves may still play a role. With this view of the detonation cell size as an approximate scaling parameter, it remains clear that a natural gas-air combustor requires operation at high pressures and temperatures to permit reasonably sized hardware.

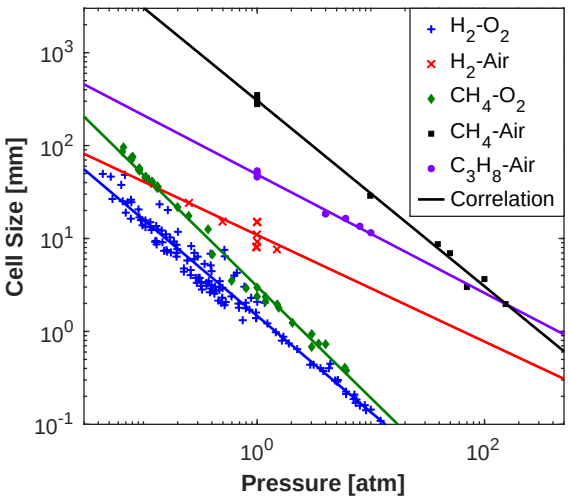

Figure 2.2. Detonation cell size data for several propellant combinations showing variation with respect to pressure for constant temperature and mixture fraction.

A correlation was developed to estimate the cell size dependence on pressure, temperature, and oxygen mass fraction using available data for the methane-oxygen-nitrogen system [36]–[39]. The correlation facilitates combustor sizing and will subsequently be used to investigate the importance of detonation cell size on RDWC operation. The correlation is given as

$$\lambda = (3.05\text{mm}) \exp\left(\frac{2\beta}{1.219 + 0.11\beta}\right) \left(\frac{P}{1\text{atm}}\right)^{\frac{\beta - 22.56}{18.8}} \left(\frac{T}{300\text{K}}\right)^{-1}, \tag{2.1}$$

where β is the number of moles of nitrogen per mole of oxygen in the mixture ($\beta = 3.76$ for air), while P and T are the initial pressure and temperature of the mixture. The functional form of Eq. 2.1 is based on trends observed in detailed calculations of induction lengths [40]. The correlation was developed with the view that the detonation cell size is most appropriate as a heuristic parameter in the design and analysis of RDWCs. As a result, no attempt was made to correct for factors that differ between the original experiments used to measure cell size and the present application to RDWCs, such as the presence of wall curvature, lateral relief, turbulence, and flow stratification. The green and black lines of Fig. 2.2 show the cell size computed by Eq. 2.1 for $\beta = 0$ and $\beta = 3.76$, respectively. A least squares fit was used to compute the remaining lines. The targeted range of operating conditions with chamber pressures of 1-2 MPa and the oxidizer preheated to 600 K produces an estimated cell size of 8 to 15 mm.

This analysis of detonation cell sizes does not account for the minor constituents in natural gas, such as ethane and propane. However, it has been shown that these additional species serve to sensitize the mixture via contribution of H radicals in initial chain branching reactions [41]. The addition of 5% ethane can reduce the ignition delay time by a factor of two. This effect will help to reduce the cell size and thereby increase the operable range of the RDWC.

The cell size analysis was used to inform the baseline dimensions of the combustor. The radial gap was selected to be on the order of one to two cell widths at the target operating conditions. The chamber diameter was then selected to ensure a minimum 10:1 ratio to the radial gap. This ratio was selected to reduce the influence of curvature effects while

maintaining a tractable combustor size. A large chamber diameter to radial gap ratio has been shown to produce significant radial variations in the detonation structure [42].

2.2.3 Injector Design

Two distinct injector concepts were designed and tested to evaluate their impact on combustor operability. The injection system of an RDWC must produce mixing on spatiotemporal timescales that sufficiently prepare the reactant mixture prior to the periodic arrival of detonation wavefronts. In addition, combustor operation and performance is highly sensitive to the geometric details of the injection system. A key parameter is the location of fuel injection relative to the throat of the oxidizer system, which has a significant impact on the injection dynamics and subsequent mixing. A brief review of airbreathing RDWC injector designs in the public literature showed that most operable systems placed the fuel injection downstream of the air injection throat [7], [15], [18], [19], [22], [25], [43]–[45]. Injecting fuel downstream of the oxidizer throat may make the dynamic injection and flow recovery process more receptive to coupling with the dynamics of the chamber environment, which may play a role in supporting stable operation. In contrast, RDWCs that operate with rocket propellants have been shown to produce stable operation with injection upstream or downstream of the oxidizer throat [16]. The distinction could be explained by operational differences between airbreathing and rocket RDWCs, including the relative strength of the detonation wave. Without the additional nitrogen in air, a detonation wave in a rocket RDWC will propagate faster and produce higher peak pressures. The pressure waves are then sufficiently strong to travel upstream past the oxidizer throat and perturb the fuel injection processes. Given this distinction between RDWC systems, the current design places fuel injection downstream of the air throat.

Figure 2.3 presents detailed schematics of both an axial and sting injector design, respectively denoted A and B. Both designs inject fuel from orifices in the expansion region of a circumferentially continuous oxidizer injection slot, forming a jet-in-crossflow. The location of fuel injection orifices was selected to promote interaction between unsteady shock trains from both the fuel and air. The shock train location will vary widely in response to the

dynamic pressure from each passing detonation wave. The principle difference between the two injector designs is that injector B has two axial oxidizer injection slots. While design A injects fuel from both the inner and outer circumference of the combustion chamber, design B injects fuel from the middle of the combustion channel into both axial air slots. Both concepts attempt to distribute fuel injection across the cross section of incoming oxidizer flow to increase the fraction of oxidizer exposed to the fuel. The area ratio between the combustion chamber and oxidizer throat is 8.6 for injector A and 9.4 for injector B.

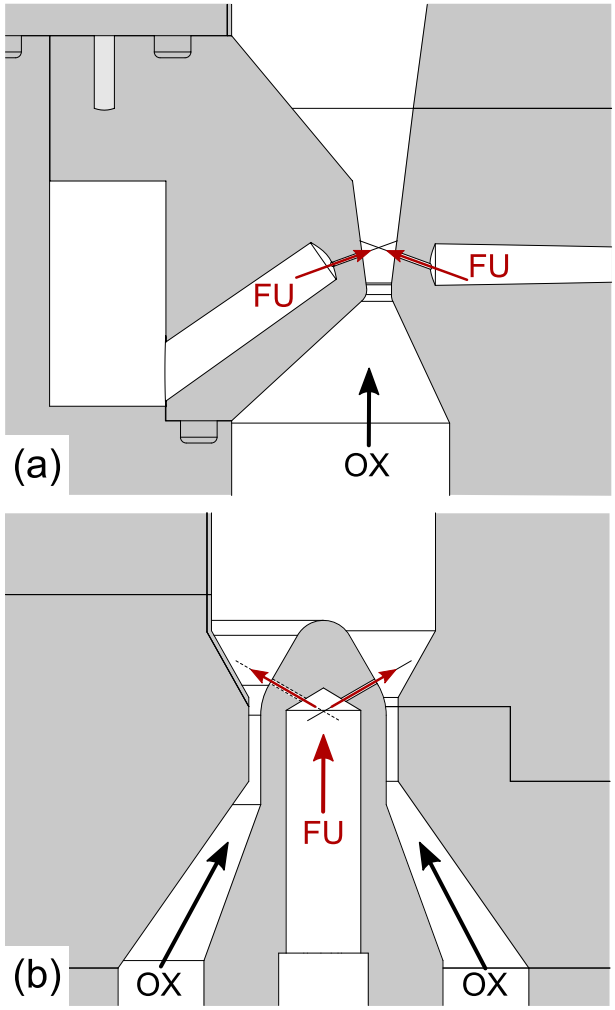

Figure 2.3. Detailed schematic of combustor head end geometry for axial injector A (a) and sting injector B (b) with arrows highlighting the flow of fuel (FU) and oxidizer (OX).

Two different nozzle contraction ratios (CR), 1.93 and 2.75, were tested with each injector configuration. This alters the Mach number of propellant flows within the chamber and the pressure ratio from each propellant manifold into the chamber. The injector dynamic response and the mixing near the head end of the chamber between detonation wave fronts is changed dramatically, particularly as the oxidizer injection is changed from a choked to unchoked condition. Changing backpressure nozzles varied the pressure ratio across the air injection slot from 1.5 - 2.5 while it changed from 2.5 - 4 across the fuel injection orifices. The pressure ratios were selected such that the injectors could respond after being checked off by each detonation head in time to sufficiently fill and mix propellants. Variation of combustor backpressure also affects the fill height, which is the axial extent of propellant inflow to the chamber between wave passage. Based on the approximation that premixed reactants fill the chamber head end volumetrically at the mean chamber pressure, the fill height is estimated to vary between 20-40% of the chamber length downstream of the injector throat due to changing backpressure nozzles.

2.2.4 Instrumentation and Optical Diagnostics

Operation of the experiment is remotely monitored and controlled using a National Instruments (NI) based data acquisition and control system (DACS). The NI signal conditioning hardware records analog inputs from pressure transducers, thermocouples, valve position indicators, and thrust stand load cells using a 16 bit ADC (NI PXIe-6375). It also provides digital control for valve actuation and analog set-point control of electronic regulators for closed-loop feedback control of pressure upstream of CFVNs (Tescom ER5000). A NI LabView Virtual Instrument (VI) is used for experiment operation and data acquisition. The VI provides auto-sequenced control with redline monitoring for automatic abort of test operations. All experiment control and condition monitoring operates at a frequency of 1 kHz [27]. High-frequency pressure and timing measurements were recorded with an independent NI data acquisition system that provides non-multiplexed readout on up to 32 channels at frequencies up to 2 MHz.

The RDWC is instrumented with an array of low-and high-frequency pressure transducers within the combustion chamber and propellant manifolds. A pressure transducer in the Capillary Tube Attenuated Pressure (CTAP) configuration with a length-to-diameter ratio of approximately 2000 was included for comparison to other studies. Pressure fluctuations were measured with water cooled piezoresistive transducers (Kulite WCT312M), which have a reported element natural frequency of 1.65 MHz. Prior studies have shown that it is difficult for transducers to survive in the preferred, flush-mount configuration due to the high heat fluxes associated with high pressure detonative combustion [16], [46]. Therefore, the transducers are installed in a recessed cavity with a resonant frequency > 50 kHz, which provides a measurement of detonation pressure with lower amplitude attenuation and phase lag than a comparable semi-infinite tube pressure installation while protecting the instrument [47]. The transducer outputs were recorded at 1 MHz to provide a high level of temporal resolution. While much consideration was given to the selection and installation of transducers for pressure measurements, the inherent limitations of pressure measurements in an RDE restricts their quantitative interpretation. The installation approach required for the high-frequency pressure transducers biases their measurements, while the interpretation of mean pressures from low-frequency transducers is unclear given that RDEs are a fundamentally unsteady system. As a result, the collected pressure measurements are primarily used to provide directional sensitivities and are not considered to be an accurate measurement of the thermodynamic state within the combustion chamber. Figure 2.4 specifies instrument port locations in the combustion chamber and propellant manifolds, while Table 2.1 lists the coordinates of each port. Reported measurements refer to the instrumentation port number to specify transducer location. Chamber transducers CC-01 and CC-02 were installed in all tests to allow consistent comparison across test days and instrumentation configurations.

The wave dynamics in the chamber are visualized by direct imaging of the combustor annulus. Images are recorded at 110 kHz at a resolution of 384 x 384. Broadband chemiluminescence from the chamber is collected by a 500 mm focal-length, f/5.6 objective lens (Nikon AF-S 200-500mm) and imaged by a Phantom v2512 high speed CMOS camera. Chamber images provide information about the wave number, topology, and velocity.

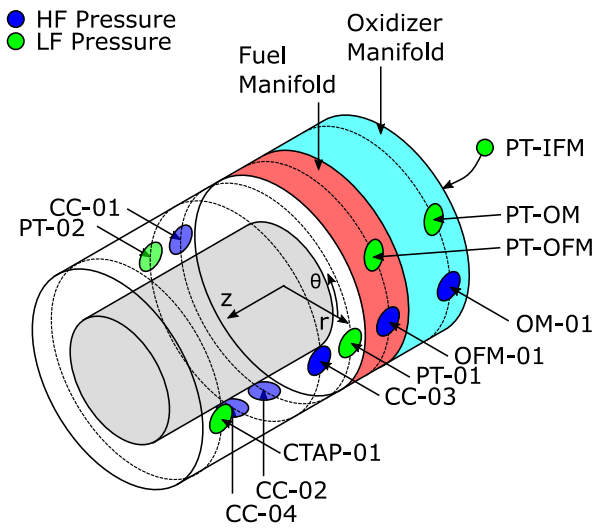

Figure 2.4. Measurement port locations around circumference of combustor.

Table 2.1. Coordinates of transducer port locations on combustor.

Port	Location	θ [deg]	z [mm]
OM-01	Oxidizer Manifold	0	-41
OFM-01	Outer Fuel Manifold	0	-2
CC-01	Chamber	180	27
CC-02	Chamber	270	27
CC-03	Chamber	0	49
CC-04	Chamber	270	49
PT-OM	Oxidizer Manifold		
PT-OFM	Outer Fuel Manifold		
PT-IFM	Inner Fuel Manifold		
PT-01	Chamber	0	27
PT-02	Chamber	180	49
CTAP-01	Chamber	270	100

2.3 Results and Discussion

The RDWC was tested with both injector configurations across a range of operating conditions in a broad parametric survey of mass flux, G, mass fraction of oxygen in the main oxidizer flow, $Y_{O_2}^{Ox}$, equivalence ratio, ϕ, and mass fraction of hydrogen in the fuel flow, $Y_{H_2}^{F}$. Approximately 60 tests were conducted with each injector, where half of all tests used air without oxygen enrichment. The range of tested conditions is summarized in Table 2.2.

Table 2.2. Range of tested combustor operating conditions.

G $[kg/m^2/s]$	ϕ	$Y_{O_2}^{Ox}$ [%]	T_3 [K]	$Y_{H_2}^{F}$ [%]	P_c [MPa]
200-500	0.85-1.2	23.2-35	575-800	0-17	0.7-1.8

2.3.1 Chamber Dynamics

Figure 2.5a presents a pressure-time history illustrating a typical test sequence. Propellant flows are established prior to ignition to allow fuel manifolds to fully prime. The pre-detonator injects a detonation wave into the chamber and ignites the main chamber propellants at t = 0. Ignition triggers a short startup transient where the number and direction of detonation heads can change on a per-cycle basis. The pressure fluctuations then enter a limit cycle characteristic of one or more rotating detonation waves within the chamber. The pressure-time history in Fig. 2.5b shows steep-fronted waveforms with modulating peaks that decay to approximately the mean chamber pressure. The pressure measurements at CC-01 and CC-02 exhibit a consistent phase relationship, indicating the presence of co-rotating detonation waves in the chamber. Inspection of high speed video reveals a single wave circumscribing the chamber, corroborating observations from the pressure transducers. This test was conducted with injector B using the CR = 1.93 nozzle. The operating conditions were a mass flux of $G = 350 kg/m^2/s$, equivalence ratio of $\phi = 0.90$, air inlet temperature of $T_3 = 590 K$, and pure air as the oxidizer. Operation with a single detonation wave was only observed at a narrow range of conditions similar to this test.

Figure 2.6 shows the operating wave mode and velocity as a function of flow condition for the injector B and CR = 1.93 nozzle configuration. This was the only configuration to exhibit either single or co-rotating waves. Single-wave operation was observed at each of the three tested mass fluxes and only in a narrow range of equivalence ratios between 0.90 and 0.95. While most other conditions produced counter-rotating waves with one wave propagating in each direction, the test conducted at a mass flux of $G = 450 kg/m^2/s$ and equivalence ratio of $\phi = 1.0$ resulted in two waves propagating in each direction. Equivalence ratios greater than 1.15 resulted in steady combustion. The wave speed relative to the CJ velocity varied between 55-65% for all conditions operating with this injector and nozzle configuration.

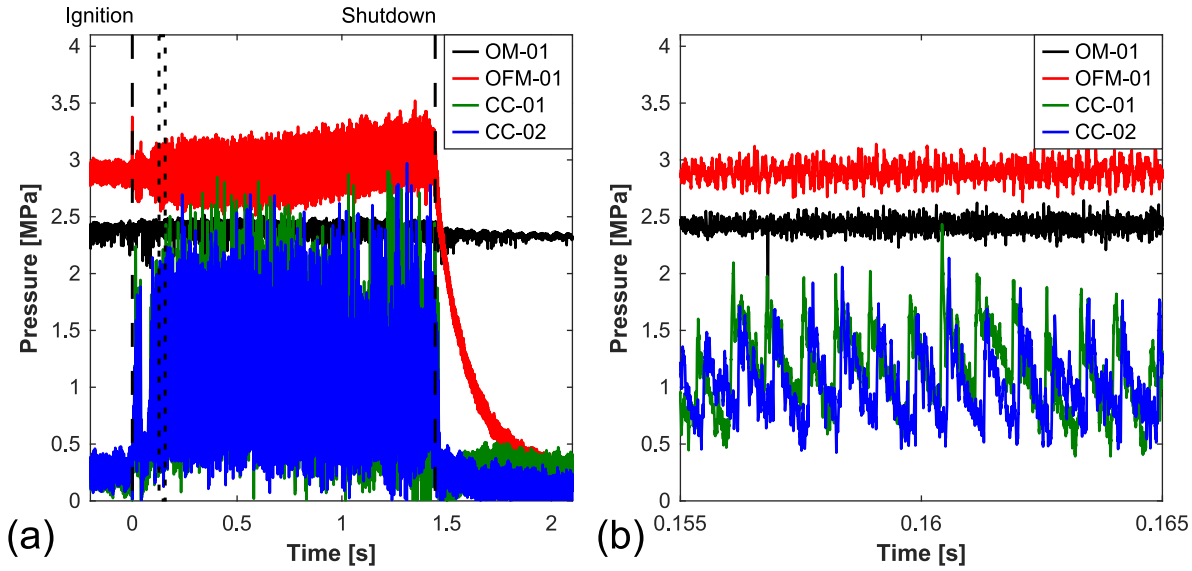

Figure 2.5. Representative high frequency pressure measurements illustrating (a) test sequence and (b) steep fronted waves from a rotating detonation wave in the chamber.

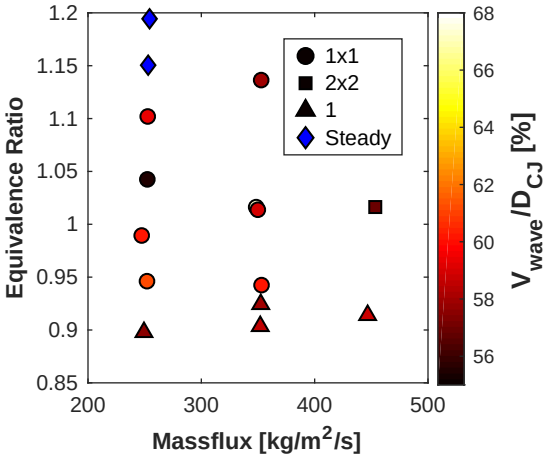

Figure 2.6. Wave mode and velocity as a function of flow condition for injector B using the CR = 1.93 nozzle.

The power spectral density (PSD) of the chamber pressure signal computed from a 100 ms window of the representative test is shown in Fig. 2.7a. The steep-fronted oscillations evident at measurement location CC-01 correspond to the fundamental frequency of 1.45 kHz and subsequent harmonics. Measurement location CC-02 shows a similar sequence of harmonics. Both chamber pressure transducers exhibit a minor peak at 1.24 kHz near the fundamental

frequency. This corresponds with a counter-propagating wave which gains strength and subsequently decays during the 100 ms window of the PSD, though the dominant operational mode is still a single detonation.

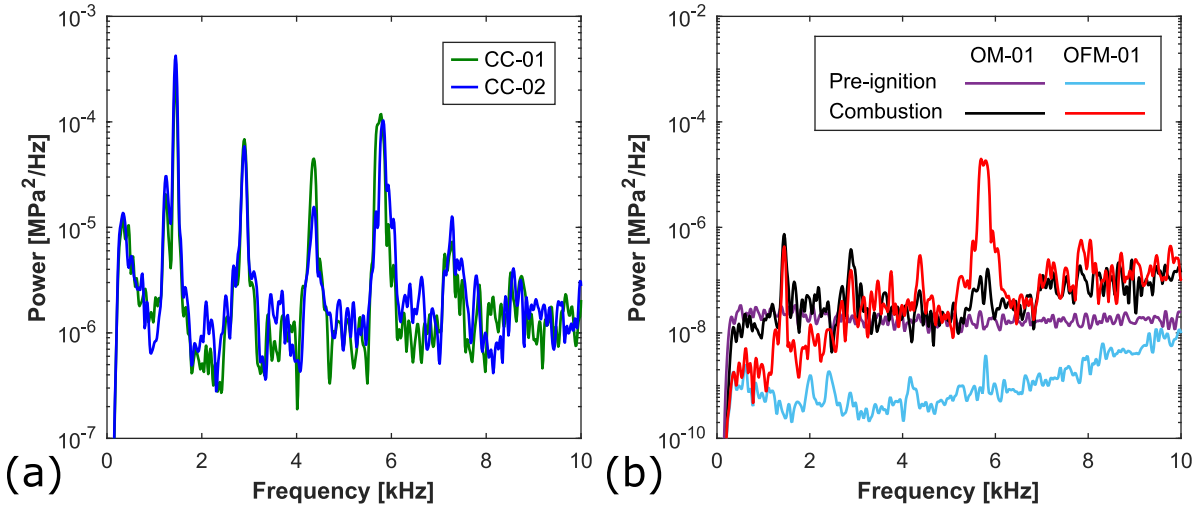

Figure 2.7. Power spectral density plots of (a) chamber pressure transducers and (b) manifold pressure transducers.

The steep-fronted waves found in the combustion chamber apply forcing to the propellant manifolds. Spectral analysis of transducers located in the outer fuel and oxidizer manifolds, OFM-01 and OM-01 respectively, reveals periodic content in Fig. 2.7b. During combustion, both manifolds respond at the fundamental forcing frequency of 1.45 kHz, and higher harmonics. It is unclear why the fuel manifold responds so strongly at 5.8 kHz, the fourth harmonic of the chamber fundamental frequency. The peak frequency of both manifolds is observed to vary between harmonics of the chamber frequency across the range of tested conditions, though no trend is discernible. Figure 2.7b overlays a second PSD from a window immediately prior to ignition to see if any frequencies inherent to the manifolds persist. The oxidizer manifold exhibits no clear natural frequency, while the fuel manifold has natural resonances at 2 and 2.4 kHz. These manifold responses are typical of the parametric survey, where the forcing applied by steep-fronted detonation waves is observed in manifold pressure fluctuations, but there is no indication that the manifold acoustics correspond to the chamber limit cycle frequency.

Imaging of the combustor annulus provides information about wave dynamics throughout each test. Figure 2.8a plots the time-history of pixel intensity around the chamber circumference by transposing the θ direction of Fig. 2.4 onto the y-axis, similar to the method of Bennewitz *et al.* [48]. Inspection of the pixel intensity time-history (referred to as the "detonation surface") reveals a single detonation wave propagating in the $+\theta$ direction, consistent with the phase relationship between CC-01 and CC-02 in Fig. 2.5. Comparison with the single image of Fig. 2.8b illustrates how the detonation surface can be used to extract information about the wave structure. The vertical width of lines on the detonation surface reflect the extent of post-wave combustion luminescence, seen extending from the wave front at $\theta = 85°$ to $\theta = 340°$ in Fig. 2.8b. An ideal detonation front would appear as a line of vanishing width in Fig. 2.8a. Changes in line slope and spacing make cycle-to-cycle variation in wave propagation apparent on the detonation surface, while it is difficult to ascertain from image sequences.

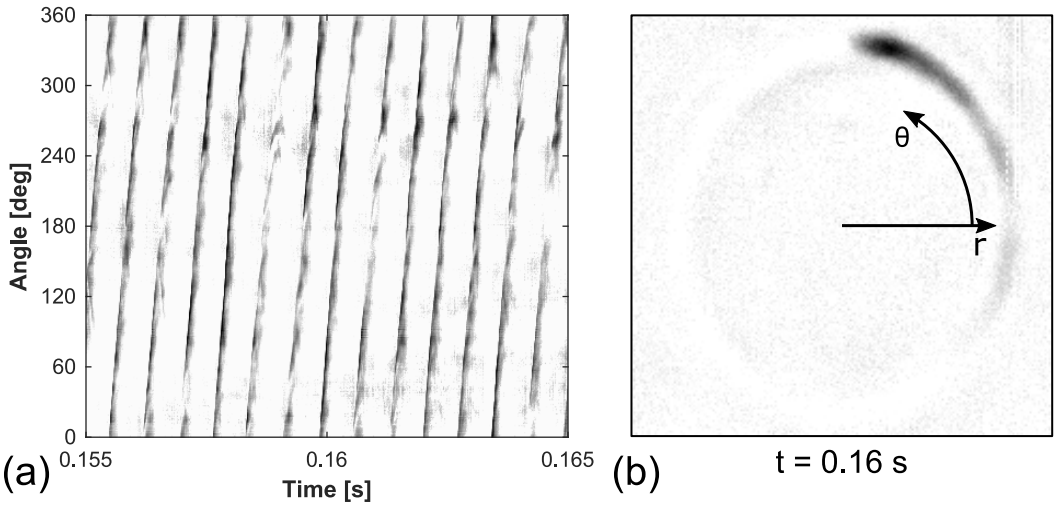

Figure 2.8. Detonation surface plot (a) and high-speed image (b) showing a single detonation wave.

Figure 2.9 depicts the pressure-time history and detonation surface plot from another representative test with two counter-propagating detonation waves in the combustion chamber. This test was conducted with injector A and the CR = 2.75 nozzle, where the operating conditions were $G = 250 kg/m^2/s$, $\phi = 1$, $T_3 = 730K$, and pure air as the oxidizer. The

wave intersection at $\theta = 0°$ and $\theta = 180°$ throughout the time slice of Fig. 2.9b is consistent throughout the duration of the test, aside from startup and shutdown transients. Transducer CC-01 is situated at the $\theta = 180°$ intersection point, resulting in the pressure fluctuation amplitudes seen in Fig. 2.9a that exceed three times the mean chamber pressure. Pressure probe CC-02 is located at $\theta = 270°$, resulting in lower fluctuation amplitudes and two peaks between each peak in CC-01. While the wave intersection points in this test are aligned with the inlets feeding the oxidizer manifold located upstream at $\theta = 0°$ and $\theta = 180°$, this is not observed at all operating conditions. The intersection points have been observed to precess during the test while still producing high-amplitude pressure fluctuations at other flow conditions [49].

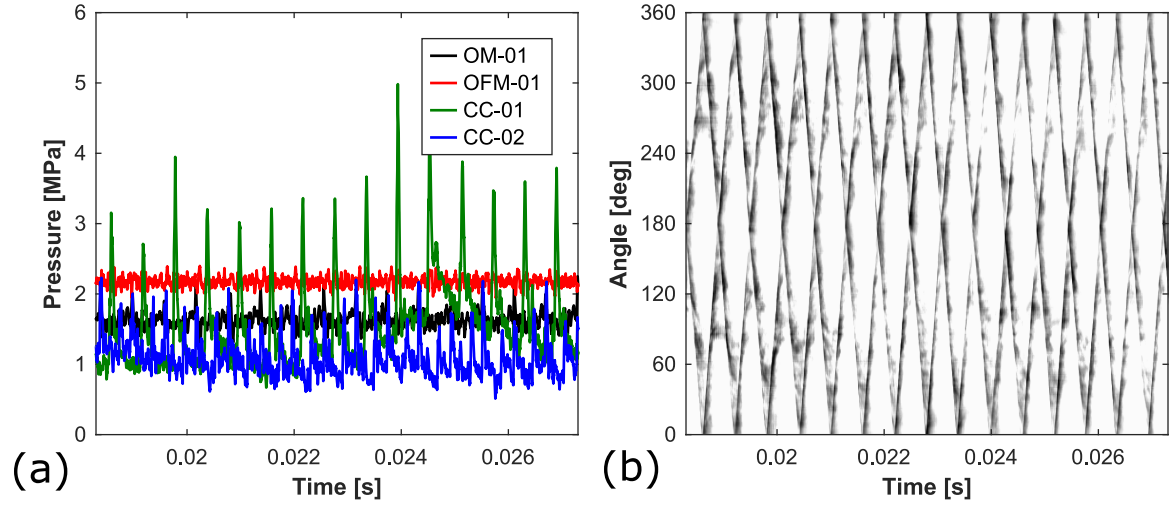

Figure 2.9. Pressure time history (a) and detonation surface plot (b) for a representative test case with two counter-propagating detonation waves.

2.3.2 Analysis Approach

In order to understand the sensitivity of the strength and stability of chamber dynamics to operating condition, two metrics were selected to evaluate each test. The average amplitude of pressure fluctuations normalized by the mean chamber pressure measured with PT-02, P/P_c, provides an indication of the strength of detonation waves in the chamber. The pressure fluctuation amplitude for a single transducer is computed as the difference between

the mean peak pressure and mean valley pressure across a sufficient number of samples to converge the first-order moment [50].

Figure 2.10a and b illustrate the efficacy of the peak identification process for the pressure histories of Fig. 2.5b and Fig. 2.9a, respectively. The figure shows a plot of each pressure series notated with the identified peaks alongside a histogram of the pressure fluctuation amplitude for each transducer location. The overlapped histograms of Fig. 2.10 show that a single detonation wave produces a similar distribution of pressure fluctuation amplitudes at each transducer location. In comparison, Fig. 2.10b shows a test where the intersection point of counter-rotating waves aligned with a single transducer, producing peak pressures that do not appropriately characterize the overall chamber dynamics. There is little overlap in the distributions of pressure fluctuation amplitude for each transducer. A more representative value of P is then obtained by averaging the pressure fluctuation amplitude measured across all installed transducers. The typical relative uncertainty of the normalized pressure fluctuation amplitude, P/P_c, is 2-4% with a 95% confidence interval.

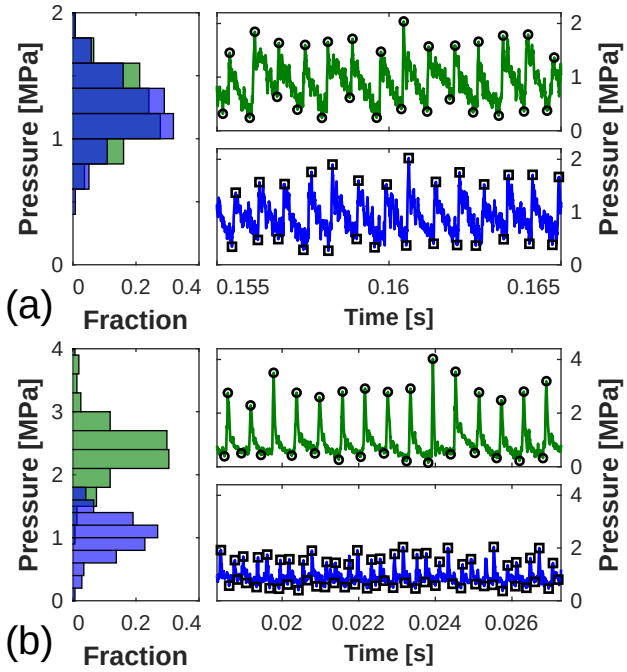

Figure 2.10. Peak identification and distribution of pressure fluctuation amplitudes for representative test cases exhibiting (a) single and (b) counter-rotating wave modes.

The coherence of wave dynamics was characterized by the fraction of spectral power contributing to the primary limit-cycle process in the measured pressure-time history and was computed as the integral of the power spectral density under peaks corresponding to the fundamental frequency, harmonics, and subharmonics normalized by the total power contained in the signal. The domain of integration spanned until the power had dropped to 95% of the peak value, or an adjacent peak was found. Termed the power fraction (PF), this parameter is expected to approach unity for stable, robust chamber dynamics and will diminish to zero for weaker dynamics with additional frequencies that correspond to superimposed processes. Similar to the pressure fluctuation amplitude, the reported power fraction is an average of the power fractions computed for each installed pressure transducer.

Figure 2.11 demonstrates the ability of this method to distinguish signals affected by different types and magnitudes of contamination. Two synthetic signals are presented as examples, a sine wave and a periodic, steep-fronted waveform. Increasing the parameter σ systematically decreases the coherence of each signal using three corruption models. The "Noise" method adds white Gaussian noise with a variance of σ^2. The "Mix" model has been used in prior studies of signal regularity [51] and samples either the underlying signal or a uniformly distributed random value with probability σ. As σ increases, the corruption model transitions from sampling the true signal to sampling random noise. The sample timeseries use a value of $\sigma = 0.1$ for both the "Noise" and "Mix" models. Finally, the "Dephase" corruption method changes the signal phase by a random, uniformly distributed amount with probability σ, where a value of $\sigma = 0.02$ was selected for the plots of Fig. 2.11a.

Figure 2.11b then presents the power fraction computed for the six combinations of waveform type and corruption method over a range of the parameter value, σ. For each combination, the power fraction was averaged over 10-40 realizations of the corruption method. As expected, the power fraction of both the sine and steep-fronted waves begins near unity and is insensitive to the "Noise" and "Mix" corruption methods for $\sigma < 0.1$. Higher levels of contamination result in a gradual roll-off in power fraction. The "Dephase" corruption model results in a steep decline in power fraction for values of σ as low as 0.001. The high sensitivity to dephasing is the desired outcome, as it is most representative of the signal corruption that the power fraction attempts to differentiate.

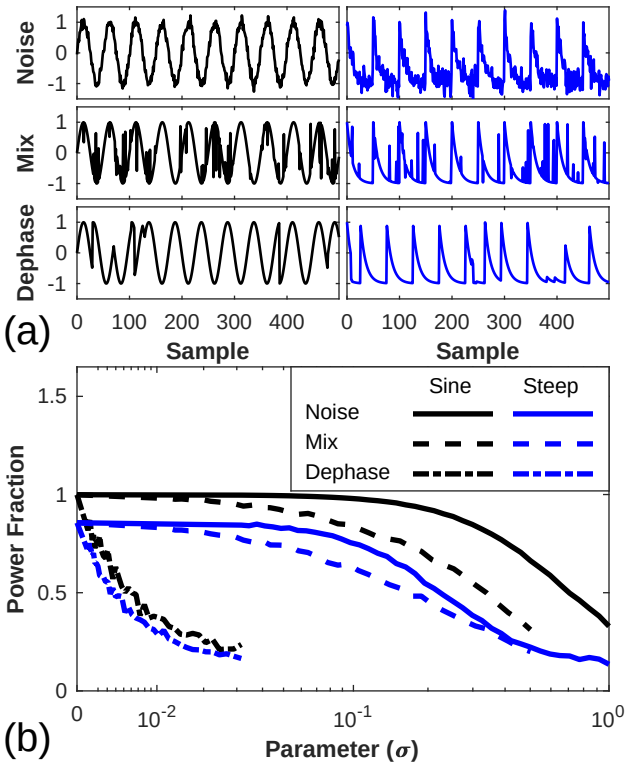

Figure 2.11. Demonstration of power fraction metric with (a) synthetic sine wave and steep-fronted signals with three types of contamination and (b) power fraction for varying levels of signal contamination.

The pressure fluctuation amplitude and power fraction are computed from a 100 ms window (150-600 waves, depending on operating condition) selected from the approximate middle of each test to avoid the transient effects of startup or fuel cutoff at shutdown. The pressure fluctuation amplitude was 1.9 and 2.4 for the two tests corresponding to Fig. 2.10a and b, respectively. The corresponding power fractions were 51% and 63%.

2.3.3 Global Operability

Figure 2.12 depicts scatter plots that summarize the range of tested conditions in terms of power fraction, estimated wave speed, and estimated cell size at mean chamber conditions. The markers are colored by the pressure fluctuation amplitude, while the shape indicates the injector configuration. Figure 2.12a shows that the power fraction, estimated wave velocity, and pressure fluctuation amplitude are all approximately correlated. This is expected, as

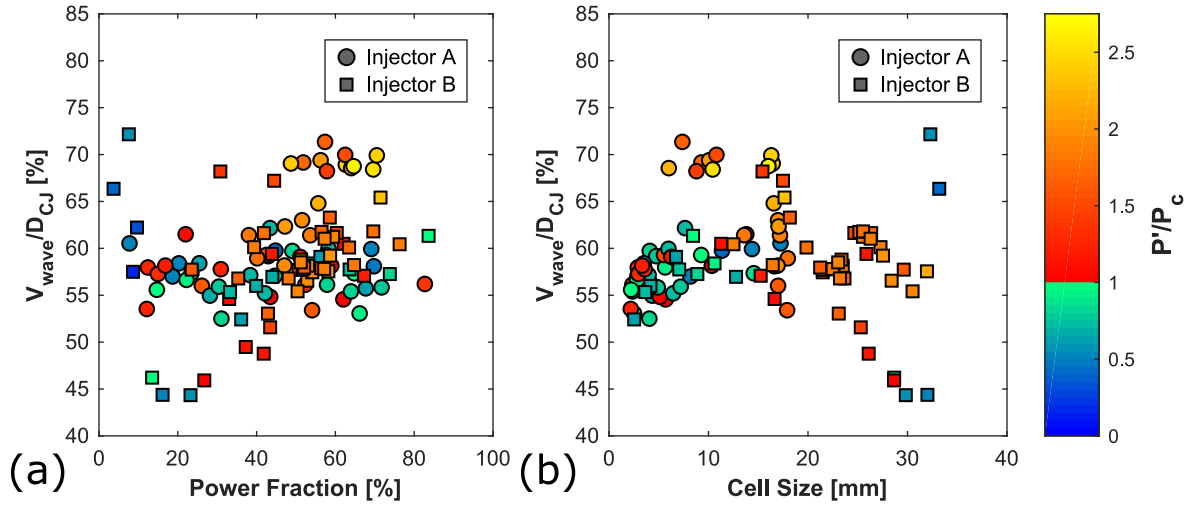

Figure 2.12. Scatter plots of detonation quality evaluated by power fraction, pressure fluctuation amplitude, cell size, and estimated wave velocity.

faster detonation waves will produce stronger leading shocks and thereby higher pressure fluctuations. Tests with high power fractions, indicating stable detonation propagation, will similarly tend to produce higher pressure fluctuation amplitudes because there are fewer auxiliary processes within the combustion chamber that could destructively interfere with and weaken the detonation.

Figures 2.12a also shows an approximate floor in the observed wave velocities between 50-60% of the CJ detonation velocity for the mixture. Studies of the deflagration-to-detonation transition process have found that deflagration waves will accelerate to approximately half of the CJ detonation velocity before spontaneous transition to detonation [2]. Furthermore, deflagration waves can propagate at this velocity in a quasi-steady manner, which produces an uncoupled precursor shock ahead of the combustion front wherein turbulence is likely the mechanism supporting self-propagation. This shock-turbulent reaction front complex has been modeled as a CJ deflagration, resulting in a predicted velocity that closely matches the observed 50% of the CJ detonation velocity [52]. In the present RDWC experiments, it is possible that the intense turbulence created in the inflow supports the propagation of a combustion wave similar to a CJ deflagration, which would explain the observed floor in velocity with moderate pressure fluctuation amplitudes.

Some of the points in Fig. 2.12a demonstrate the limitations of both the power fraction and the estimated wave velocity for interpretation of test outcome. For example, the two points at the upper left of the plot indicate tests that had estimated wave speeds of 65-75%. However, their low power fraction and pressure fluctuation amplitude indicates that these tests likely produced steady combustion instead of detonation waves. Test cases with high power fractions but very low pressure fluctuation amplitudes similarly resulted in steady deflagration. This highlights the benefit of using both the power fraction and pressure fluctuation amplitude when looking at trends between test cases.

Figure 2.12b compares the estimated wave speed and cell size with the pressure fluctuation amplitude. Here it is apparent that the estimated cell size is not correlated with the pressure fluctuation amplitude or estimated wave speed. In fact, the cases with the highest pressure fluctuation amplitudes and wave speeds have cell widths that are approximately the width of the combustor or one half its width. As discussed in Section 2.2.2, the nonideal flow field and boundary conditions found in an RDWC relegate the detonation cell size to an approximate scaling parameter. Figure 2.12b then suggests that the cell size must be of the right order of magnitude to support detonative operation, but that continued decreases do not guarantee more stable operation.

2.3.4 Parameter Sensitivities

The effect of individual inlet flow conditions on combustor operability was then investigated for each tested combination of injector and backpressure nozzle. The combustor mass flux, oxygen mass fraction, equivalence ratio, and hydrogen mass fraction were all varied independent of other operating conditions. Each test was conducted at either a high or low oxidizer inlet temperature, $T_3 = 710 - 750K$ and $T_3 = 600 - 675K$ respectively. Injector A could not be reliably ignited with the CR = 1.93 exit nozzle because of a high degree of flow expansion into the chamber. Pressure transducers at locations PT-01 and PT-02 measured approximately 70 kPa prior to ignition at this condition, while the oxidizer manifold pressure PT-OM was 1.3 MPa. This indicates the bulk velocity in the injection and combustion

region was $O(800m/s)$ with a Mach number of 2.5, preventing the combustion process from occurring within the chamber.

Figure 2.13 shows the sensitivity of detonation propagation within the combustor to changes in the mass flux, G. These tests were conducted with unity equivalence ratio and an oxidizer inlet temperature, T_3, of $600 - 675K$. The mass fraction of oxygen in the oxidizer flow was fixed at $Y_{O_2}^{Ox} = 28\%$ with injector A, while pure air was used for the tests with injector B.

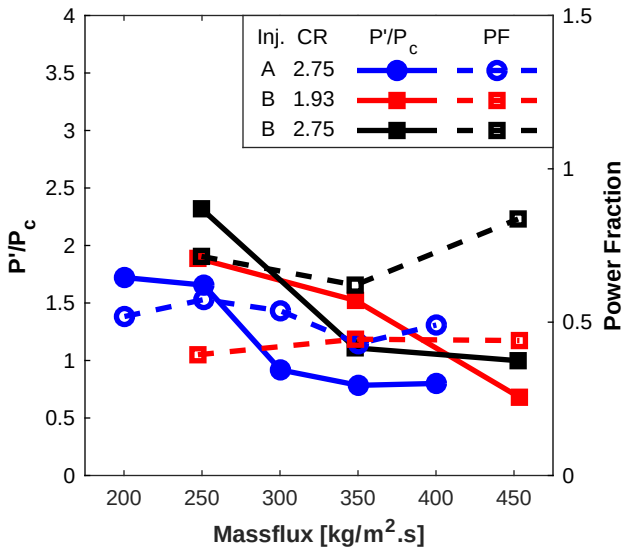

Figure 2.13. Sensitivity of combustor operability with respect to mass flux, G.

The pressure fluctuation amplitude decreases with increasing mass flux for each combination of injector and backpressure nozzle. Similarly, power fraction decreases with increasing mass flux for injector A, consistent with detailed observations of the pressure-time history that indicate less stable wave propagation [49]. However, there is no clear trend in power fraction as the mass flux is increased for injector B with both backpressure nozzles. Inspection of the corresponding pressure-time histories shows that the pressure fluctuations are highly periodic, but low amplitude. In addition, the wave speed decreases from 65-70% of the CJ detonation velocity to 55-60%. This could correspond to a transition from low-order detonations to CJ deflagration waves. Increasing the mass flux also results in an increased number of detonation fronts in the combustor. For injector A, the number of waves increases

from one propagating in each direction to two in each direction at $G = 300kg/m^2/s$. Injector B with the CR = 2.75 nozzle behaves in the same manner, although the transition from one to two waves propagating in each direction is observed to occur at $G = 350kg/m^2/s$ due to the more limited number of tested conditions. In contrast, Injector B with the CR = 1.93 nozzle maintains a single wave in each direction at $G = 350kg/m^2/s$, but transitions to two waves in each direction by $G = 450kg/m^2/s$. The number of waves within the chamber increases with mass flux for both injectors and results in a higher wave arrival frequency, which decreases the amount of time available to refresh the combustor channel with sufficiently mixed, fresh propellants. Combustion of reactants that are not completely mixed will then reduce the wave speed and pressure fluctuation amplitude, until a new equilibrium between wave strength and propellant mixing has been reached.

Variation of mass flux (Fig. 2.13) approximately isolates the effect of chamber pressure on the wave dynamics because the injection pressure ratios and Mach numbers remain constant for a given geometry defined by the combination of injector configuration and backpressure nozzle. The reduced pressure fluctuation amplitudes with increasing mass flux may then be a result of higher pressures suppressing the detonation waves. This is consistent with the observed operation of injector B with the CR = 1.93 nozzle, which produces a lower chamber pressure for a given mass flux and accordingly is able to operate at higher mass fluxes. Nozzles with high contraction ratios have also been shown to reflect the trailing oblique shock from the detonation front back into the injection region, which can adversely affect injection dynamics and lead to wave failure [53]. It should be noted that varying mass flux does not strictly isolate the effect of chamber pressure, as propellant mixing and chemical kinetics also depend on local gas thermophysical properties such as density.

Sensitivity to the chemical kinetic timescales of the propellant mixture was explored by changing the mass fraction of oxygen in the main oxidizer flow and the combustor inlet temperature while maintaining the equivalence ratio and mass flux constant at unity and $250kg/m^2/s$, respectively. Trends in detonation strength and stability are shown in Fig. 2.14. For all injector and nozzle configurations, the fundamental frequency of the chamber dynamics increased with $Y_{O_2}^{Ox}$. Tests with Injector A at low T_3 exhibited a narrow range of oxygen content that supported stable, detonative operation, shown in Fig. 2.14 by the peak in P/P_c

at $Y_{O_2}^{Ox} = 26\%$ and higher power fraction for tests with $Y_{O_2}^{Ox} = 26 - 28\%$. These conditions resulted in stable, counter-propagating detonation waves, while higher and lower oxygen content produced chaotic chamber dynamics, with inconsistent pressure fluctuation amplitudes and waveforms. At the higher oxidizer inlet temperature range, the range of oxygen contents that produced stable, counter-propagating waves shifted to pure air, $Y_{O_2}^{Ox} = 23.2\%$. While increasing the oxygen content to 26% resulted in low pressure fluctuation amplitude and power fraction characteristic of muddled chamber dynamics, further increases permitted stable combustion fronts to re-form. This is observed in the increase in both P/P_c and power fraction in Fig. 2.14.

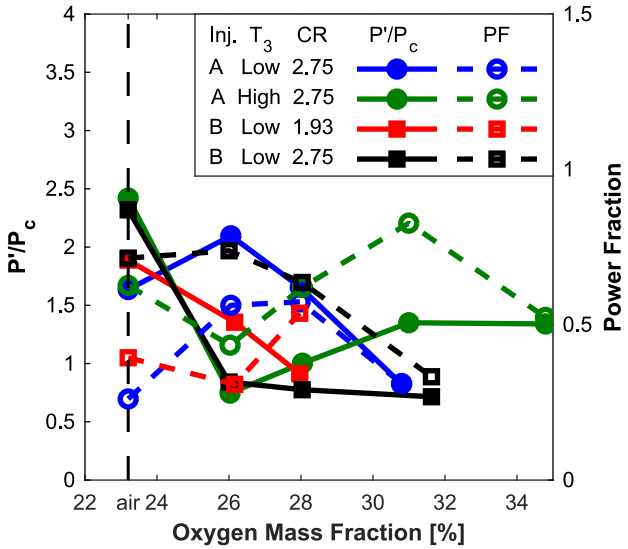

Figure 2.14. Sensitivity of combustor operability with respect to mass fraction of oxygen in oxidizer flow, $Y_{O_2}^{Ox}$.

While the addition of oxygen improves detonation stability for injector A at some operating conditions, it appears to uniformly decrease the operational stability for injector B. This is shown by the monotonic decrease in pressure fluctuation amplitude with increasing oxygen content for both nozzle configurations. While the power fraction similarly decreases for the CR = 2.75 nozzle, it increases for the CR = 1.93 nozzle. This is not consistent with observations of raw pressure-time histories and imaging of chamber wave dynamics, illustrating the importance of considering multiple metrics in evaluating combustor operation.

For injector A, the shift in the oxidizer oxygen content that causes the combustor to transition from two to multiple counter-propogating waves at different oxidizer inlet temperatures could be explained by the role of the two parameters in the chemical kinetics of the reactant mixture. RDWC operation requires a fine balance between transient propellant mixing and chemical reaction timescales to present an appropriately prepared mixture to the detonation wave without producing deflagration [50], [54]. Increasing the inlet air temperature or the mass fraction of oxygen are both expected to change the reaction timescales by reducing the ignition delay time of the propellant mixture. Therefore, increasing mixture temperature would require a corresponding decrease in oxygen content to maintain the balance between mixing and chemical kinetics to support detonation in a particular operating regime.

Figure 2.15 presents the variation in combustor operability with respect to equivalence ratio, conducted with a mass flux of $250 kg/m^2/s$ and pure air as the oxidizer. The tests with injector A were conducted at the high T_3 condition, while those with injector B used air inlet temperatures in the low range. Both injector configurations produce the strongest, most stable detonation waves at unity equivalence ratio when operating with the CR = 2.75 nozzle. This is seen by the sharp drop in power fraction and pressure fluctuation amplitude moving to fuel-rich or fuel-lean mixtures. In contrast, injector B with the CR = 1.93 nozzle exhibits more stable operation with higher pressure fluctuation amplitudes at lean equivalence ratios. While P/P_c peaks at $\phi = 0.9$, the power fraction plateaus between $\phi = 0.9 - 0.95$. In particular, the condition with $\phi = 0.9$ produces a single detonation wave in the chamber, while all other conditions result in counter-propagating detonations or steady combustion with no wave fronts visible in high speed imaging.

Viewing the sensitivities presented in Figs. 2.14 and 2.15 together then presents a more complete view of the dependence of combustor operation on the chemical kinetic sensitivity of the propellant mixture. For injector A, the chemical kinetic timescales need to be modestly reduced via enriching the air with oxygen or operating with higher inlet temperatures before a stable, high-amplitude detonation forms. More significant perturbations from further sensitizing the mixture with additional oxygen or departure from the stoichiometric condition significantly diminishes the ability of the detonation to propagate. Injector B with

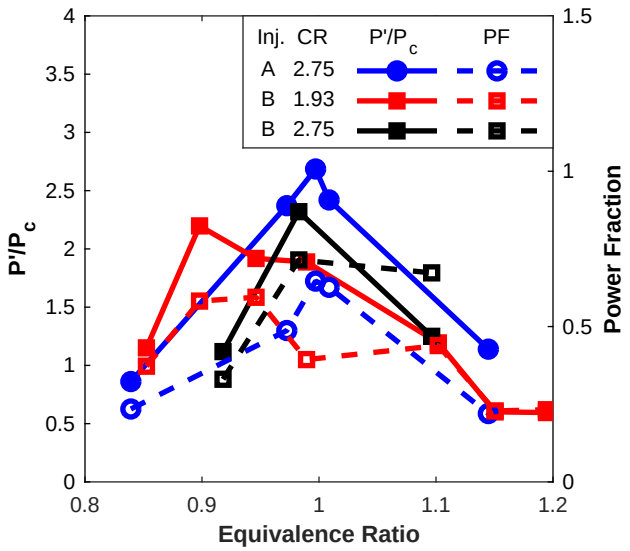

Figure 2.15. Sensitivity of combustor operability with respect to equivalence ratio, ϕ. Injector B with the CR = 1.93 nozzle at $\phi = 0.9$ results in operation with a single detonation wave.

the CR = 2.75 nozzle functions similarly, though unlike injector A does not require the additional sensitization from oxygen or increased air inlet temperature to produce strong, stable detonation waves. The primary difference between these two configurations is the geometry of the injection and mixing regions. The operational differences between the two inlets, where injector A requires enrichment to produce stable detonation waves while injector B does not, could then be attributed to their relative mixing effectiveness and would indicate that injector B better mixes the propellants than injector A. Further enhancing the chemical kinetics with injector B then produces deflagration burning, as the mixture is able to ignite prior to arrival of subsequent waves.

The same reasoning suggests that injector B with the CR = 1.93 nozzle produces even better mixing. While operation with pure air in the low temperature range produces strong detonations, reducing the equivalence ratio increases the detonation stability, resulting in the bias towards fuel-lean mixtures seen in Fig. 2.15. The conclusion that reducing the nozzle contraction ratio produces better mixing is consistent with basic fluid dynamics analysis, where decreasing the nozzle contraction ratio increases the pressure ratio across both the fuel and oxidizer injectors. The shock trains within each injectant flow are then stronger and the

resultant unsteady interactions result in more complete mixing on shorter spatial/temporal timescales. In addition, the manifolds are better able to re-initiate flow after being checked off by the overpressure from the passing detonation wave. However, this configuration is also observed to produce higher losses [55].

The final operational parameter varied was the mass fraction of hydrogen in the fuel, shown in Fig. 2.16. A limitation of this study was that the hydrogen could not be premixed with the natural gas and was instead injected via the inner injector of configuration A, while natural gas was flowed through the outer injector. These tests were conducted with $G = 250 kg/m^2/s$, pure air as the oxidizer, $\phi \approx 1$, and T_3 in the range of $710 - 750K$. Addition of hydrogen resulted in a sharp decrease in the pressure fluctuation amplitude, while the power fraction remained approximately constant across the series of conditions. Inspection of high speed video for tests with hydrogen revealed no wave motion, while individual pressure-time histories exhibited chamber dynamics more similar to combustion instability with smooth, nearly sinusoidal waveforms that produced a high power fraction.

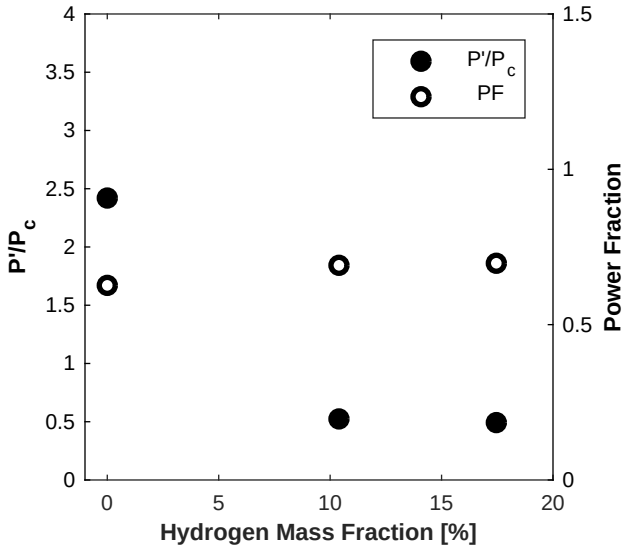

Figure 2.16. Sensitivity of combustor operability with respect to hydrogen addition to fuel, $Y_{H_2}^F$, with injector A and nozzle CR = 2.75.

The detonation wave dynamics with hydrogen addition observed in this study do not match trends found in prior research, where it has been shown to improve detonation strength

and stability. Several possible explanations include differences in injection geometry or operating conditions and chemical kinetic limitations. Injection of pure hydrogen from the inner fuel manifold and natural gas from the outer fuel manifold of injector design A is expected to produce radial fuel stratification. As a consequence, a propellant mixture near the inside diameter of the combustor would be more susceptible to deflagration burning, and could interfere with the development of coherent chamber dynamics. Compared to other experiments that have investigated RDWC operation with mixtures of hydrogen and natural gas or methane, this experiment operated at higher air inlet temperatures [23], and higher pressures and natural gas content [26]. Furthermore, at comparable hydrogen mass fractions, $Y_{H_2}^F$, Bykovskii *et al.* observed either poor, unstable detonations or combustion external to the chamber [23]. The tests conducted in this study and by Bykovskii *et al.* could be near a crossover point in the chemical kinetics of hydrogen-natural gas mixtures, where one fuel begins to have a greater effect than the other. Detailed calculations of the chemical kinetics of hydrogen-air mixtures applied to RDWC systems have shown similar crossover points due to pressure variation [54]. The sensitivity to mixture chemical kinetic timescales observed through changing the propellant combination and by variation of equivalence ratio and oxygen addition highlights the importance of testing RDWCs at application relevant flow conditions with corresponding propellants.

2.4 Conclusion

Detonation wave dynamics in a high pressure, natural gas-air RDWC were investigated using high frequency pressure measurements and direct imaging of wave motion in the combustor annulus. A broad parametric survey characterized the sensitivity of combustor operability to the mass flux of reactants, oxygen mass fraction in the oxidizer flow, equivalence ratio, and mass fraction of hydrogen in the fuel. Sensitivities were evaluated using pressure fluctuation amplitude as a measure of detonation strength and the fraction of spectral power associated with the primary chamber dynamics, termed the power fraction, for comparison of operational mode stability.

Global evaluation of detonation quality showed that combustion fronts in the combustor propagate at a minimum velocity of approximately 50% of the mixture CJ detonation velocity. This could correspond to a precursor shock-turbulent flame complex that forms a CJ deflagration wave. Comparing operability metrics to the estimated detonation cell size for each test showed that cell size should be at most of the order of the chamber gap, but that smaller cell sizes fail to guarantee formation of high-order detonation waves. This supports the view of the cell size as an approximate scaling parameter for RDWC design, due to the non-canonical flow and boundary conditions found in a combustor.

Comparison of combustor operation at different mass fluxes showed that higher chamber pressures likely suppressed the detonation, resulting weaker pressure fluctuation amplitudes and less stable wave propagation for the studied configurations. Parametric variation of the oxidizer oxygen content showed that injector A required limited sensitization to support robust detonation, but that further oxygen enrichment resulted in more waves and chaotic pressure-time histories. Increasing the oxidizer inlet temperature reduced the range of oxygen content that supported stable operation to pure air, pointing to changes in chemical kinetics as an important factor. In comparison, injector B required no sensitization with the CR = 2.75 backpressure nozzle, and produced stronger detonation waves at fuel-lean conditions with the CR = 1.93 nozzle. This suggests that injector B produces better mixing than injector A, as any method of sensitizing the mixture results in less coherent chamber dynamics or steady deflagration. Finally, addition of hydrogen to the fuel was shown to result in deflagrative combustion with no wave motion.

The parametric survey showed that chamber wave dynamics are typically characterized by multiple, counter-rotating detonation heads. However, a limited range of conditions with injector B and the CR = 1.93 nozzle exhibited sustained operation with a single detonation wave. To the authors' knowledge, this is the first demonstration of RDWC operation with a single wave using natural gas and air as propellants.

3. PERFORMANCE CHARACTERIZATION OF A NATURAL GAS-AIR ROTATING DETONATION ENGINE

This chapter has been previously published in the Journal of Propulsion and Power [56].
DOI: https://doi.org/10.2514/1.B38087

3.1 Introduction

The possibility of achieving thermodynamic cycle efficiencies greater than traditional gas turbine and rocket combustors has motivated recent interest in pressure-gain combustion (PGC) cycles, wherein gas expansion is constrained during heat release to achieve a cycle-averaged total pressure increase [8], [13]. The rotating detonation engine (RDE) has received particular interest because it operates with quasi-steady flow and is geometrically similar to existing engine architectures. In an RDE, one or more detonation waves propagate transverse to incoming reactants, typically in an annular chamber. Detonation speeds of order 1-2 km/s produce typical cycle frequencies of 1-10 kHz in air-breathing RDEs and require injector designs that can dynamically respond to passing detonation waves through high injection pressure drops or fluidic valving due to the high pressures behind the shock-coupled reaction front. The high reaction front propagation velocities produce thermal power densities greater than deflagrative combustors and permit new integration approaches for propulsion system design. However, PGC systems must compete against modern gas turbine and rocket engines, which have benefited from decades of incremental technology development. Furthermore, modeling and design of an RDE remains difficult due to the complex coupling of fluid mechanic and chemical kinetic processes inherent to the cycle, and due to strong sensitivities to geometric parameters.

Two principal challenges in the development of RDEs are achieving operation at engine-relevant conditions as well as quantifying (and subsequently optimizing) performance so that the theoretical pressure gain can be achieved in practical systems. While a number of studies have been conducted on a range of combustor designs, most have focused on laboratory-scale conditions or readily detonable propellants [7], [15], [17], [18], [20], [21],

[57]. However, interest in RDEs operating with natural gas-air mixtures for land-based power generation gas turbine engines has presented additional challenges. The chemical kinetics of these reactants make them difficult to detonate, as characterized by their cell size of 300 mm at standard conditions. Bykovskii *et al.* [22]–[24] conducted studies of a 500 mm RDE with syngas and mixtures of methane with hydrogen. While the combustor was able to operate with co-rotating waves for mixtures that were less than 70% methane by mass, greater fractions of methane produced counter-rotating waves or external combustion. Roy *et al.* [58] similarly studied air-breathing RDE operation with natural gas-hydrogen mixtures in a 150 mm combustor, but found it was only able to support detonation with mixtures that were at least 85% hydrogen. While preheating the air and operating at a chamber pressure of 0.3 MPa produced more stable operation, it failed to expand the range of operable natural gas concentrations. The limited range of operable natural gas mass fractions was attributed to significant increases in the chemical induction time and thereby detonation cell size as the natural gas concentration increased, until the cells outgrew the combustor hardware scale.

Quantifying the performance of PGC systems and RDEs has proven difficult due to the inherently unsteady nature of operation and high-enthalpy gas flows exiting the combustor. A number of methods have been proposed for evaluating the net pressure gain based on measurement of outlet flow conditions or combustor thrust production. Recent research has applied laser diagnostics to obtain temporally resolved measurements of exhaust plume velocity [59] and of temperature and species content [60], although measurement of combustor thrust production remains a standard method of performance evaluation. Kaemming and Paxson developed the Equivalent Available Pressure (EAP) method of estimating the net pressure gain produced by a combustor based on thrust measurements and applied it to simulation results to demonstrate the sensitivity of pressure gain to combustor geometry, heat release, and non-axial momentum [61]. Bach *et al.* applied this technique to a laboratory-scale hydrogen-air RDE to show that experimental measurements follow the same trends as simulations with respect to combustor geometry [62]. TenEyck [63] also analyzed experimental thrust measurements using the EAP methodology and observed similar sensitivities to combustor area ratios. He then used design correlations for flame holder pressure drop to show that the measured pressure loss was comparable to combustor designs typical of ramjets

or afterburners, suggesting that RDEs can achieve performance comparable to traditional combustors for these applications. Finally, Baratta and Stout [64] recently demonstrated operation of a low-loss RDE and measured a total pressure drop of less than 5% between the reactant plenum and combustor exhaust, also using the EAP method.

Application of thermodynamic models to the RDE cycle is key to elucidating the parameters that affect device performance, as is the case for any power conversion technology. A number of analytic models of RDE performance have been proposed, providing insight into different aspects of the cycle including parasitic loss mechanisms, component integration, and flight vehicle performance [55], [65]–[68]. For example, Braun *et al.* presented a model used to study the performance of an RDE for ramjet applications [68]. Stechmann *et al.* analyzed the performance of RDEs in rocket applications, with particular emphasis on the effects of nozzle integration and propellant selection [65]. The study implemented an unsteady outflow model to assess the effect of the transient blowdown process inherent to PGC cycles on nozzle performance. The analysis of Kaemming *et al.* focused on the effect of loss mechanisms on device performance, including deflagration burning, exit flow distortion, lateral relief in the detonation front, and secondary shocks [55]. Their study accounted for these loss mechanisms by tracing the independent thermodynamic pathways present in an RDE and compared the results to performance measurements from experiments and numerical simulations to establish model efficacy. Appropriate application of such thermodynamic models will be critical to development of an RDE capable of achieving a pressure gain, which has not yet been demonstrated in the open literature.

The present study seeks to apply a thermodynamic model to elucidate the factors that affect RDE pressure gain for a generic combustor and subsequently compare its predictions to integral performance measurements. Measurements of thrust, chamber pressure, and wave dynamics were conducted on a combustor developed to operate at the flow conditions of land-based power generation gas turbines, with natural gas and air as the reactants, chamber pressures up to 2 MPa, and air preheat temperatures up to 800 K.

3.2 Experiment Description

3.2.1 Test Article

A combustor was developed to study RDE operation with natural gas and air reactants at a mean chamber pressure up to 2 MPa. The system permits variation of reactant flowrates, stoichiometry, reactant types, system backpressure, and air pre-heat temperature. A cross section of the combustor is shown in Fig. 3.1, with basic dimensions labeled. The outside diameter of the RDE chamber is 228 mm, with a 19 mm annular gap and length of 130 mm.

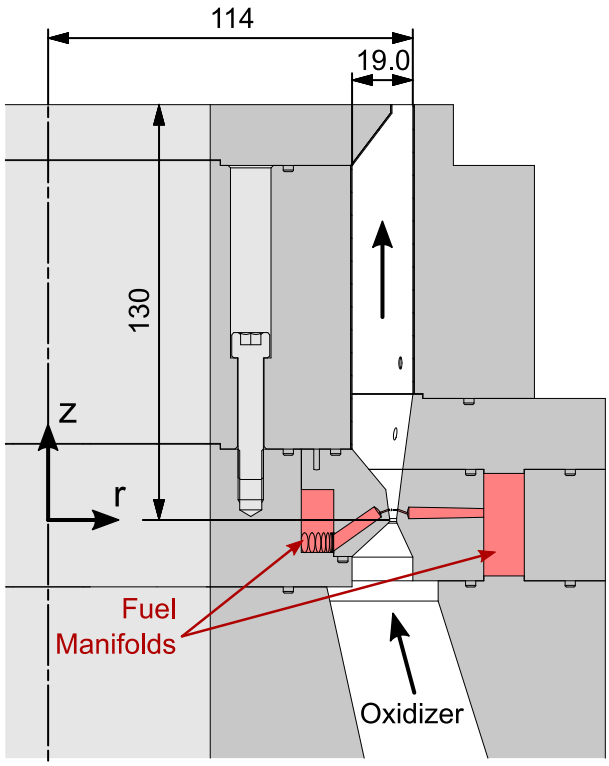

Figure 3.1. Cross section of RDE test article with major dimensions labeled (in mm).

The combustor was tested with axial and sting injector designs, respectively denoted A and B in Fig. 3.2. Both designs inject the oxidizer through circumferential slots at the head end of the chamber with fuel injection orifices shortly downstream of the oxidizer throat. The centrally-located sting in injector B creates two axial air slots. Design A injects fuel from both the inner and outer circumference of the combustion chamber and design B injects fuel from the middle of the combustion channel into both axial air slots. Additional details about

the combustor and injector design along with supporting analysis are provided in Walters *et al.* [12].

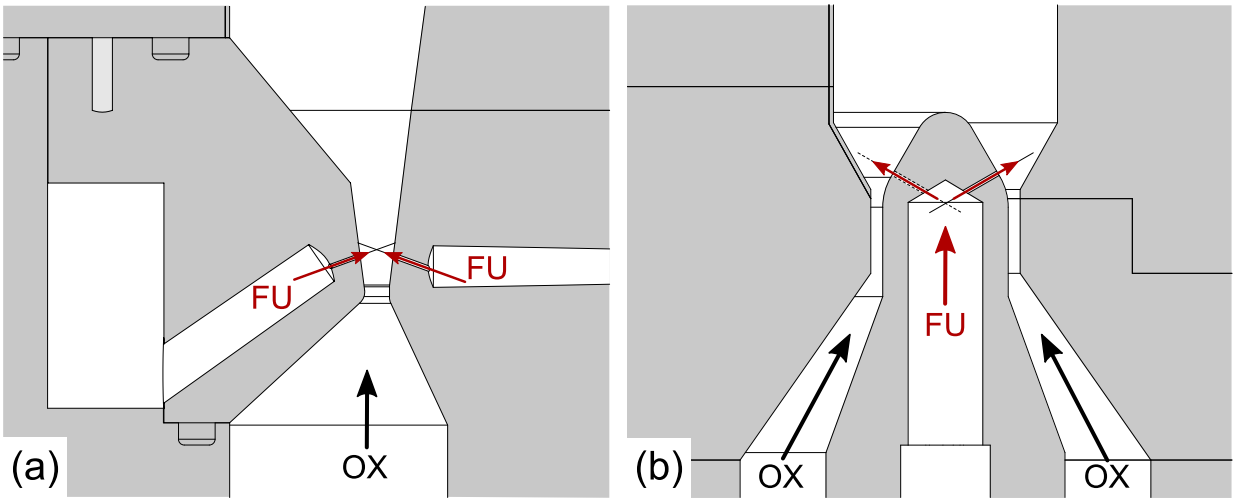

Figure 3.2. Detailed schematic of combustor head end geometry for axial injector A (a) and sting injector B (b) with arrows highlighting the flow of fuel (FU) and oxidizer (OX).

Test operations were conducted on a thrust stand installed at the Maurice J. Zucrow Laboratories [27], [28], which also provided requisite propellant supply systems. The test platform can supply of up to 10 kg/s of non-vitiated, heated air to the test article with commensurate flows of natural gas, gaseous oxygen, nitrogen, cooling water, and other gaseous fuels. The air flow can be enriched with additional oxygen up to a mass fraction of oxygen in the oxidizer flow of $Y_{O_2}^{Ox} = 40\%$, compared to $Y_{O_2}^{Ox} = 23.2\%$ for pure air. Increasing the oxygen content of the oxidizer can increase the range of operability for less detonable propellants by reducing the chemical induction timescale and thereby the detonation cell size [2]. Natural gas is sourced from a local pipeline, while oxygen is supplied by manifolds of high-purity cylinders. The mole fraction of major species in the natural gas supply reported by the distributor are averaged each month to compute fuel composition. The composition of natural gas for these experiments was CH_4 92.4%, C_2H_6 6%, N_2 1%, CO_2 0.3%, and C_3H_8 0.3%. This mixture was used for calculations of natural gas flowrate and mixture stoichiometry.

The mass flow rates of fuel and oxidizer are metered by critical flow venturi nozzles (CFVNs) that conform to ASME and ISO specifications [30], [69]. The mass flowrate is computed using Eq. (4-3) of [69],

$$\dot{m} = \frac{C_d A_{th} C_R^* P_t}{\sqrt{(R_u/MW)\, T_t}}, \tag{3.1}$$

where C_d is the discharge coefficient, A_{th} is the throat area, C_R^* is the real gas critical flow function, R_u is the universal gas constant, and MW is the species molecular weight. The pressure and temperature are monitored throughout each test and then corrected to total conditions, P_t and T_t respectively, using the diameter ratio between the CFVN throat and upstream tubing. The real gas critical flow function, C_R^*, is a nondimensional constant relating the CFVN throat mass flux to the upstream stagnation conditions. All fluid thermophysical properties, including C_R^*, are computed using the NIST Reference Fluid Thermodynamic and Transport Properties Database (REFPROP) [31], as recommended by [69]. This approach uses a high-accuracy real-gas equation of state to determine the critical flow function under the assumption of isentropic flow with constant total enthalpy. Departure from an ideal gas equation of state can be significant at pressures and temperatures typical for CFVN operation, particularly for species with high critical temperatures, such as methane.

Uncertainty of mass flow rates, and subsequently operating conditions, are computed using the Kline-McClintock method of uncertainty propagation [32]. Uncertainty of a dependent variable is computed as

$$u_y = \sqrt{\sum_{\mathrm{i}} \left(u_{x_\mathrm{i}} \frac{\partial y}{\partial x_\mathrm{i}} \right)^2} \tag{3.2}$$

where x_i are the independent variables and u_{x_i} is the corresponding uncertainty. Partial derivatives are evaluated numerically using a central difference scheme to propagate uncertainties through all steps of calculating flowrates, including through REFPROP when computing the real gas critical flow factor and other fluid properties. All sources of uncertainty considered for computing flowrates are enumerated in Table 3.1. The analysis follows recommendations in [69], [70], where uncertainty sources are labeled as Type A to indicate

that they are computed using statistics, or Type B to indicate that they are evaluated using other methods. Total uncertainty of each mass flow rate is approximately 0.8% with a 95% confidence interval. This results in a typical uncertainty in operating conditions of 0.5% of total mass flux, 0.9% of equivalence ratio, and 0.1% of mass fraction of oxygen in the main oxidizer flow.

Table 3.1. Sources of uncertainty for mass flowrate calculations.

Quantity	Uncertainty Type	Uncertainty Source
Pressure	A	100 ms average with 95% confidence interval
	B	0.04% Full-Scale (GE UNIK 5000 Premium Accuracy transducer)
Temperature	A	100 ms average with 95% confidence interval
	B	Greater of 1.1K or 0.4% of reading (Omega Special Limits of Error Type K thermocouple)
Molecular Weight	A	Only applied for natural gas, and based on constituent uncertainty from 1-month average
Throat Diameter	B	Manufacturer tolerance of 0.013 mm
Throat to Upstream Diameter Ratio	B	Derived from throat diameter uncertainty and assumed 1% uncertainty of upstream diameter
Discharge Coefficient	B	0.3% Correlation accuracy [30], [69]
Critical Flow Function	B	0.025% REFPROP database accuracy [69]

Combustion is initiated by injection of a detonation wave into the chamber from an external pre-detonator [33]. The shock-coupled reaction front ignites the main chamber reactant flows, which are established prior to initiation to reduce transient effects of valve actuation, regulator response, and manifold priming. A short startup transient follows wherein the number and direction of detonation waves is observed to vary on a per-cycle basis. After the transient, limit-cycle operation establishes with one or more rotating detonation heads in the main combustor. Combustion is terminated by replacing the fuel flow with an inert gas purge. The steady-state test operation is approximately one second, which provides a statistically significant number of detonation cycles for analysis while ensuring hardware survivability in the absence of active cooling measures.

3.2.2 Instrumentation and Diagnostics

The experiment is remotely monitored and controlled using a National Instruments (NI) based data acquisition and control system. Analog inputs from pressure transducers, thermocouples, and thrust stand load cells are recorded using a 16 bit analog to digital converter (NI PXIe-6375). The data system also provides auto-sequenced control with redline monitoring for valve actuation and set-point control of electronic regulators for closed-loop feedback control of pressure upstream of CFVNs. All experiment control and condition monitoring operates at a frequency of 1 kHz [27]. High-frequency pressure and timing measurements were recorded with an independent NI data acquisition system that provides non-multiplexed readout on up to 32 channels at frequencies up to 2 MHz.

Measurement of the thrust generated by the combustor was conducted using a Force Measurement Systems single component axial thrust stand. The stand is outfitted with an Interface 2000-D-10K-4-U load cell to measure thrust loads up to 44 kN. Correction for tares from plate flexures, fluid lines, and instrumentation cables is achieved via an *in-situ* hydraulic calibration system using an identical load cell. Deviation from the applied calibration load is less than 5 N across the calibrated range, including effects of nonlinearity and hysteresis. A Vishay Model 2100 strain gauge conditioner system is used to amplify the millivolt signal from the load cells for recording by the data system.

To evaluate RDE performance during combustor development, it is valuable to decouple the performance of the combustor from any installation effects or downstream components, such as an expansion nozzle. One such effect is the interaction of the exhaust plume with a bluff-body combustor, which has been shown to produce sub-atmospheric pressures (base drag) on aft-facing surfaces of the combustor [71]. It is therefore necessary to measure the local pressure on combustor aft surfaces so that the measured thrust can be corrected for the base drag. The base pressure on combustor aft surfaces was measured with seven GE UNIK 5000 pressure transducers, which have a range of 200 psi and full-scale accuracy of 0.04%. The location of the base pressure ports are indicated in Fig. 3.3 as EAP-01 through EAP-07.

The thrust of warm reactants exhausting from the chamber prior to ignition could not be directly measured with the current configuration due to thermal expansion of preheated air pipes parallel to the thrust-line applying an unknown load to the thrust stand metric bed. Instead, the load cell measures the thrust increment from pre-ignition conditions to steady-state combustion. An auxiliary test determined that the thrust of steady reactant flow prior to ignition could be calculated by evaluation of the thrust equation based on measured chamber conditions and mass flowrates. This test also determined that the natural frequency of the live bed assembly is approximately 33 Hz. A 4^{th} order Butterworth band-rejection filter is applied to remove the effect of stand resonances, as they are not relevant to performance calculations. This also permits a more appropriate estimate of measurement variation for uncertainty analysis.

Reported gross thrust measurements, F_g, are then composed of three components: the load cell measurement corrected using the calibration system and filtered to remove stand resonances, the computed reactant thrust of warm reactants prior to ignition, and base drag measured during each test. The base drag component was typically 10-20% of the gross thrust in the current measurements, while the load cell measurement varied between 40-60% and reactant thrust accounted for the balance. An example summation of each component for computing the gross thrust, F_g, is included in Section 3.4.1.

An error analysis similar to that used in computing uncertainty of mass flowrates and operating conditions was conducted for gross thrust measurements. Precision uncertainty of base pressure and load cell measurements were determined by averaging over 100 ms intervals during each test run. The manufacturer supplied transducer accuracy was used as the bias uncertainty of base pressure measurements. Bias uncertainty of load cell readings was assigned a value of 10 N to account for manufacturer quoted accuracy and the observed residual of ± 5 N during daily calibrations. An additional uncertainty of 2% of the inert propellant flow thrust correction was added based on the residual between the computed and measured thrust during the auxiliary cold flow test. After accounting for the enumerated error sources, the typical relative uncertainty in gross thrust was 1.5% with a 95% confidence interval.

The RDE is instrumented with an array of low-and high-frequency pressure transducers within the combustion chamber and propellant manifolds. Pressure fluctuations were measured with water cooled piezoresistive transducers (Kulite WCT312M-3000A), which have a reported element natural frequency of 1.65 MHz. Prior studies have shown that it is difficult for transducers to survive in the preferred, flush-mount configuration due to the high heat fluxes associated with detonative combustion [16], [46]. Therefore, the transducers are installed in a recessed cavity with a resonant frequency > 50 kHz, which provides a measurement of detonation pressure with lower amplitude attenuation and phase lag than a comparable semi-infinite tube pressure installation while protecting the instrument [47]. Each transducer was sampled at a frequency of 1 MHz to provide a high level of temporal resolution. Transducer port locations in the combustion chamber and propellant manifolds, along with the coordinates of each port with respect to the indicated r$-$z$-\theta$ coordinate system are shown in Figure 3.3. The origin of the z-axis coincides with the oxidizer injector throat, as shown in Fig. 3.1. Reported measurements refer to the instrumentation port number to specify transducer location.

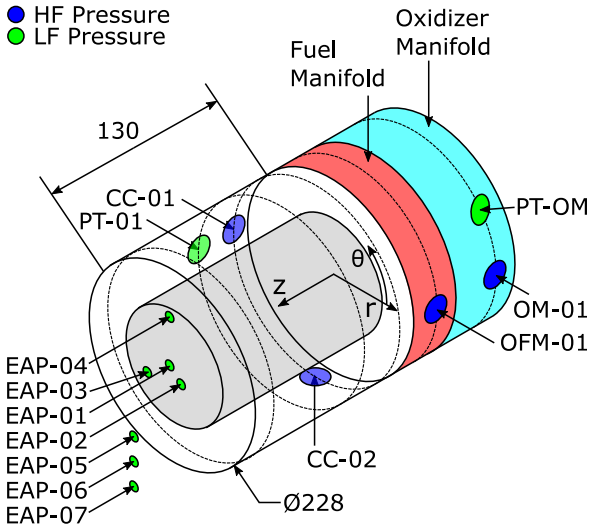

Port	Location	θ, deg	z, mm	r, mm
OM-01	Oxidizer Manifold	0	-41	114
OFM-01	Outer Fuel Manifold	0	-2	114
CC-01	Chamber	180	27	114
CC-02	Chamber	270	27	114
PT-OM	Oxidizer Manifold	-	-	-
PT-01	Chamber	180	49	114
EAP-01	Chamber Aft	-	130	0
EAP-02	Chamber Aft	330	130	32
EAP-03	Chamber Aft	210	130	64
EAP-04	Chamber Aft	90	130	89
EAP-05	Chamber Aft	165	130	133
EAP-06	Chamber Aft	180	130	174
EAP-07	Chamber Aft	180	130	216

Figure 3.3. Transducer port locations and coordinates on combustor (dimensions in mm).

The wave dynamics in the chamber are visualized by direct imaging of the combustor annulus. Images are recorded at 44 kHz with a resolution of 256 x 256. Broadband chemi-

luminescence from the chamber is collected by a 500 mm focal-length, $f/5.6$ objective lens (Nikon AF-S 200-500mm) and imaged by a Phantom v411 high speed CMOS camera. These images are used to provide topological information about the combustor dynamics, including the number of detonation waves and the corresponding wave velocities.

3.3 Analysis Approach and Results

3.3.1 Performance Model

A simplified model of the RDE thermodynamic cycle was developed to characterize the influence of combustor geometry and operating conditions on device performance. The model was adapted from that of Kaemming *et al.* by removing loss mechanisms due to shocks, deflagration burning, and outlet flow distortion [55]. The resulting model estimates the performance of an ideal RDE and reduces the number of empirical parameters. Figure 3.4 shows thermodynamic station numbers relative to a representative combustor geometry.

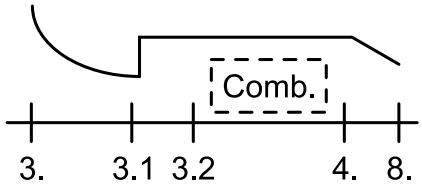

Figure 3.4. Diagram showing station numbers for the thermodynamic cycle model.

The temperature-entropy diagram of Fig. 3.5 shows the components of the model cycle along with the cycle of an ideal, constant pressure (CP) combustor for comparison. The two cycles are based on identical inlet flow conditions and combustor geometry. A description of the simplified model is included here, but the full model including loss mechanisms and detailed rationale can be found in [55]. The model requires an iterative solution procedure where the inlet and outlet flowrates are balanced by adjusting the assumed pressure immediately ahead of the detonation wave, $P_{3.2}$. Propellant manifold total state conditions (T_{t3}, P_{t3}) are required inputs. The temperature ahead of the detonation wave is then given as

$$T_{3.2} = \frac{T_{t3}}{1 + \frac{\gamma_R - 1}{2} \max M_{3.1}^2} = \frac{2T_{t3}}{\gamma_R + 1}, \tag{3.3}$$

where γ_R is the ratio of specific heats for the reactants and the second equality is based on the observation that the maximum injection Mach number, $M_{3.1}$, is unity for all studied configurations. he fluid temperature immediately ahead of the detonation wave will likely be greater than that given by Eq. (3.3) in a real system due to product gas recirculation and potential deflagration burning [7]. However, numerical simulations show that Eq. (3.3) is an appropriate approximation for the ideal case where these loss mechanisms are ignored [72]. The Chapman-Jouguet (CJ) conditions (T_{CJ}, P_{CJ}) are then computed from the initial state $(T_{3.2}, P_{3.2})$, assuming equilibrium thermochemistry using NASA CEA [73].

The flowrate of reactants into the chamber is determined using a time-dependent inflow model. The sub-model assumes a pressure-time history that exponentially decays from P_{CJ} to $P_{3.2}$ according to

$$P_{3.1}(t) = P_{3.2} + (P_{CJ} - P_{3.2})\,\mathrm{e}^{-kt}, \tag{3.4}$$

where k is a tuned time-constant parameter. The Mach number of propellants entering the chamber is then

$$M_{3.1}(t) = \min\left[1, \sqrt{\frac{2}{\gamma_R - 1}\left(\left(\frac{P_{t3}}{\min\left(P_{3.1}(t), P_{t3}\right)}\right)^{\frac{\gamma_R - 1}{\gamma_R}} - 1\right)}\right], \tag{3.5}$$

where the pressure has been limited to prevent imaginary results and the Mach number has been limited to one to produce choked flow. The mass flowrate of reactants into the combustion chamber during the wave period, T, is

$$\dot{m}_{in} = A_{3.1} P_{t3} \sqrt{\frac{\gamma_R}{R_R T_{t3}}} \int_0^T M_{3.1}(t) \left(1 + \frac{\gamma_R - 1}{2} M_{3.1}^2(t)\right)^{-\frac{\gamma_R + 1}{2(\gamma_R - 1)}} dt. \tag{3.6}$$

Equation (3.6) neglects any injector backflow resulting from the high pressure behind the detonation wave, an assumption consistent with the objective of presenting a simplified performance model.

The detonation wave is modeled as a normal shock (station 3.2 - station vN) followed by heat addition (station vN - station CJ) to the Chapman-Jouguet point, in accordance

with the Zel'dovich-von Neumann-Döring theory [2]. However, the resulting peak pressure and temperature do not represent a steady condition from which work is extracted. This process instead occurs through an unsteady blowdown, where each pressure and temperature state corresponds with an infinitesimal mass packet. The work available for extraction from downstream of the detonation can then be computed by modeling this time-dependent blowdown process or using an appropriately averaged mean state. Paxson and Kaemming [13] further establish that the appropriately averaged state is set by the mass-averaged total temperature of products and demonstrate that this must equal the constant pressure adiabatic flame temperature for a generic PGC device. Each method of computing the work available for extraction has advantages. For example, Stechmann *et al.* approximated the unsteady blowdown to investigate nozzle integration in an RDE [65]. The current model is intended to study global system performance and therefore computes the appropriately averaged mean state.

The conditions of this mean state are computed from the CJ condition by accounting for the "shock work." For an unsupported, freely propagating detonation, as in an RDE, an expansion must occur behind the detonation front to provide the thrust necessary to support propagation of the leading shock [2], [14]. Mathematically, this is a result of the Galilean transformation from the wave-fixed frame of reference to the laboratory frame of reference. While energy is conserved across a non-reacting normal shock in the shock-fixed frame, a shock propagating through a quiescent medium increases the static temperature and velocity of the flow, and hence the total enthalpy in the laboratory frame. Thus, the shock has done work on the fluid. It is assumed that the energy transferred to the fluid by the shock is equal to the energy required to sustain its propagation and is therefore not available to do work. Finally, it can be shown that the total specific enthalpy increase is equal to $V^2/2$, where V is the shock propagation velocity [74]. The shock work is then modeled as an expansion immediately following the CJ point (station CJ - station 4.). The resulting temperature is computed as

$$T_{t4} = T_{CJ} + \frac{a_{CJ}^2 + u_{3.1}^2 - D_{CJ}^2}{2c_{p,P}}, \tag{3.7}$$

where a_{CJ} is the speed of sound at the CJ conditions, $u_{3.1} = \max M_{3.1}(t)\sqrt{\gamma_R R_R T_{3.2}}$, the reactant inflow velocity, and D_{CJ} is the CJ detonation wave velocity. The expansion from the CJ state to T_{t4} is modeled as isentropic, resulting in a post-combustion total pressure of

$$P_{t4} = P_{CJ}\left(\frac{T_{t4}}{T_{CJ}}\right)^{\frac{\gamma_P}{\gamma_P - 1}}. \tag{3.8}$$

Finally, the mass flowrate of products out of the combustion chamber is computed assuming choked flow, giving

$$\dot{m}_{out} = A_8 P_{t4}\sqrt{\frac{\gamma_P}{R_P T_{t4}}\left(\frac{2}{\gamma_P + 1}\right)^{\frac{\gamma_P + 1}{\gamma_P - 1}}}. \tag{3.9}$$

Simulations have shown that RDE exhaust does not remain precisely choked, but that the assumption is appropriate on average provided that the overall pressure ratio, P_{t3}/P_∞, is sufficient [61]. Furthermore, it is a conservative approximation that results in the lowest possible pressure, P_{t4}, required to exhaust a given propellant flowrate from the combustion annulus. The inlet and outlet mass flowrates are then compared to check convergence of the assumed pressure ahead of the detonation wave, $P_{3.2}$. The assumed pressure is adjusted and the calculation repeated until flowrates have been balanced within a relative tolerance of 0.01%.

The conditions following the expansion for shock work (station 4.) represent the thermodynamic state that is available to do work. Inspection of Fig. 3.5 shows that this state lies above the propellant manifold pressure isobar, indicating that a pressure gain has been achieved. In comparison, the heat addition isobar for the constant pressure cycle lies slightly below that of the manifold pressure, producing the expected total pressure loss. As expected from the previous discussion, the total temperature of the appropriately averaged state in the RDE cycle is approximately equal to the adiabatic flame temperature of the constant pressure cycle. Any differences in the work available for extraction is then a result of the different pressures at this condition. That is, while $P_{t4}^{RDE} \neq P_{t4}^{CP}$, $T_{t4}^{RDE} \approx T_{t4}^{CP}$, where deviations in temperature are the result of different product gas mixtures and properties. While the model predicts that an RDE operating with the particular geometry and flow conditions

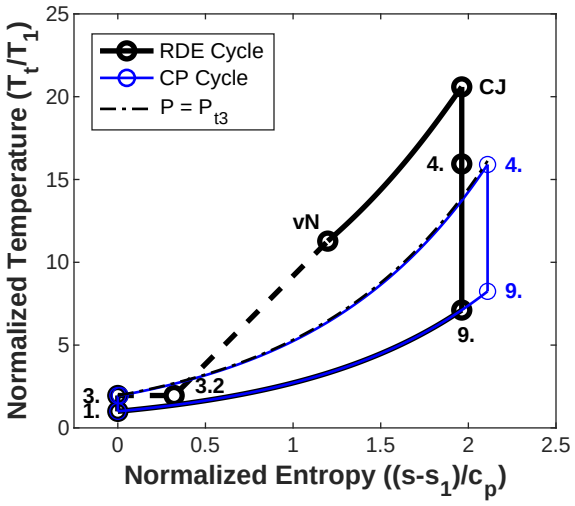

Figure 3.5. Temperature-entropy diagram showing the thermodynamic cycle of the RDE model and an ideal, constant pressure cycle operating at the same conditions.

used to generate Fig. 3.5 produces a pressure gain relative to the propellant manifold total pressure, this is not always the case.

3.3.2 Performance Metrics

Several methods of evaluating RDE performance have been proposed, with the aim of quantifying the pressure gain or loss from experiments and computations. These include the Equivalent Available Pressure (EAP) methodology developed by Kaemming and Paxson [61] and the thrust efficiency outlined by Stechmann *et al.* [65]. Both of these methods will be explained and evaluated for application to the current study.

The EAP method computes the total pressure that would produce the measured thrust when expanded to the combustion chamber outlet. For a combustor with no expansion region, this corresponds to thermodynamic station number 8 at the exhaust throat. The method assumes unity Mach number at this station, which was shown to be a conservative approximation that underpredicts EAP by 10% at most. The EAP is then given as

$$EAP = \frac{\frac{F_g}{A_8} + P_\infty}{\gamma_P + 1} \left(\frac{\gamma_P + 1}{2} \right)^{\frac{\gamma_P}{\gamma_P - 1}}, \tag{3.10}$$

where F_g is gross thrust and P_∞ is the ambient pressure. The EAP is then compared to manifold total pressure to determine if the combustor produces a positive pressure gain. Comparison to the manifold stagnation pressure produces a performance metric that treats the RDE as a system which includes losses from its injector. While this approach assumes equal stagnation pressures for all reactants, the oxidizer manifold pressure can reasonably be considered representative for air-breathing RDEs due to the disparity in fuel and oxidizer flowrates. A weighted average of the fuel and oxidizer supply pressure may be required for rocket-type RDEs with a higher fuel mass fraction. The net pressure gain across the system is then computed as

$$Pressure\ Gain\ (PG) = \frac{EAP}{P_{t3}} - 1, \tag{3.11}$$

where EAP is computed from Eq. (3.10) and P_{t3} is the total pressure measured by PT-OM. By this convention, a negative pressure gain corresponds to a total pressure loss. The EAP computed from thrust measurements has recently been applied in a number of experimental efforts to quantify the total pressure difference across an RDE [62]–[64].

The combustor thrust efficiency, η_F^{Comb}, is a second approach for evaluating RDE performance proposed in [16], [65]. It compares the thrust generated by an RDE to an ideal, constant pressure combustor operating with the same nozzle exit area, A_8, and same total propellant mass flowrate, $\dot{m}$. This ideal thermodynamic model overpredicts CP combustor performance compared to real systems because it ignores typical loss mechanisms. Nevertheless, it was chosen for this study to highlight conditions for which an RDE could outperform any CP combustor without consideration of device-specific factors. As a performance metric, the combustor thrust efficiency assumes that an RDE has achieved a pressure gain when it produces more thrust than the corresponding CP combustor such that $\eta_F^{Comb} > 1$. However, the imposed restriction of equal exit areas does not provide a consistent basis of comparison between RDE and CP combustors. The following analysis demonstrates that the combustor thrust efficiency will equal unity for an ideal RDE. That is, this parameter is unable to identify when a pressure gain has been achieved and is therefore not a useful performance metric for the current study.

Using the same assumptions as the model, η_F^{Comb} can be evaluated analytically. In particular, the RDE and CP combustors are assumed to operate with choked exit flow with no nozzle or expansion ($M_8 = 1$). The combustion product properties, γ_P and R_P, are assumed equal as mixture property differences are a secondary effect. In accordance with the assumption of steady outflow applied in the thermodynamic model, the analysis begins from the thrust equation for steady flow,

$$F = \dot{m}u_8 + (P_8 - P_\infty)A_8, \tag{3.12}$$

and appropriate relations can be substituted for unknown variables. As a result of the choked exit condition, the mass flowrate is given by Eq. (3.9), the sonic exit velocity results in $u_8 = \sqrt{\frac{2\gamma_P R_P T_{t4}}{\gamma_P+1}}$, and the exit plane pressure is computed with the isentropic relation $P_8 = P_{t4}\left(\frac{2}{\gamma_P+1}\right)^{\frac{\gamma_P}{\gamma_P-1}}$. Substituting and simplifying gives

$$F = A_8 P_{t4}\left(\sigma_F - \frac{P_\infty}{P_{t4}}\right), \tag{3.13}$$

where σ_F is introduced and defined as $\sigma_F = (\gamma_P + 1)\left(\frac{2}{\gamma_P+1}\right)^{\frac{\gamma_P}{\gamma_P-1}}$ to permit more compact notation. The RDE and CP combustor must have the same flowrate, such that

$$\dot{m}_{RDE} = \dot{m}_{CP} \rightarrow \frac{A_8^{RDE} P_{t4}^{RDE}}{\sqrt{T_{t4}^{RDE}}} = \frac{A_8^{CP} P_{t4}^{CP}}{\sqrt{T_{t4}^{CP}}}, \tag{3.14}$$

after substituting in Eq. (3.9) for each combustor type and simplifying. However, the total temperature of the RDE and CP products must be equal, as discussed in Section 3.3.1. Therefore, the flowrate equality can be further simplified to

$$A_8^{RDE} P_{t4}^{RDE} = A_8^{CP} P_{t4}^{CP}. \tag{3.15}$$

The ratio of the thrust generated by the RDE and CP combustors can now be written as

$$\frac{F_{RDE}}{F_{CP}} = \frac{A_8^{RDE} P_{t4}^{RDE}\left(\sigma_F - \frac{P_\infty}{P_{t4}^{RDE}}\right)}{A_8^{CP} P_{t4}^{CP}\left(\sigma_F - \frac{P_\infty}{P_{t4}^{CP}}\right)} = \frac{\sigma_F - \frac{P_\infty}{P_{t4}^{RDE}}}{\sigma_F - \frac{P_\infty}{P_{t4}^{CP}}}. \tag{3.16}$$

For the combustor thrust efficiency, the mass flowrate and exit area are held fixed as mentioned previously. Since $A_8^{RDE} = A_8^{CP}$, Eq. (3.15) simplifies to $P_{t4}^{RDE} = P_{t4}^{CP}$ and

$$\eta_F^{Comb} = \frac{F_{RDE}}{F_{CP}}\bigg|_{\dot{m},\ A_8} = 1. \tag{3.17}$$

As Eq. 3.17 demonstrates, the combustor thrust efficiency of an ideal RDE will be unity as a result of the constant flowrate and exit area. Therefore, the combustor thrust efficiency is unable to distinguish when an RDE outperforms an ideal CP combustor, or when a pressure gain has been achieved. In contrast, the pressure gain computed using the EAP normalized by the reactant manifold total pressure in Eq. (3.11) will clearly demarcate both of these points. As PGC cycles deliver a performance benefit through increased pressure, any figure of merit for quantifying their benefit must do so in this context. Normalizing measured work output by the driving potential in the system as a baseline, in this case P_{t3}, provides the context necessary to quantify the pressure gain.

An alternative method could compare the thrust from RDE and CP combustors while holding the reactant mass flowrate and manifold pressure fixed, as this provides an appropriate connection to the reference driving potential. This performance metric, or "system thrust efficiency," can be evaluated in a manner similar to the combustor thrust efficiency to assess its relationship with the pressure gain of Eq. (3.11). Starting from Eq. (3.16), the CP combustor injector is assumed ideal such that $P_{t4}^{CP} = P_{t3}$ and

$$\eta_F^{Sys} = \frac{F_{RDE}}{F_{CP}}\bigg|_{\dot{m},\ P_{t3}} = \frac{\sigma_F - \frac{P_\infty}{P_{t4}^{RDE}}}{\sigma_F - \frac{P_\infty}{P_{t3}}}. \tag{3.18}$$

Using Eq. (3.11), the percentage increase or decrease in thrust relative to the ideal constant pressure combustor, or "Thrust Gain," can then be written as

$$Thrust\ Gain\ (TG) = \eta_F^{Sys} - 1 = \frac{1 - \frac{1}{PG+1}}{\frac{P_{t3}}{P_\infty}\sigma_F - 1}. \tag{3.19}$$

Hence the system thrust efficiency and thrust gain are closely related to the pressure gain, as they incorporate appropriate normalization by the same driving potential in the system, P_{t3}. An RDE which has achieved a pressure gain will then produce a system thrust efficiency

greater than unity, or equivalently a positive thrust gain. For the assumed configuration of a development combustor without an expansion nozzle, Eq. (3.19) shows that the thrust gain decreases with increasing pressure ratio. In the limit of a vacuum ambient condition, a combustor operating without a nozzle would be unable to demonstrate a pressure gain on the basis of a thrust measurement. It would also be possible to relax the requirement of a lossless CP combustor injector and account for an assumed pressure drop representative of fielded systems when evaluating the thrust gain. This approach may prove insightful during a trade study evaluating the different combustor types. The current study will primarily use the pressure gain defined by Eq. (3.11) because pressure is a more relevant parameter in the motivating application of terrestrial power generation.

3.3.3 Model Results

Prior work has shown that the pressure gain depends strongly on the area ratios $A_{3.2}/A_{3.1}$ and $CR = A_{3.2}/A_8$, which are respectively the oxidizer inlet area ratio and the nozzle contraction ratio [61]–[63]. While the two area ratios have typically been considered independently, Fig. 3.6 shows that the pressure gain computed by a parametric survey of combustor geometries using CFD results presented by Kaemming *et al.* [61] can be collapsed by eliminating $A_{3.2}$, the combustor annulus area. The pressure gain that an RDE can produce appears to be intricately tied to $A_8/A_{3.1}$, the area ratio between the outlet and inlet of the combustor.

Figure 3.6 includes the pressure gain computed from CFD simulations using both the method of Eq. (3.10) (EAP) and a related method that uses the full thermodynamic and flow state available to a simulation (EAPi) [61]. Results from the performance model discussed in Section 3.3.1 are overlaid on Fig. 3.6 for ideal rotating detonation and constant pressure combustors. The ideal RDE pressure gain, indicated by the solid black line of Fig. 3.6, exhibits excellent agreement with the CFD results across the entire range of area ratios. The only flow variables that were matched with the simulations for this parameter sweep were the propellants (hydrogen and air), stoichiometry, and inlet total temperature. Analysis of the model equations determined that neither the mass flowrate nor manifold total pressure, P_{t3}, affected the predicted pressure gain for chamber pressures sufficient to choke the outlet

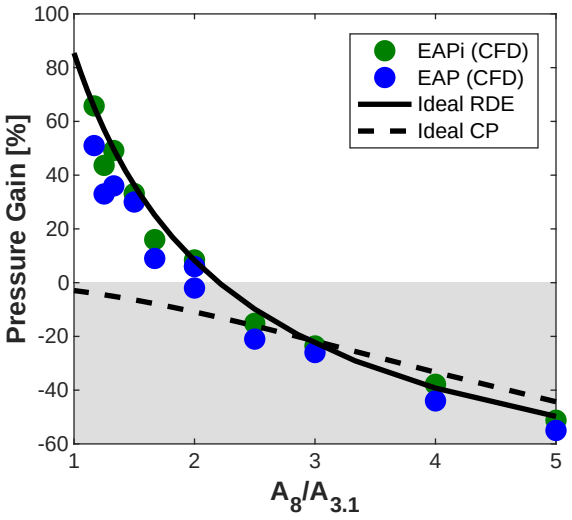

Figure 3.6. Comparison of pressure gain computed with thermodynamic model and reference CFD data [61].

flow. As a result, the only input parameters that affect the pressure gain predicted by the thermodynamic model are those matched between the simulation and model: the reactants, stoichiometry, and inlet total temperature.

The broken black line of Fig. 3.6 shows the pressure gain produced by a constant pressure combustor for comparison to the other results. As expected, the pressure gain for the CP combustor approaches zero as $A_8/A_{3.1}$ approaches unity, corresponding to an ideal injector. The maximum pressure gain is not precisely zero, as a pressure drop must exist to generate a nonzero massflow. The RDE and CP models reach a crossover point near $A_8/A_{3.1} = 3$, where both models forecast a 20% pressure loss. For greater outlet-to-inlet area ratios, the RDE is predicted to produce a lower pressure gain than a CP combustor operating with the identical flow conditions and geometry. However, for high-loss injectors where $A_8/A_{3.1} > 3$, the thermodynamic model also indicates that both combustor types will produce a very similar pressure loss. As a result, it will be difficult to distinguish a well-performing RDE and CP combustor on the basis of performance for high-loss configurations typical of most current experiments.

While Fig. 3.6 shows that low outlet-to-inlet area ratios are required for an RDE to achieve a pressure gain, it should be noted that this requirement can conflict with other design

objectives. Reducing this area ratio reduces the mean pressure ratio across the injector, which can increase the time required for reactant flow to reestablish after detonation passage. It will also change the average flow velocities and residence time within the chamber, which can affect combustor operability. Similarly, the specific injector inlet ($A_{3.2}/A_{3.1}$) and nozzle contraction ($A_{3.2}/A_8$) area ratios will each play a role in determining device operability and hence performance for a real system. For example, a lower injector inlet area ratio will promote coupling with the oxidizer plenum and can transition the RDE to a non-detonative mode of operation [62]. Prediction of these interactions is outside the scope of the simple model presented here. Development of a high-performance RDE will require consideration of the trade-offs between these competing requirements and objectives.

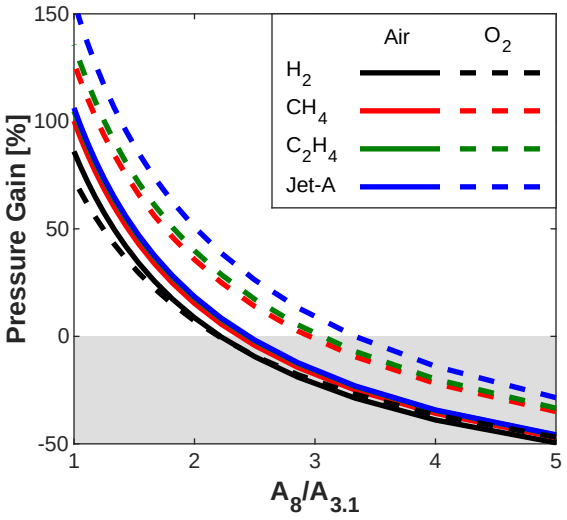

Figure 3.7. Comparison of pressure gain computed with thermodynamic model for different propellants.

Figure 3.7 presents pressure gain as a function of outlet-to-inlet area ratio for several reactant combinations, as the effect of propellant selection is not explored in the current experiments. Hydrogen, methane, ethylene, and vaporized Jet-A fuels with air and oxygen as oxidizers were selected because these propellant combinations have been widely considered or studied for RDE applications [6], [8], [16], [18]–[20], [23], [59], [75], [76]. Inlet flow conditions of $T_{t3} = 300$ K and $\phi = 1$ were used for the calculations. The trend for each reactant mixture is similar to that observed in Fig. 3.6 for hydrogen-air, where the pressure gain

rapidly decreases as the area ratio $A_8/A_{3.1}$ increases. Methane-air reactants are predicted to produce a marginally higher pressure gain than hydrogen-air for a given area ratio. Switching oxidizers to pure oxygen produces a significant increase in computed pressure gain for methane. Exchanging the oxidizer for a hydrogen-fueled combustor brings the pressure gain closer to zero, decreasing positive values and increasing negative values of pressure gain. The other hydrocarbon fuels, ethylene and vaporized Jet-A, exhibit similar trends as methane. For air-breathing conditions, the curves are almost identical to that of methane, while the model predicts that combustion with oxygen produces a greater increase in pressure gain than for methane. The similarity between the hydrocarbon fuels is not surprising, as they all have similar heating values and fuel mass fractions for each oxidizer.

The claim that RDEs are capable of achieving a thermodynamic cycle efficiency higher than current power and propulsion systems operating on the Brayton cycle is evaluated using the performance model. The thermal cycle efficiency can be written as,

$$\eta_{th} = 1 - \frac{c_P \left(T_9 - T_{t1}\right)}{\Delta h_v \left(f/a\right)}, \tag{3.20}$$

where Δh_v is the fuel heating value and f/a is the fuel-air mass ratio [13]. The constant pressure combustor shown in Fig. 3.6 has a cycle efficiency of 49% for an ideal injector, while the RDE cycle efficiency varies between 36-59%, depending on the outlet-to-inlet area ratio. The range of thermal efficiencies the thermodynamic model predicts for the ideal RDE then brackets the efficiency of the ideal CP combustor, which is expected based on the range of pressure gain shown in Fig. 3.6. The mechanism by which a PGC cycle can deliver increased thermal efficiency is via a higher effective overall pressure ratio, as Section 3.3.1 showed that the mass-averaged temperature of combustion products is the same as in a CP cycle.

3.4 Experimental Results

3.4.1 Performance Characterization

The combustor operational envelope and chamber dynamics were previously characterized in a broad parametric survey of operating conditions. Approximately 120 tests were conducted, the majority of which used natural gas with pure air that was not enriched with

additional oxygen. The range of tested conditions is summarized in Table 3.2. Further details about combustor operational sensitivities to propellant flowrate, oxygen enrichment, and equivalence ratio can be found in [12]. From this survey, a test case that exhibited stable operation with one detonation wave propagating in each direction was selected to demonstrate the data reduction and performance analysis method.

Table 3.2. Range of tested combustor operating conditions.

$G\ [kg/\left(m^2 \cdot s\right)]$	ϕ	$Y_{O_2}^{Ox}$ [%]	T_3 [K]	P_c [MPa]	$A_{3.2}/A_{3.1}$	$A_{3.2}/A_8$
200-500	0.85-1.2	23.2-35	575-800	0.7-1.8	8.6, 9.4	1.93, 2.75

The selected case was conducted with a chamber propellant mass flux of 250 $kg/\left(m^2 \cdot s\right)$, unity equivalence ratio, an inlet oxidizer temperature of 725 K, and pure air as the oxidizer. Figure 3.8a presents the pressure-time history recorded by the high-frequency transducers installed in the propellant manifolds and combustion chamber. The pre-detonator injects a detonation wave into the chamber and ignites the main chamber reactants at t = 0. After a short ignition transient (typically 10-20 ms), pressure fluctuations enter a limit cycle characteristic of one or more rotating detonation waves within the chamber. The pressure-time history in Fig. 3.8b shows steep-fronted wave forms with modulating peaks that decay to approximately the mean chamber pressure. The mean peak-to-valley chamber pressure fluctuation amplitude P/P_c [12], [50] was 2.8 times the mean chamber pressure of 0.82 MPa measured at PT-01, indicating the presence of strong detonations. This is corroborated by the average wave velocity of 1230 m/s, which is 68% of the CJ speed for these operating conditions.

The transducer located at CC-02 measures high amplitude pressure fluctuations of more than four times the mean chamber pressure throughout the duration of the test. Peak pressure amplitudes can reach three times the measured fuel and oxidizer manifold pressures. Simultaneously-acquired chemiluminescence images indicate that the intersection points of the counter-rotating detonation waves are located near $\theta = 90°, 270°$, which is aligned with CC-02. These locations are not geometrically aligned with any reactant injection or combustor feature and have been observed to change over the test duration for other flow conditions. The wave intersections produce high amplitude pressure peaks as the counter-rotating deto-

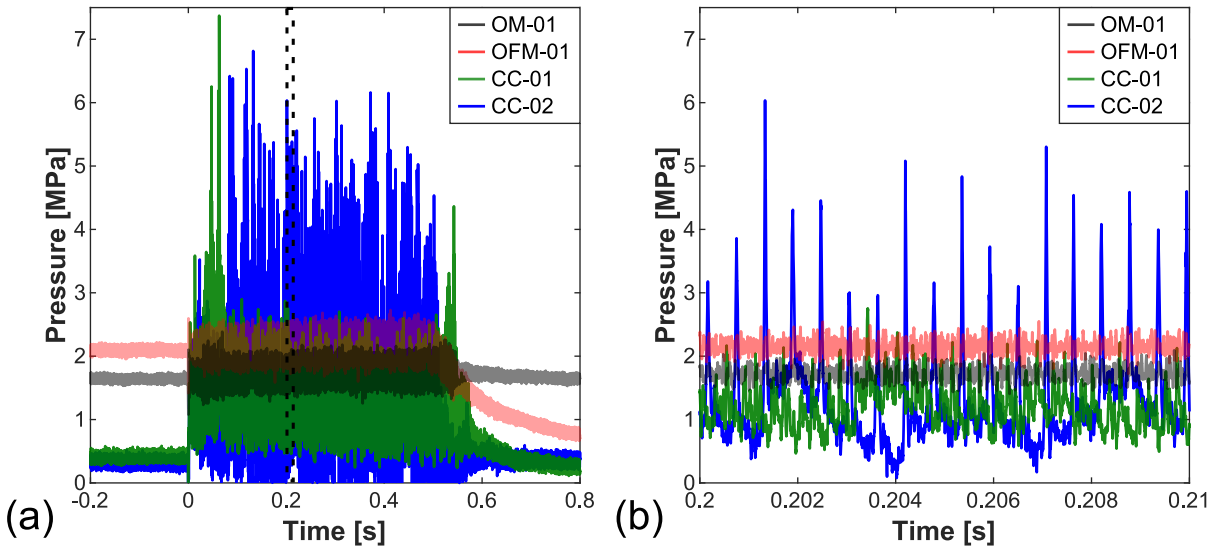

Figure 3.8. High frequency pressure measurements illustrating (a) test sequence and (b) steep fronted waves from rotating detonation waves in chamber.

nations interact and amplify the resulting pressure rise in a manner reminiscent of a reflected shock interaction.

Figure 3.9a shows an example segment of a detonation surface plot, where the pixel intensity distribution around the annulus circumference has been extracted from the high speed images and transposed onto a $\theta - t$ time history [48]. The lines with positive and negative slope correspond to detonation waves traveling in the $+\theta$ and $-\theta$ directions, respectively. The crosshatch pattern shows that the waves intersect near $\theta = 135°, 315°$ for the selected time window, while the regular line spacing indicates stable wave dynamics. The annulus image of Fig. 3.9b shows waves at $\theta = 100°, 170°$ shortly before an intersection event at $\theta = 135°$. The counter-propagating waves observed in this test are representative of most tests conducted with the combustor.

Figure 3.10 shows the pressure on aft-facing surfaces of the combustor relative to ambient conditions measured during the test. The probe locations correspond with those enumerated in Fig. 2.4. The flow of propellants prior to the start of combustion produces subatmospheric pressures on the combustor centerbody region, but has little effect on the surface pressure of the combustor outerbody. Ignition and the presence of rotating detonation waves in the

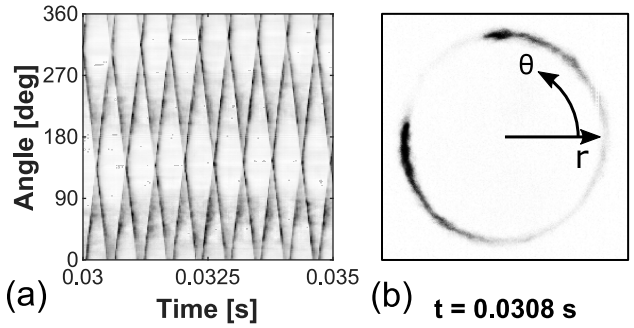

Figure 3.9. Detonation surface plot (a) and high-speed image (b) showing counter-propagating detonation waves.

chamber is observed to alter the pressure distribution on the centerbody, corresponding to probes EAP-01 through EAP-04. The pressure at probe locations EAP-02 and EAP-03 decreased to 25% below ambient atmospheric conditions. Recent experimental studies have observed similar subatmospheric pressures in the center bluff body region [63]. Harroun further conducted simulations to show that rotating detonation waves enhance the base region ejector effect compared to a steady flow [71]. The pressure on aft-facing surfaces outside of the combustor annulus are comparatively unaffected by the combustion processes in the chamber, in agreement with other experimental results [63]. The total base drag acting on the combustor bluff body, F_B, is then computed using an area-weighted sum of the measured base pressures.

The time-history of thrust in Fig. 3.11 shows the contribution of each component of the gross thrust, F_g, discussed in Section 3.2.2. The thrust of pre-ignition reactant flow is given as F_{flow} and computed using the chamber conditions and reactant mass flowrate immediately prior to ignition ($-0.3 < t < -0.1$ s). The thrust stand step response after filtering oscillations from the live bed resonance natural frequency of 33 Hz is represented by F_{LC} in red. Base drag, F_B, accounts for 14% of the gross thrust for this case, while the load cell measurement and computed reactant flow thrust each account for 43%. Across the range of tested conditions, the base thrust was observed to vary between 10-20% of the total gross thrust. This represents a significant decrement to the measured thrust and would result in severe performance under-prediction if the base drag is not measured. The thrust

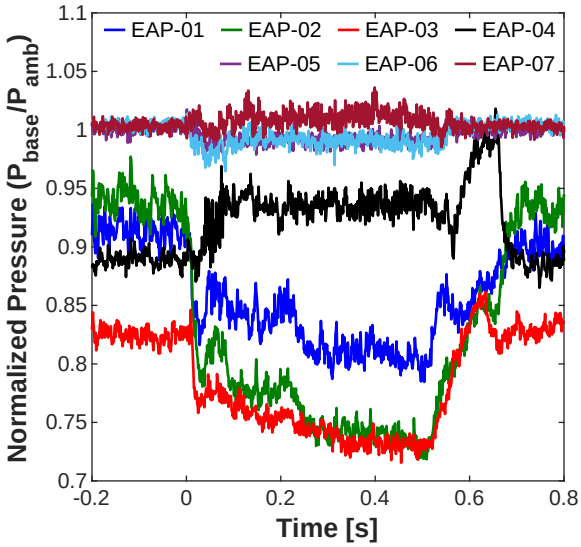

Figure 3.10. Raw base pressure measurements. Transducers in the legend top row correspond to locations on the combustor centerbody, while those on the bottom row lie outside the combustion annulus.

measurement signal exhibits significant unsteadiness during the RDE hot-fire, but averaging over a 100 ms window results in a gross thrust of 4.52 kN with a 2σ uncertainty of 1.7% after accounting for the error sources discussed in Section 3.2.2.

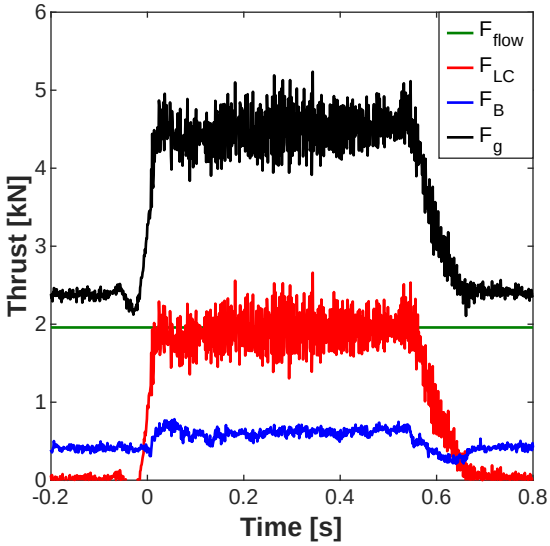

Figure 3.11. Breakdown of gross thrust into constituent components: reactant flow, load cell, and base drag.

The measured gross thrust F_g, nozzle throat area A_8, oxidizer plenum pressure p_{t3} measured at PT-OM, and estimated product ratio of specific heats γ_P, are then used to compute the net pressure gain according to Eqs. (3.10) and (3.11). The combustion product ratio of specific heats, γ_P, is estimated by averaging γ computed using equilibrium thermochemistry for a CJ detonation and a constant pressure combustor, which approximately bounds the range of possible values [73]. Uncertainty of pressure gain is computed through application of Eq. (3.2), where gross thrust uncertainty is computed as discussed in Section 3.2.2. The uncertainty in nozzle throat area is computed using measured part dimensions and an assumed deviation of twice the specified manufacturing tolerance to account for possible degradation during operation. Oxidizer plenum pressure uncertainty is computed using the measurement variance and manufacturer reported transducer accuracy. Finally, deviation in the value of γ_P is estimated as half the difference between the two specific heat ratios used in its computation. Combined, these error sources result in an average pressure gain absolute uncertainty of $\pm 0.8\%$ with a 95% confidence interval.

This test condition produces a net pressure gain of -46% relative to the oxidizer manifold with an absolute uncertainty of $\pm 1.3\%$ with a 95% confidence interval. As discussed in Section 3.3.2, the convention of Eq. (3.11) results in a negative value of pressure gain when there is a total pressure loss. For comparison, the test condition delivers a thrust gain (loss) relative to an ideal constant pressure combustor computed according to Eq. (3.19) of -9.2% with absolute error bounds of $\pm 1.6\%$.

3.4.2 Parameter Sensitivities

The sensitivity of RDE performance to controlled flow parameters was studied by comparing experimental measurements of pressure gain to predictions from the idealized model across the range of tested operating conditions. Reported pressure gain values for injector A have not been corrected for base pressure, as the requisite hardware was not installed during those tests. Each injector was tested in the natural gas RDE over a range of mass fluxes, oxygen mass fractions, and equivalence ratios, with each parameter varied independent of the others. Tests were conducted with an oxidizer inlet temperature either in the low range

of $T_3 = 600 - 675\ K$, or in the high range of $T_3 = 710 - 750\ K$. In the following plots, lines with markers denote experimental measurements while the solid and broken lines show the pressure gain predicted by the performance model for an RDE and CP combustor, respectively. Unfilled markers denote flow conditions that operated in a deflagrative combustion mode with no evidence of wave motion in chemiluminescence imaging. Error bars are not included because the typical uncertainty, evaluated in the same manner as Section 3.4.1, is $\pm 0.8\%$, less than the marker size.

Figure 3.12 shows the variation in combustor performance as the combustor annulus mass flux is increased. Injector A was operated with oxygen-enriched air with $Y_{O_2}^{Ox} = 28\%$ for this sweep, while injector B used pure air for both tested nozzle contraction ratios. All tests were conducted with $\phi = 1$ and an oxidizer inlet temperature between 600 and 670 K. The performance model predicts that net pressure gain for both combustor types is independent of the total propellant flowrate, or equivalently the propellant manifold pressure. Injector B closely follows this trend, with little variation in pressure gain as the mass flux is increased. While the trend for injector A is similar, a greater pressure loss is observed for $G = 250 - 300\ kg/\left(m^2 \cdot s\right)$. It is possible that the decrease is related to the transition from one to two counter-rotating waves propagating in each direction, which was observed to occur in this range of mass fluxes using the chemiluminescence imaging. For these conditions, injector B achieves a pressure loss 5-10 percentage points lower than model predictions while injector A is 10-15 points below predictions. As discussed in Section 3.3.3, the observed independence of combustor performance with respect to combustor mass flux was expected, as analysis of the model determined that pressure gain was independent of manifold pressure. This is a result of no loss mechanisms and the choked exit boundary conditions, which causes all pressures to rise proportionally as total flowrate is increased.

Enriching the oxidizer mixture with additional oxygen is generally expected to increase the net pressure gain, as the greater proportion of fuel for a given equivalence ratio will result in higher mass-specific heat release. This trend is observed in Fig. 3.13 for the theoretical combustor calculations and in Fig. 3.7 for the transition to pure oxygen. All tests included in this figure were conducted with $G = 250\ kg/\left(m^2 \cdot s\right)$ and unity equivalence ratio. Injector B follows the expected trend reasonably well for both nozzle contraction ratios. Exceptions

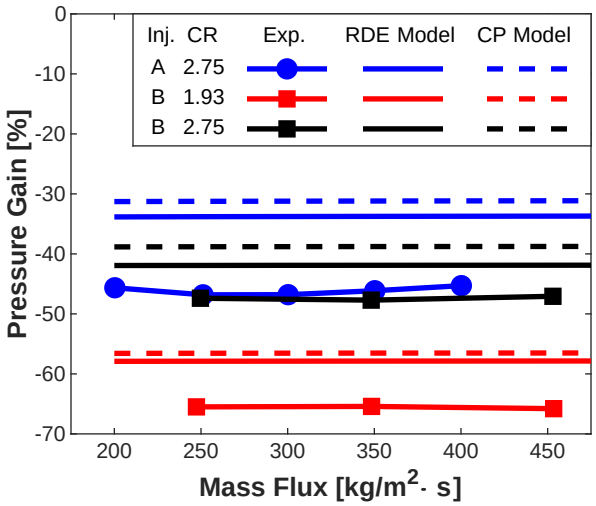

Figure 3.12. Combustor performance sensitivity to mass flux, G.

occur when the CR = 2.75 nozzle transitions to a deflagative combustion mode, and as conditions approach the corresponding transition point for the CR = 1.93 nozzle, just beyond $Y_{O_2}^{Ox} = 28\%$. Similar trends are not observed for injector A at either of the tested oxidizer preheat temperatures, $T_3 = 600 - 670\ K$ or $T_3 = 710 - 750\ K$.

However, increasing the propellant inlet temperature uniformly decreases both the predicted and measured pressure gain across the range of oxygen mass fractions. At these conditions, increasing the inlet temperature by approximately 100 K has an effect on pressure gain comparable to a 10% increase in $A_8/A_{3.1}$. The increased initial propellant temperature decreases the combustor pressure gain via two mechanisms. First, it results in a lower pressure ratio across the detonation wave. This can either be explained by reduction of initial density, or through reduction in the CJ Mach number and hence pressure ratio, as the reactant speed of sound is more sensitive than the detonation velocity to the initial temperature. Second, an increased inlet temperature increases the required manifold pressure for a given flowrate, while the mass averaged product temperature and associated pressure, T_{t4} and P_{t4}, are relatively unaffected.

Figure 3.14 shows the dependence of combustor performance on equivalence ratio, where a fixed mass flux of $G = 250\ kg/\left(m^2 \cdot s\right)$ and pure air were used for all tests. For this series, injector A was operated with $T_3 = 710 - 750\ K$ while injector B was operated in the low

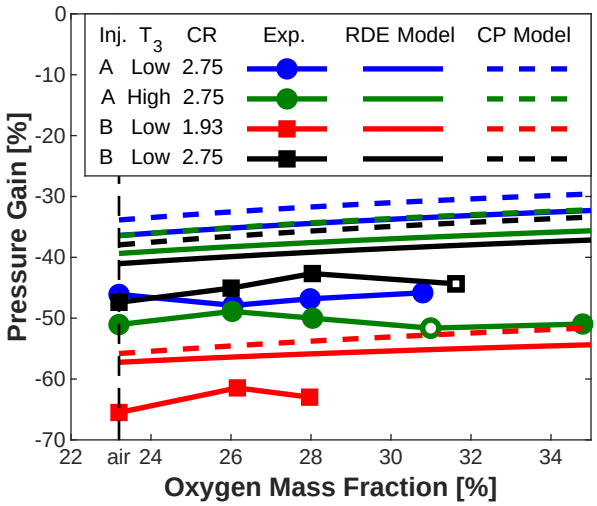

Figure 3.13. Combustor performance sensitivity to mass fraction of oxygen in oxidizer, $Y_{O_2}^{Ox}$. Unfilled markers indicate operating conditions that failed to produce rotating detonations.

inlet temperature range with $T_3 = 600 - 670\ K$. Similar to Fig. 3.13, injector B follows the trend predicted by the model while injector A does not. The relationship between pressure gain and equivalence ratio is the result of a similar mechanism as the oxygen mass fraction dependence. As the equivalence ratio shifts away from unity, near the maximum pressure gain, the heat release per unit mass decreases.

Injector B with the CR = 1.93 nozzle at $\phi = 0.9$ is the only test condition that produces a single detonation wave within the combustion chamber. The combustor returns to a counter-propagating mode as the equivalence ratio is increased to 0.95, similar to all other operating conditions. The transition results in a minor increase of net pressure gain from -68% to -67%, which is within the measurement accuracy. The similarity between these values suggests that for the selected conditions, the details of the wave propagation do not have a significant impact on the RDE propulsive performance. This may be related to the overall wave strength, as these conditions produced stable, but not high-order detonations. The single wave case ($\phi = 0.9$) exhibits a wave speed that is 58% of the CJ detonation velocity with pressure fluctuations of 2.2 times the mean chamber pressure, while the wave speed and pressure fluctuation amplitude were respectively 61% and 1.9 for the counter-propagating

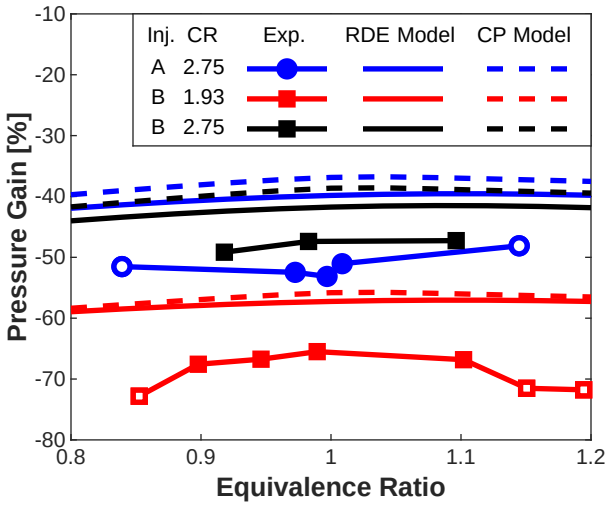

Figure 3.14. Combustor performance sensitivity to equivalence ratio, ϕ. Unfilled markers indicate operating conditions that failed to produce rotating detonations.

wave mode ($\phi = 0.95$). These tests were also conducted with a high-loss injector design, which limits the maximum achievable pressure gain and thereby plays a more important role in determining the performance than wave dynamics. As discussed in Section 3.3.3 and shown for these particular conditions in Fig. 3.14, the gap between RDE and CP combustor performance is quite small, supporting the conclusion that relative detonation quality has limited impact on pressure gain for high-loss systems.

A number of loss mechanisms present in experiments but ignored in the idealized thermodynamic model may contribute to the observed performance deficits for both injectors. Examples include incomplete mixing, mixture stratification, product gas recirculation into the reaction zone, and injector response dynamics [7], [62]. While it is difficult to ascribe specific aspects of the injector design to these potential mechanisms, comparative evaluation of performance trends can point to deficiencies. For all three varied operating parameters, mass flux, equivalence ratio, and oxygen mass fraction, the injector B performance generally followed the same trends as the thermodynamic model, while injector A did not. This suggests that an uncontrolled factor, potentially one of the possible loss mechanisms, plays a dominant role in determining the performance of injector A, rather than the mixture thermodynamics.

As shown in the injector schematics of Fig. 3.2, the fuel orifices for injector A are situated in a shallow diverging region downstream of the oxidizer throat followed by a rapid expansion to the combustion annulus width. In comparison, injector B has a shorter, continuous transition from the oxidizer throat to the chamber cross section with fuel orifices located further into the expansion region. Two plausible outcomes from these design differences are that injector A has an increased susceptibility to product gas recirculation due to the aggressive expansion, and a reduced ability for the fuel supply to respond to the chamber dynamics due their comparatively sheltered location in the shallow expansion. The operability analysis presented by Walters *et al.* [12] further concluded that injector B mixes the reactants more effectively than injector A on the basis of the respective sensitivities to mixture chemical kinetics. It then seems likely that one or multiple of these loss mechanisms, mixing efficiency, exhaust gas recirculation, or injector dynamic response, contribute to the observed performance deficit for injector A.

Though multiple factors may contribute to the disparity in measured performance relative to idealized calculations, the effect of the injector discharge coefficient can be quantified with the current measurements. While the model assumes an injector discharge coefficient of unity, injector A has a discharge coefficient of approximately 0.9, while it is 0.8 for injector B. This effectively reduces the injector throat area, $A_{3.1}$, corresponding to an increase in the outlet-to-inlet area ratio, $A_8/A_{3.1}$, by 11% and 25% for injectors A and B, respectively. The change moves the RDE operating point further to the right along the line of Fig. 3.6 and reduces the theoretical pressure gain by 5-10 percentage points. The sensitivity of RDE pressure gain to the outlet-to-inlet area ratio is contrasted against the above parameter studies, which demonstrated comparatively low sensitivity to combustor operating conditions. This underscores the role of the outlet-to-inlet area ratio as the most important parameter governing RDE pressure gain.

3.4.3 Global Trends

Global trends in combustor performance can be used to better understand differences between the two tested injectors. Figure 3.15 presents a scatter plot of relative pressure gain

against the detonation cell size colored by pressure fluctuation amplitude. The cell size was estimated for each test condition using the correlation developed by Walters *et al.* [12]. The relative pressure gain is computed as

$$RPG = \frac{PG_{exp.} + 1}{PG_{model} + 1} = \left(\frac{EAP}{P_{t3}}\right)_{exp.} \cdot \left(\frac{P_{t3}}{P_{t4}}\right)_{model}, \tag{3.21}$$

and compares the experimentally measured net pressure gain to that predicted by the performance model at the same operating conditions.

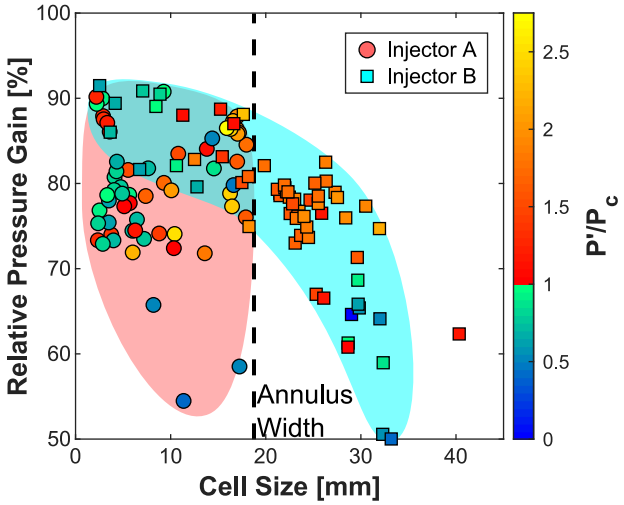

Figure 3.15. Scatter plot of relative pressure gain and estimated detonation cell size colored by pressure fluctuation amplitude. Shaded regions highlight points associated with each injector type.

Inspection of Fig. 3.15 revealed that test points were approximately grouped according to their injector type. The corresponding regions are shaded to highlight the resulting trends. There appears to be a trend between estimated cell size and relative pressure gain for injector B, while points corresponding to injector A show no apparent trend with the cell size parameter. The trend for injector B suggests that reducing cell size improves combustor performance relative to theoretical predictions, until it is similar to the chamber gap dimension. Further reductions, which were typically the result of oxygen enrichment, resulted in a high relative pressure gain that was coupled with transition to a deflagrative combustion mode. This supports the notion of the detonation cell size as an approximate scaling parameter

whose specific value does not necessarily determine the operability or performance of an RDE. Adequate operation and performance can be achieved once the cell size is of a similar scale as the combustor annulus width.

Injector B is able to operate across a wide range of relative pressure gain and estimated cell sizes, while injector A typically operates in a more narrow range. The differences may be explained in terms of the relative effectiveness of the two injector designs. Injector A seems to support moderate performance across a wide range of conditions, while injector B is able to achieve higher performance when operated at the correct flow parameters. However, these trends do not explicitly capture details about the ability of the injector design to produce robust, rotating detonation waves. While select conditions using injector A generated the fastest detonation waves and highest pressure fluctuation amplitudes observed with this combustor, all conditions produced counter-propagating wave dynamics. Injector B was able to produce a single, co-rotating wave for lean equivalence ratios, but the waves were typically slower across the tested conditions.

While the current measurements do not demonstrate a pressure gain, it is promising that two, quite different, and unoptimized injector designs approach the performance predicted by an ideal performance model. The combustor also has a length of 130 mm, resulting in a thermal power density ten times greater than existing systems [77]. Furthermore, the majority of these tests were conducted with natural gas and pure air, a propellant combination that is difficult to detonate and presents challenges for RDEs. Finally, the dependence of net pressure gain on the combustor outlet-to-inlet area ratio, $A_8/A_{3.1}$, provides direction for development of high-performance combustors.

3.5 Conclusions

Performance of a high pressure, natural gas-air RDE was investigated using measurements of thrust combined with high frequency pressure measurements and imaging of detonation wave motion in the combustor annulus. Experimental results were compared to an idealized RDE performance model. Analysis of common performance metrics demonstrated the necessity of normalizing by the propellant manifold conditions for any consistent evaluation of

RDE performance. PGC systems achieve a performance benefit through increased pressure, so it is necessary to normalize work output by the propellant manifold pressure, the driving potential in the system, for a performance metric to be capable of identifying a pressure gain.

Predictions of RDE pressure gain using the thermodynamic performance model closely matched results from numerical simulations and revealed that the pressure gain depends strongly on the area ratio between the exit and inlet of the combustor. Analysis using the model showed that it is difficult to distinguish a well-performing RDE operating with a high-loss injector from a constant pressure combustor on the basis of performance. Application of the model to different propellant combinations showed that fuel selection had minimal effect on the pressure gain of air-breathing RDEs, but more significant effects for rocket-type RDEs operating with oxygen.

Measurements of net pressure gain using the equivalent available pressure methodology were compared with model predictions to evaluate the effect of operating conditions on RDE performance. Injector B (incorporating transverse injection from a centrally-mounted "sting") performance followed trends predicted by the model, while injector A (employing transverse jet injection from both sides of the channel) generally did not. Combined with a global analysis of relative pressure gain for each injector across all tested conditions, this supported the conclusion that operation of injector A is controlled by an secondary process, likely reactant mixing. The global analysis also highlighted the effect of detonation cell size as an approximate scaling parameter, where detonative combustor operation is possible as long as the cell size is of a similar scale as the annular gap. The similarity between trends observed in the experiments and predicted by the thermodynamic model is promising for an RDE operating with less detonable reactants, namely natural gas and air. While a pressure gain was not demonstrated, the results elucidate the methods of analyzing RDE performance and point to avenues of future development that could lead to an optimized, integrated rotating detonation combustor.

4. FLOW AND PERFORMANCE ANALYSIS OF A NATURAL GAS-AIR ROTATING DETONATION ENGINE WITH HIGH-SPEED VELOCIMETRY

This chapter has been accepted for publication in Combustion and Flame [78].
DOI: https://doi.org/10.1016/j.combustflame.2021.111549

4.1 Introduction

The potential of achieving thermodynamic cycle efficiencies and thermal power densities greater than traditional combustors has motivated recent interest in rotating detonation engines (RDEs) [6], [8]. Computational and experimental studies have explored a range of applications, including gas turbines, ramjets, and rockets [7], [17]. However, further work is required to advance RDE technology to a readiness level where the cycle benefits can be realized in an integrated propulsion or power system. The recent review of Anand and Gutmark [9] provides an overview of pending challenges, including dynamic injection and mixing, detonation propagation in non-ideal conditions, operation with application-relevant reactants and corresponding conditions, highly-unsteady transonic exhaust, and system integration. Furthermore, no experiment in open literature has successfully demonstrated a pressure gain relative to the reactant supply necessary to attain the desired thermodynamic advantages. Continued progress will require computational modeling in concert with experimental investigation of the tightly coupled physics driving detonation structure, dynamics, and performance.

The structure and propagation dynamics of detonation waves in an RDE are the result of interaction between chemical kinetics and unsteady injection and mixing, which is inextricably linked to the cycle. High pressures behind the detonation front induce reactant flow cessation, resulting in a dynamic injection process where fresh reactants must enter the combustion annulus and mix prior to subsequent wave arrival. Mixing between incoming reactants and products from previous waves is likely to occur in the turbulent flowfield, potentially initiating auxiliary reactions that can compete with the detonation [7], [79]. These

tightly coupled processes have been observed to produce a range of combustion modes, including one or more co- or counter-rotating detonation heads [16], [80]. Imaging of the combustion annulus has revealed interactions between waves as well as mode transitions, where the number or direction of waves change in a transient event [18], [20]. For example, experiments by Bleumner et al. [80] identified a progression from counter-rotating waves of equal strength to a single detonation front wherein one of the counter-rotating waves becomes weaker, splits into multiple fronts, and eventually disappears as the mass flowrate of reactants is increased. These regimes were classified based on the relative wave velocity as counter-rotating waves at equal speed, transitioning counter-rotating waves, single-wave with counter-rotating components, and single-wave. Other experiments have observed a cascading sequence of wave bifurcations with increasing flowrate, where wave velocity increases until nucleation of a new co-rotating wave accompanies a drop in velocity [7].

The structure of single and co-rotating detonation waves has been studied through extensive experiments and numerical simulations. Early imaging of broadband chemiluminescence using motion compensated photography techniques provided qualitative insight into the flowfield, revealing a detonation wave front with an attached oblique shock wave propagating into a triangular refill region [7]. Simulations supported these observations and have been used to interrogate the flow physics, boundary conditions, and thermodynamic processes occurring within RDEs [14], [81]. Later experiments acquired images of OH* chemiluminscence and mid-infrared radiation to make quantitative measurements of the wave height, oblique shock angle, and reactant refresh height and characterize their sensitivity to operating conditions [15], [82]. Phase averaging has also been applied to resolve the circumferential detonation structure using combustion annulus images and point pressure transducer probes, as in Bohon et al. [18]. Finally, recent experiments have used combustor flame imaging in conjunction with differences in wave arrival at axially distributed pressure transducers to reconstruct the wavefront structure for several different reactant combinations in a hollow combustor [83].

Despite their prevalence in experimental studies of RDEs, the structure of counter-rotating wave modes has not been studied as extensively as co-rotating waves. While counter-rotating fronts of equal strength are frequently observed to propagate at or near the speed

of sound of combustion products [80], sustained propagation at speeds of up to 70% of the reactant mixture Chapman-Jouguet velocity has been observed in an RDE operating with natural gas and air [12]. Some experiments have observed conditions that support a disparity in velocities between the two counter-propagating waves. Bleumner et al. [80] hypothesized that the weaker wave propagates as a shock between intersections with the main detonation front, creating a local explosion that energizes both waves for the ensuing lap. Optically accessible combustors have permitted direct observation of the wave structure, demonstrating that counter-rotating detonation waves propagate in the same axial plane, producing complex wave interactions [15], [23]. In computations, counter-rotating waves have been observed to fail in two-dimensional simulations [84], which may suggest that they are a fundamentally three-dimensional phenomena and that a corresponding flowfield is required to support their propagation [9]. Recent three-dimensional simulations of hollow RDEs have focused on the appearance of counter-rotating waves and analyzed the instantaneous process of wave interaction [85], [86].

Application of high-speed diagnostics has permitted rapid progress in understanding the structure and dynamics of detonation waves in RDEs, as well as their effect at downstream boundaries. In addition to the high-speed imaging discussed above, non-intrusive laser-based techniques have provided quantitative, time-resolved measurements within the combustion chamber and at the combustor exit plane. Laser absorption spectroscopy has been applied to acquire time-resolved point measurements of reaction product concentration, temperature, and pressure at repetition rates ranging from 20 kHz up to 3 MHz [60], [87]–[89]. While instantaneous measurements, frequency analysis, and average fuel consumption are typically reported, these studies were primarily focused on development and demonstration of the diagnostic technique. Recent work has conducted simultaneous measurement of gas temperature at four axially distributed probe locations in a hydrogen-air RDE [90]. Three conditions with increasing mass flowrate were analyzed to extract phase-averaged reconstructions of the unwrapped temperature field, which were qualitatively similar to those observed in numerical simulations. Further analysis estimated the fraction of combustion products in the pre-detonation mixture and pointed to the role of exhaust gas recirculation in depressing the detonation velocity, temperature, and pressure from Chapman-Jouguet equilibrium

conditions, as is commonly observed in experiments and detailed simulations. Particle image velocimetry (PIV) has also been applied to measure the time-history of flow velocity at the exit plane of an RDE combustor, though initial attempts encountered challenges with seed density and illumination, resulting in frequent vector dropout [91]. Journell et al. [59] used a burst-mode laser to resolve these issues, revealing periodic azimuthal velocity fluctuations synchronized to the wave cycle, while the axial velocity component exhibited high levels of turbulence. In addition to providing a fundamental understanding of flow structure, wave dynamics, and combustor performance, time-resolved measurements also provide direct quantitative means of comparison with high-fidelity models which permit more detailed analysis of wave structure and performance [92]–[95]. Experimental measurements of flow variables, such as velocity and temperature, are necessary to anchor detailed models and build confidence in their validity prior to use in combustor design.

Despite significant progress in understanding the fluid mechanic and combustion processes that govern RDE operation, consistent methods of quantifying RDE performance required to conclusively demonstrate their thermodynamic benefits have remained elusive. Recent work has highlighted the necessity of comparing RDE performance to the system driving potential, typically the reactant manifold supply pressure, for determining whether a combustor has produced a pressure gain [56]. The Equivalent Available Pressure (EAP) methodology [61], which computes a hypothetical, steady pressure consistent with the experimentally measured thrust, has gained acceptance as one method of making this comparison [56], [62], [64], [96], [97]. For example, Fievisohn et al. [97] provided a detailed presentation of the application of the technique, including experiment design and uncertainty quantification. Experiments applying the EAP method, in conjunction with simplified models, have also highlighted that the pressure gain an RDE can achieve is largely determined by the area ratio between the reactant inlet and combustor outlet [56], [96]. While these insights have enabled significant progress, the currently reported best-performing RDE still operates with a total pressure loss of 5% [64], below the threshold necessary to achieve the long-sought pressure gain.

Understanding the connection between local flow dynamics and global combustor performance is necessary to develop integrated RDE systems. Current methods of performance

measurement rely on globally integrated quantities, which necessarily make assumptions that systematically underestimate the potential work output due to the unsteady, transonic flowfield found in RDEs. The objective of this paper is then to investigate the front and flow structure of single and counter-propagating wave modes in a natural gas-air RDE operating at a mean chamber pressure of $p_c = 0.7MPa$. Natural gas presents challenges for airbreathing RDEs because its primary constituent, methane, does not readily detonate in air. However, the challenges associated with less-detonable reactants are expected to be more representative of those encountered as RDE technology progresses toward fielded systems. Procedures for adapting a combustor design from readily-detonable (e.g. hydrogen-air, methane-oxygen) to less-detonable (e.g. natural gas-air, methane-air) reactant combinations have not been established. Therefore, the current work focuses on such conditions where there has been limited prior application of advanced diagnostics. High-speed PIV is applied in the RDE exhaust plume with simultaneous measurements of the circumferential wave structure to interrogate the instantaneous and phase-resolved flowfield. The wave-resolved measurements are used to quantify the effect of wave propagation mode on flowfield structure and combustor performance. The presented velocimetry provides an experimental interrogation of a critical boundary condition through direct measurement of a primitive flow variable in an RDE. The measurements further enable quantitative examination of RDE performance and flow using the novel analysis framework derived herein.

4.2 Experiment Description

4.2.1 Hardware

A natural gas and air fired RDE was operated at the Purdue University Maurice J. Zucrow laboratories [27], [28]. The combustor was designed to operate with mean chamber pressures up to 2 MPa while supporting parametric variation of reactant flow rate, stoichiometry, and air preheat temperature. Figure 4.1 shows a cross section of the combustor. The annular combustion chamber has an outside diameter of 228 mm, annular gap of 19 mm, and length of 118 mm. Reactants are introduced using a 'sting' injection system, where air is fed axially through two, coaxial circumferential slots separated by a centrally located sting

which injects fuel through discrete orifices into the expansion region downstream of each slot at the chamber head end. Non-vitiated, heated air is supplied by a heat exchanger while natural gas fuel is sourced from a local pipeline. The ratio of combustion annulus area to injector area is 9.4 for this injector configuration, while the contraction ratio is 1.93 between the chamber and exit nozzle throat. Additional details about the combustor, injector, and fluid supply systems are provided in Walters et al. [12].

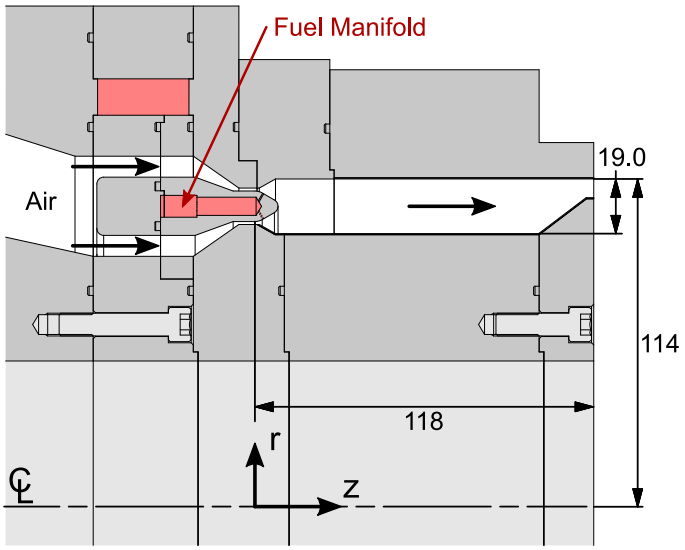

Figure 4.1. Cross section of RDE test article with major dimensions labeled (in mm).

The mass flow rate of reactants and combustor thrust are critical integral quantities that will anchor performance analysis based on the PIV measurements. The mass flow rates of reactants are metered with critical flow venturi nozzles that conform to ASME specifications [69]. The RDE is installed on a single-component thrust stand outfitted with a load cell (Interface 2000-D-10K-4-U) for measurement of the combustor net thrust. Aft facing surfaces of the chamber are instrumented with static pressure ports to isolate the thrust produced by the RDE from exhaust plume flow effects, which have been shown to produce suction on bluff-body combustors [71]. Uncertainty in flow rate and thrust measurements are computed according to the procedure outlined by the ISO "Guide to the expression of uncertainty in measurement" [70], accounting for contributions from Type A (computed using statistics) and Type B (evaluated using other methods) uncertainty sources. Typical

relative uncertainties of mass flow rate and gross thrust are 0.8% and 1.5% respectively, each with a 95% confidence interval. A complete enumeration of considered uncertainty sources has been previously provided by Walters et al. [56].

4.2.2 Diagnostic Arrangement

Figure 4.2 shows a schematic of the RDE labeled with instrumentation locations and the diagnostic arrangement. Pressure fluctuations in the reactant manifolds and combustion chamber are monitored with high frequency pressure transducers (Kulite WCT312M-3000A) sampled at 2 MHz at multiple axial and circumferential locations. The transducers are installed in a recessed cavity with a resonant frequency > 50 kHz, which reduces the amplitude attenuation and phase lag compared to a semi-infinite tube pressure installation while protecting the instrument from the high heat fluxes associated with detonative combustion [16], [46], [47]. Biases introduced by the installation method preclude quantitative interpretation of the resulting dynamic pressure measurements as the thermodynamic state within the combustion chamber, though relative values can provide directional sensitivities. Wave dynamics in the chamber are visualized by direct imaging of the combustor annulus with a CMOS camera (Phantom v411) operating at a repetition rate of 44 kHz and resolution of 256×256. Broadband chemiluminescence from the chamber collected by a 500 mm focal-length, $f/5.6$ objective lens (Nikon AF-S 200-500 mm) provides information about the wave number, topology, and velocity. While the spatial resolution of the chemiluminescence imaging is likely coarser than the computed lower bound of 1 mm/pixel, this proved sufficient for tracking the wave location throughout the test duration.

PIV measurements were conducted using a Nd:YAG-based master oscillator power amplifier Pulse-Burst Laser (PBL) system (Spectral Energies QuasiModo) and high-speed CMOS camera (Phantom v2512). The PBL provided a 10 ms doublet pulse train of 532 nm light at a repetition frequency of 100 kHz, yielding approximately 1000 vector fields. At this repetition rate, the laser delivers 3 mJ of energy per pulse. The beam was expanded and collimated using two cylindrical lenses in a telescope arrangement and then focused using two additional cylindrical lenses. Details of the optical arrangement are included in Fig. 4.2.

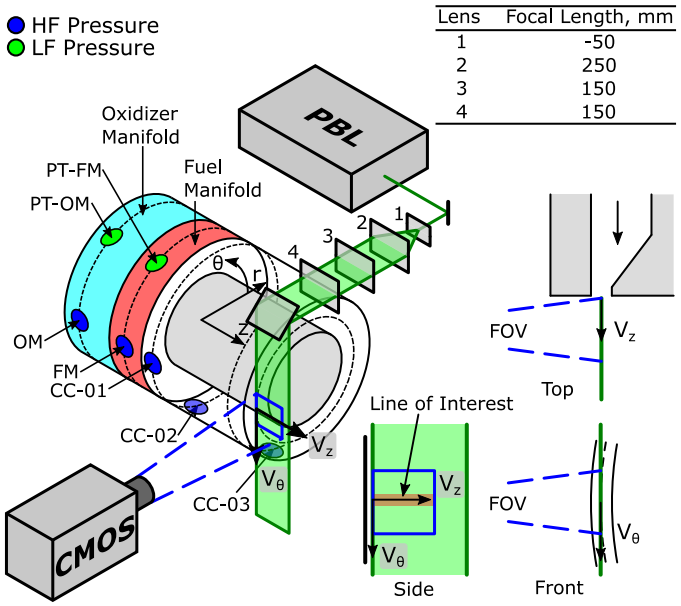

Figure 4.2. Schematic of combustor, instrumentation port locations, and diagnostic arrangement.

The laser sheet was focused just beyond the measurement plane to achieve a near-constant laser sheet thickness of $600\,\mu m$ while avoiding an increase in particle drop-out near the beam waist. The air flow was seeded with 200 nm zirconia (ZiO_2) particles, and the Mie scattering signal was imaged using a 200 mm $f/4.0$ lens (Nikon AF Micro NIKKOR) with a 3-nm FWHM bandpass filter. The CMOS camera collected images with a resolution of 256×256 pixels at 200 kHz, with a $4.23\,\mu s$ exposure and doublet pulse separation time of $1.5\,\mu s$. The 200 nm zirconia particles will respond to a fluid timescale of 50 kHz, equal to the Nyquist frequency of the velocity measurements [98]. This is sufficiently removed from the timescales of interest, which are of the same order as the wave circumscription frequency of approximately 1.5 kHz, that any risk of particle agglomeration was deemed acceptable.

Image spatial calibration, pre-processing, cross-correlation, and vector post-processing were executed using a commercial multi-pass adaptive-windowing software package (LaVision DaVis 8.3). Vector post-processing applied a three-pass universal outlier detection median filter to remove spurious vectors, where final vector fields had approximately 80-90% first choice vectors and an average correlation peak ratio greater than two. A final interrogation window size of 32×32 pixels with 75% overlap yielded a vector spacing of 1.6 mm. This

vector field resolution was considered sufficient given the combustor size (228 mm outside diameter) and average axial flow velocity of 1000 m/s, which corresponds to a flow displacement of 10 mm between measurements. For both cases, the average statistical correlation uncertainty in axial and azimuthal velocity components was 4% and 8%, respectively [99]. No periodic trend in uncertainty was observed relative to the wave cycle. PIV accuracy was further evaluated by comparing the measured velocity at non-reacting flow conditions with the expected, sonic velocity. The exhaust velocity averaged over the 10 ms of PBL operation was 435 ± 2 m/s with a 95% confidence interval, which deviates less than 1% from the computed sonic velocity of 439 m/s for the upstream total temperature of 575 K.

Figure 4.2 shows the PIV system arrangement, where the camera field of view (FOV) is centered at the $\theta = 180°$ position and the V_θ vector component is oriented in the local $+\theta$ direction. The radial velocity at the RDE exit was not resolved by the current, two-component PIV measurements. However, three-dimensional numerical simulations have reported radial velocity variation between $V_r = \pm 20$ m/s for the majority of the wave cycle, with an isolated excursion to -100 m/s, such that the radial velocity remained less than 1% of the total velocity throughout the entire cycle [100]. Purely axial (V_z) and azimuthal (V_θ) velocity components are then measured along the tangent line formed by the intersection of the measurement plane and exit annulus centerline, where the local $(x - y)$ and global $(z - \theta)$ coordinate systems coincide. The three view projection of Fig. 4.2 depicts the location of the PIV probe volume and clarifies interpretation of the resulting velocity vectors, where the tangent intersection line is labeled 'Line of Interest' in the 'side' view.

4.3 Results and Discussion

Operability and performance trends observed during a broad, parametric survey of operating conditions encompassing approximately 120 tests in this RDE have been reported by Walters et. al [12], [56]. Counter-rotating waves were observed during most tests, while select lean conditions generated a single wave mode. Thrust measurements revealed that combustor performance was a strong function of the area ratio between the combustor exit and injector throat, while it was weakly sensitive to the operating condition. The current

study focuses on two conditions selected from this survey, case A and B, whose operating parameters are enumerated in Table 4.1. The equivalence ratio (ϕ) was varied between lean and stoichiometric, while the chamber mass flux (G) and air inlet temperature (T_3) were held constant. Case A predominantly had a single, co-rotating wave while case B exhibited a counter-propagating wave mode with one wave propagating in each direction. Table 4.1 also includes wave strength metrics and key integral quantities required for subsequent analysis, along with associated uncertainties. The wave Mach number was approximately 1.15 with respect to the maximum acoustic speed in the combustion products for both test cases. The following sections first examine the detonation propagation dynamics and their instantaneous coupling with the measured flow. The measurements are then phase averaged with respect to the detonation wave location to expose the flow structure. Finally, the phase resolved velocity measurements are used to examine the flow quantitatively by analyzing the performance and global azimuthal momentum balance of the selected cases.

Table 4.1. Operating conditions for test cases, along with key parameters and associated uncertainties used in subsequent analysis.

Case	G $[\frac{kg}{m^2 \cdot s}]$	ϕ	T_3 [K]	p_c [MPa]	$\frac{p}{p_c}$	$\frac{V_{wave}}{V_{CJ}}$	$\dot{m}$ $[\frac{kg}{s}]$	F [kN]
A	350	0.91	570	0.73	1.5	58%	4.38 ± 0.017	5.84 ± 0.078
B	350	1.01	580	0.74	1.8	59%	4.39 ± 0.017	6.14 ± 0.075

4.3.1 Flow Dynamics

The wave frequency and direction for each test is shown in Fig. 4.3 as a function of time, where the broken vertical lines bracket the period of PBL operation for conducting PIV. The global operating mode was determined by first extracting the spatio-temporal history of the chemiluminescence intensity around the circumference of the combustor annulus in a manner similar to Bennewitz et al. [48]. Segments of this spatio-temporal history corresponding to the highlighted segments in Fig. 4.3 are presented as $\theta - t$ diagrams for each test case in Fig. 4.4a.1 and b.1. The mode shown in Fig. 4.3 is then identified by applying a 2D FFT to compute the frequency of the $+\theta$ and $-\theta$ running waves. The first half of case A exhibits a single wave propagating in the $-\theta$ direction, though a counter-propagating wave traveling

9% slower appears during the period of PIV data collection. Two, stable counter-propagating waves are observed during the first 0.24 s of case B, where the $+\theta$ detonation front travels 6% faster than the $-\theta$ wave. The mode change in both cases following shortly after the end of the velocity measurement window likely results from a step change in equivalence ratio as the auxiliary air circuit used to introduce the PIV seed is shutdown.

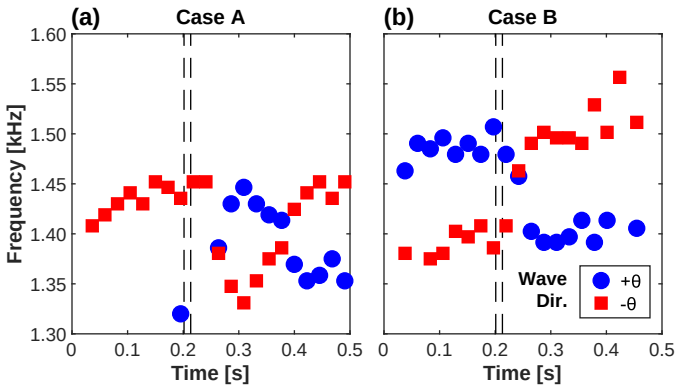

Figure 4.3. Temporal history of wave mode and frequency for case A (a) and B (b). Broken vertical lines indicate the window of velocity measurements.

Figure 4.4 presents the pressure time history at location CC-01 and velocity time history sampled at the intersection of the combustor exit plane and 'Line of Interest' highlighted in Fig. 4.2 during the window of PBL operation for cases A and B. The strong lines with negative slope in Fig. 4.4a.1 show the dominant wave propagating in the $-\theta$ direction for case A, while the counter-rotating mode of case B is apparant in the stable crosshatch pattern of Fig. 4.4b.1. Vibration of the imaging system during case A obscured a sector of the annulus, resulting in the white band centered at $\theta = 90°$ in Fig. 4.4a.1.

Close inspection of Fig. 4.4a.1 reveals a weak counter-propagating wave during t = 0.205-0.210 s, consistent with appearance of a $+\theta$ wave near t = 0.2 s in Fig. 4.3a. Similar behavior has been observed for RDEs operating with natural gas and oxygen-enriched air, where even strong single-wave modes ($p/p_c > 2.5$, $V_{wave}/V_{CJ} > 85\%$) exhibit weak counter-rotating waves [59]. Based on these prior findings and the relative strength of the counter-rotating wave, which only appears for for a short time during the first half of the test and is observed to strengthen and decay during the window of record in Fig. 4.4a, case A is classified as a predominantly single-wave mode. The transient growth and decay of the counter-propagating

wave can be observed in the timeseries presented in Fig. 4.4a.2 and a.3. At the beginning of the window, the single-wave is characterized by periodic, steep-fronted pressure waveforms at CC-01 and similarly steep-fronted V_θ fluctuations in the $-\theta$ direction. As the counter-propagating wave strengthens, the pressure peaks at CC-01 split and the circumferential velocity, V_θ, abruptly switches between the positive and negative θ directions. The counter-rotating wave subsequently decays near t = 0.210 s, and the waveforms of pressure and azimuthal velocity for the remainder of the data window are similar to the beginning of the timeseries. The axial velocity component (V_z) exhibits strong fluctuations throughout the measurement window resulting from broadband turbulence in the RDE exhaust plume.

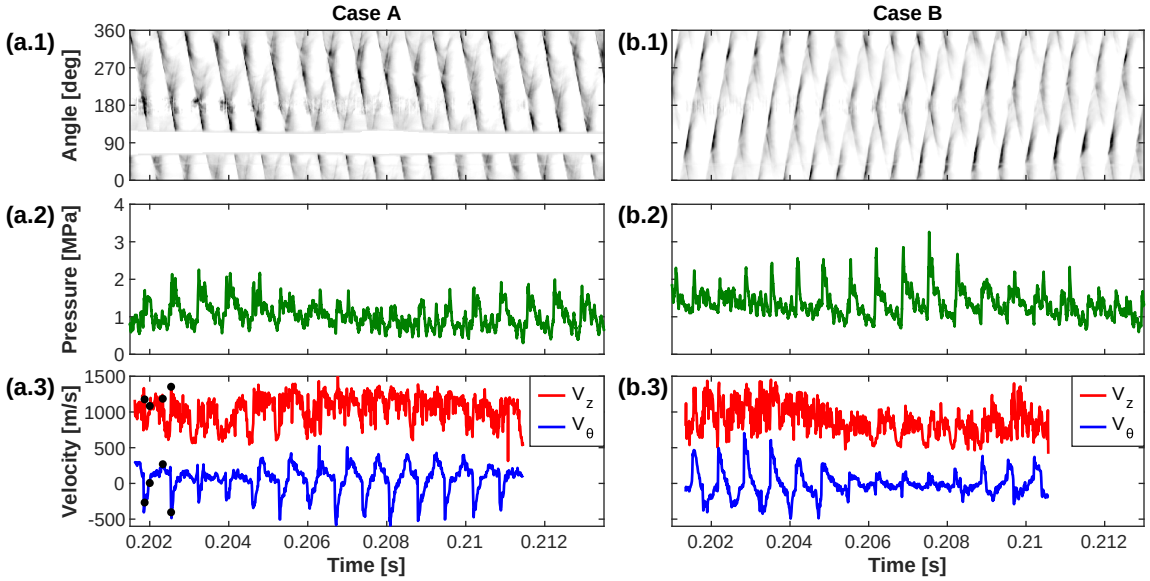

Figure 4.4. Spatio-temporal history of combustor annulus chemiluminescence intensity ((a.1) and (b.1)), time history of pressure at CC-01 ((a.2) and (b.2)), and velocity ((a.3) and (b.3)) for case A and B, respectively.

Unlike the transitional dynamics observed in case A, one wave propagates in each direction around the RDE annulus throughout the test duration for the counter-rotating wave mode of case B. The 6% difference in wave velocity noted in Fig. 4.3b results in the precession of the intersection point between the counter-rotating waves from $\theta = 60°$ and 240° to $\theta = 250°$ and 70° during the observation window. When the wave intersection points, or nodes, are offset from location CC-01 and the PIV FOV at $\theta = 180°$, pressure fluctuations are lower in amplitude and exhibit secondary peaks on the waveform. The azimuthal velocity,

V_θ, alternately turns sharply in the $+\theta$ and $-\theta$ directions as trailing oblique shocks attached to the passing detonation waves divert the flow in the direction of wave propagation. As the wave node aligns with the measurement region, the V_θ velocity fluctuations are damped, while the pressure and V_z measurements exhibit more coherent, periodic fluctuations.

Comparing the V_θ velocity component between cases A and B in Fig. 4.4a.3 and b.3, respectively, supports the classification of case A as a single-wave mode. The unidirectional, steep-fronted azimuthal velocity fluctuations observed during single-wave operation (t $<$ 0.205 s, 0.210 s $<$ t of case A) are not observed at any point during case B, even when the wave intersection node precesses through the PIV FOV. The unidirectional azimuthal velocity jumps then provide a differentiating factor that is a marker of single-wave operation. As a vector quantity, the V_θ velocity measurement is a unique diagnostic compared to the scalar quantities of pressure and chemiluminescence intensity because its sign conveys additional quantitative information. During a typical RDE wave cycle, the sign of V_θ in the exhaust plume is expected to change abruptly as a result of the trailing oblique shock and a second time as the pressure gradient behind the detonation wave reverses the flow direction [81], which is observed during the single-wave portions of Fig. 4.4a.3. Case A can therefore be delineated as exhibiting single-wave operation, providing a discriminating operating mode from case B.

Figure 4.5 shows a typical sequence of PIV vector fields from case A, which correspond with the measurements marked with black dots in Fig. 4.4a.3. The centerline of the PIV FOV, $y = 0$ mm, is aligned with $\theta = 180°$ and labels indicate the orientation of the FOV with respect to the global coordinate system. The background color is scaled relative to the V_θ velocity component, and every other vector is shown for clarity. The sequence of vector fields corresponds with the period of single-wave operation and starts immediately after the trailing oblique shock wave attached to the detonation wave has passed through the FOV in frame (a). The flow has been turned in the $-\theta$ direction, the direction of wave propagation as expected from one-dimensional shock relations. The flow then relaxes so that it is approximately axial in frame (b), before turning in the $+\theta$ direction in frame (c). Figure 4.5d captures the trailing oblique shock wave passing through the FOV, starting a new wave cycle. The white boxes denoting zero azimuthal velocity in the upper third

of frame (d) mark the shock location, separating the flow with a positive circumferential velocity due to relaxation behind the previous wave from the flow turned in the direction of wave propagation.

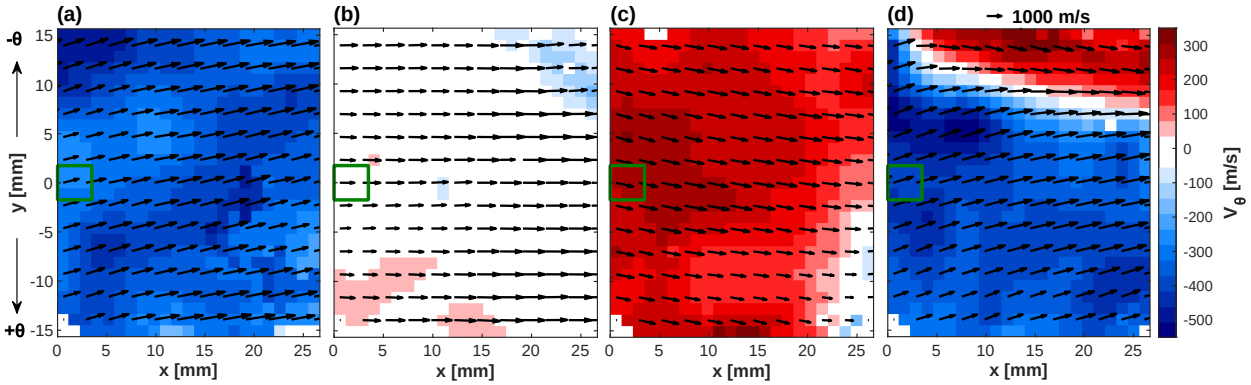

Figure 4.5. Representative vector fields from four points in a wave cycle of case A. Every other vector is shown for clarity.

Bulk flow acceleration moving from the RDE exit plane ($x = 0$ mm) downstream into the exhaust plume is apparent in the vector fields of Fig. 4.5, particularly frame (b). The axial velocity gradient, $\partial V_z/\partial x$, results from the underexpanded combustor exhaust producing a pressure gradient that accelerates the flow. On average, the axial velocity increases by 330 m/s in the PIV FOV for case A and 250 m/s for case B. No trend in the axial gradient of axial velocity was observed with respect to the wave cycle. While velocity vectors were computed for the entire field of view as shown in the frame sequence, subsequent analysis will focus on a single velocity time history, computed as the average of the velocity vectors highlighted by the green boxes in Fig. 4.5. A point along the combustor centerline where the laser sheet was tangent to the exhaust annulus was selected so that the PIV and combustor coordinate systems coincide, as discussed in section 4.2.2.

From the raw time histories of Fig. 4.4, it is clear that the frequency and coherence of pressure and velocity shift over the duration of the data window. The continuous wavelet transform (CWT) is applied to investigate the physical mechanisms for the variation by comparing the coherence of the multiple, simultaneously acquired signals in time-frequency space. A CWT based on the analytic Morse wavelet provides a time-frequency decomposition of each signal [101], shown in the wavelet scalograms of Fig. 4.6a.1-a3 for case A and

Fig. 4.6b.1-b.3 for case B. The shaded regions bounded by broken white lines denote the "cone of influence," indicating regions influenced by CWT edge-effects. For case A, the pressure at CC-01 (Fig. 4.6a.1) exhibits strong content near the fundamental frequency of 1.43 kHz during the periods of single-wave operation. During the window of counter-rotating wave action ($0.205 < t < 0.21$), the dominant frequency of pressure oscillations doubles and becomes weaker as each wave separately passes the transducer and their interactions reduce the pressure amplitude. The axial velocity component (Fig. 4.6a.2) exhibits similar trends as the pressure at CC-01, where periods of single-wave operation feature stronger content at the fundamental frequency, while twice this frequency is excited when the counter-rotating wave strengthens. The time-frequency resolution of the CWT clarifies the coupling between axial velocity and pressure, as the high levels of turbulence affecting the axial velocity measurement obscured this relationship in the raw timeseries of Fig. 4.4a. While prior simulations of steady RDE operation have shown coupling between pressure and axial velocity, the current, high-fidelity measurements demonstrate that this coupling remains even for off-nominal modes of RDE operation. Finally, the circumferential velocity (Fig. 4.6a.3) has frequency content at the wave circumscription period throughout the timeseries. However, the scalogram shows that azimuthal velocity fluctuations are strongest during the period of counter-propagating wave motion, in contrast to the pressure and axial velocity. This results from the counter-propagating waves increasing the amplitude of circumferential velocity fluctuations, rather than doubling their frequency, as each wave deflects V_θ in its corresponding direction of propagation.

A similar relationship between flow quantities is observed for case B (Fig. 4.6b.1-b.3), where the pressure and axial velocity simultaneously have strong fluctuations at the fundamental frequency of 1.5 kHz, while the strongest circumferential velocity fluctuations are temporally offset. In this test, the changes in frequency content and oscillation strength result from the node precession noted in Fig. 4.4b.1. Coherent frequency content in the pressure and axial velocity signals occurs when the wave intersection point is aligned with CC-01 and the PIV FOV between $t = 0.205$-0.209 s. Conversely, when the node is offset from the measurement location, the passage of each counter-rotating wave results in weaker pressure and axial velocity oscillations, at twice the fundamental frequency. At the same

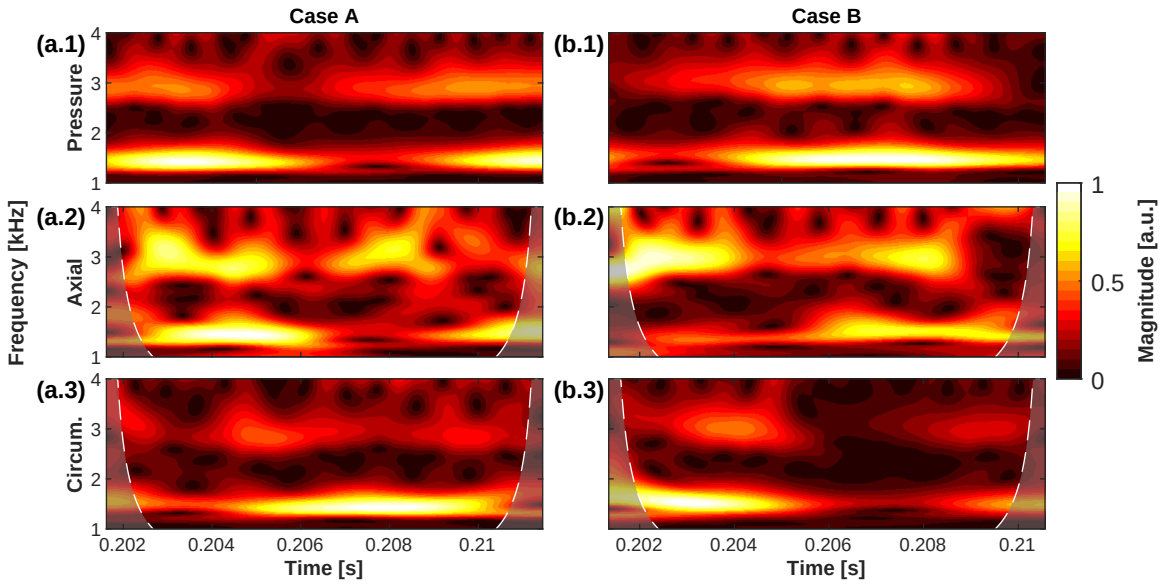

Figure 4.6. Wavelet scalogram of pressure at CC-01 ((a.1) and (b.1)), axial velocity ((a.2) and (b.2)), and circumferential velocity ((a.3) and (b.3)) for case A and B, respectively.

time, the azimuthal velocity fluctuations at 1.5 kHz become strong for the same reason as noted in Fig. 4.6a.3, where the counter-rotating waves pull the flow in opposing directions, increasing the oscillation amplitude. The time history of Fig. 4.4b.3 shows that V_θ is approximately zero with minimal coherent fluctuations when the node is aligned with PIV FOV. The scalogram in Fig. 4.6b.3 corroborates this, with minimal frequency content shown during t = 0.205-0.209 s. This is in contrast to case A, where azimuthal velocity fluctuations at the wave circumscription frequency persist throughout the timeseries in Fig. 4.6a.3 due to the trailing oblique shock attached to the single detonation wave producing jumps in azimuthal velocity in the $-\theta$ direction.

Timeseries analysis of the RDE chamber pressure and exhaust plume velocity informed by annulus imaging revealed a complex, non-stationary flowfield convolved with wave interactions and highly turbulent processes. While wavelet analysis helped clarify relationships between the amplitude and frequency of fluctuations in the measured variables, phase averaging will elucidate the structure of the RDE flowfield for the two studied cases.

4.3.2 Phase Averaged Flowfield

The circumferential structure of the detonation wave and combustor exit plane flow are reconstructed for each case by phase averaging the pressure, velocity, and annulus chemiluminescence measurements presented in Fig. 4.4. Experimental RDE investigations typically observe some degree of wave unsteadiness, resulting in inter- or intra-lap variations in the wave velocity [18], [20], [48]. Phase averaging based on a mean cycle frequency will then tend to smear the wave front due to the stochastic variations in its arrival at a given probe volume. Therefore, the presented flowfields are phase averaged using the instantaneous wave front location determined from the high-speed chemiluminescence imaging of the RDE annulus. Timing signals from the chemiluminescence and PIV cameras are acquired simultaneously with the high frequency pressure to synchronize the measurements. The identified wave location is then interpolated from the chemiluminescence imaging rate to the PIV and pressure transducer sampling frequencies.

A wave tracking algorithm capable of capturing intra-cycle wave speed variations was developed to identify the pointwise leading edge of the detonation front within the annulus. The annular profile of chemiluminescence intensity at each time is filtered and differentiated using FFT methods that leverage the exact periodicity inherent to the annular geometry. Wave fronts are identified as peaks in the derivative of the annular profile, where additional checks are performed to ensure that the front lies near the maximum chemiluminescence intensity and that the wave advances monotonically. For the counter-rotating waves in case B, the wave tracks are split into $+\theta$ and $-\theta$ components using a 2D FFT prior to applying the wave tracking routine. Figure 4.7a and b present the identified wave fronts overlaid on the spatio-temporal chemiluminescence history for the same period as in Fig. 4.4. Red lines track the $-\theta$ wave in both cases, while blue lines correspond to the $+\theta$ wave in case B. It is clear that the program has accurately identified the wave front at each instant in time, despite the obscured annulus sector in case A and low intensity of the $-\theta$ wave in case B.

The algorithm provides θ_+ and θ_- as outputs, respectively the angular position of the $+\theta$ and $-\theta$ running waves as a function of time. In case A, the position of the single $-\theta$ wave is read as θ_- and directly used to generate the subsequent phase averages. While the mean

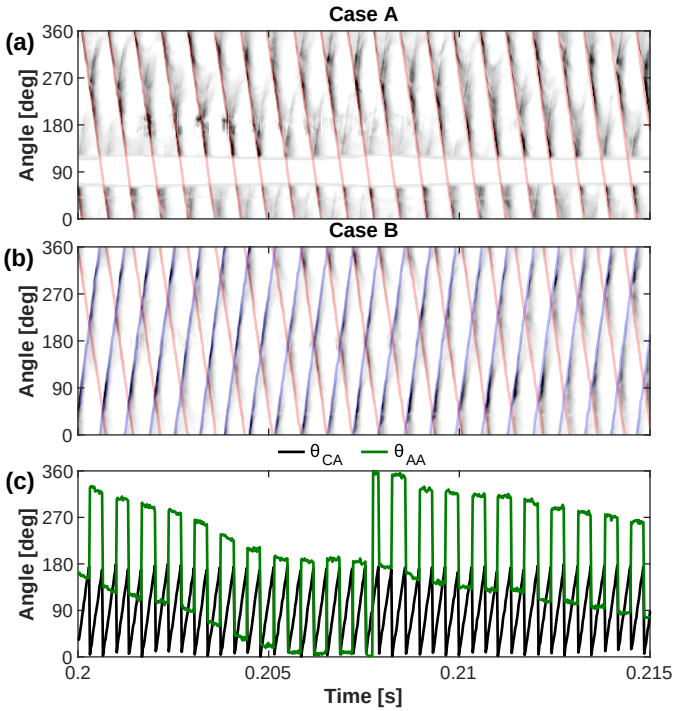

Figure 4.7. Location of instantaneous wave front for case A (a) and B (b), and resulting annulus angle and cycle angle phase signals for case B (c).

flowfield of case A is self-similar such that it can be considered steady in the wave frame of reference, the counter-rotating waves of case B produce a non-stationary flowfield that continuously evolves throughout the wave cycle. A doubly phase resolved flow reconstruction procedure is then adopted to recreate each variable around the annulus circumference and at each phase of the wave intersection cycle. This is possible due to the precession of the wave nodes observed in Fig. 4.4b.1, as each point-measurement probe collects data at each combination of wave location and separation over several wave cycles. The wave locations are thus converted into a cycle angle, θ_{CA}, that varies with the separation between the two counter-rotating waves, and an annulus angle, θ_{AA}, which represents the location of the two waves with respect to the point-probe volume. The parameters are computed as

$$\theta_{CA} = \frac{1}{2}\mathrm{mod}\left(\theta_+ - \theta_-,\ 360\right) \tag{4.1}$$

$$\theta_{AA} = \mathrm{mod}\left(180 - \theta_+ + \theta_{CA},\ 360\right), \tag{4.2}$$

and plotted in Fig. 4.7c. The two phase angles are finally used to reconstruct the flowfield for case B.

Table 4.2. Phase averaging intervals for each test case and flowfield parameter.

Case	Chemiluminescence	Pressure	Velocity
A	0.014-0.252 s	0.014-0.252 s	0.202-0.205 s, 0.210-0.212 s
B	0.015-0.235 s	0.015-0.235 s	0.201-0.211 s

While the velocity measurements were restricted to the 10 ms period of PBL operation, pressure and chemiluminescence were collected for the entirety of the test. These measurements were then averaged over the longer periods documented in Table 4.2. Note that in both cases, the windows exclude the mode transitions observed after the PIV data window in Fig. 4.3. The window of velocity measurements is also noted, including the period excluded from the phase average for case A due to the temporary appearance of a counter-propagating wave. This left six wave cycles to compute the phase averaged velocity for case A.

The phase averaged flowfield for case A is presented in Fig. 4.8 as the profile of each variable around the circumference of the RDE annulus when the wave front is aligned with $\theta = 180°$. Shaded regions surrounding the axial and circumferential velocity profiles represent a 95% confidence interval of the phase average, including the contribution from the statistical correlation uncertainty discussed in Section 4.2.2. The steep-fronted rise in pressure at the chamber head end marks the wave front, which coincides with the peak chemiluminescence intensity. Pressure profiles from CC-01 and CC-02 are shown, where the profile of CC-02 has been shifted to account for its offset circumferential position. Both transducers show a similar phase averaged profile, indicating that the detonation wave remains stable as it circumscribes the chamber annulus. The peak-to-valley pressure fluctuation amplitude is 1.04 MPa for both averaged waveforms, in agreement with the p/p_c in Table 4.1 computed

using a peak finding algorithm [12]. The trailing oblique shock attached to the detonation front impinges on the downstream CC-03 transducer after a short time delay determined by the shock angle, producing the lagged pressure profile observed in Fig. 4.8a. The magnitude of downstream pressure fluctuations at transducer CC-03 is similar to those at the chamber head end; this is likely due to the relatively low combustor diameter to length ratio. As shown in Fig. 4.8c and previously noted in Fig. 4.5d, the oblique shock extends into the combustor exhaust, turns the azimuthal velocity in the $-\theta$ direction, and increases the axial velocity, consistent with the canonical RDE flowfield [81].

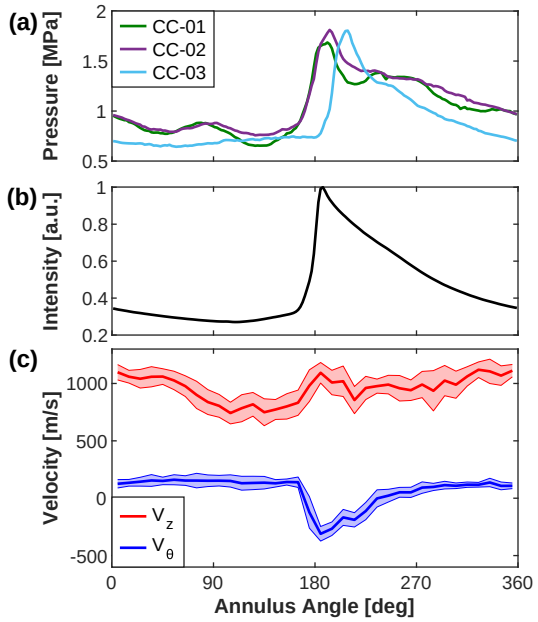

Figure 4.8. Phase-averaged (a) pressure (b) chemiluminescence intensity and (c) velocity for case A.

Behind the wave front at $\theta = 180°$, the pressure, chemiluminescence intensity, and circumferential velocity all relax to the conditions ahead of the detonation. The relaxation in pressure at the aft end of the combustor (CC-03) and exit plane azimuthal velocity occur over a similar circumferential distance, as the pressure gradient behind the detonation wave induces the flow turning. The relaxation in the chemiluminescence profile of Fig. 4.8b occurs over half the circumference of the RDE annulus, indicating that the wave and its associated heat release is spatially protracted. The spatial extent of the wave may indicate

that combustion is not completed within the detonation front and continues behind the wave as a deflagration. This hypothesis is consistent with an observed wave speed for case A that is 58% of the Chapman-Jouguet detonation velocity. In comparison, RDE experiments conducted with readily detonable reactants have observed that more compact waves correlate with higher wave speeds [16]. It appears that one or multiple auxiliary loss mechanisms prevent all of the reactants from being consumed in the detonation front, reducing the energy release available to support propagation. Recent research has provided experimental evidence for the important role of product gas recirculation and deflagrative burning in altering the mixture ahead of the detonation wave from the ideal manifold conditions and thereby depressing the detonation wave speed [90], a mechanism originally hypothesized by Edwards [79]. Additional mechanisms that plausibly contribute to the observed deficit include incomplete mixing and heat loss to the combustor walls [7], [62].

The wave chemiluminescence, pressure, and velocity for case B shown in Fig. 4.9 were reconstructed using the two phase components shown in Fig. 4.7c. The broken blue and red lines indicate the location of $+\theta$ and $-\theta$ propagating waves, respectively. Note that the reconstruction has exploited the symmetry between the wave locations, where the first and third, and second and fourth quadrants are identical. Horizontal lines in the reconstruction then reproduce a measurement of each variable around the entire annulus circumference at an instant in time corresponding to a given cycle phase. The Fig. 4.9d color scale white point is set to the mean axial velocity. The extended data window noted in Table 4.2 permitted phase averaging the annulus chemiluminescence and pressure, whereas the velocity measurements were reconstructed based on the instantaneous wave locations because data collection was limited by the 10 ms PBL pulse train. While the average azimuthal wave structure is more evident in the phase averaged chemiluminescence intensity, patterns with respect to the wave cycle are apparent in all four measurements. The reconstruction follows a complete wave cycle, with both waves starting immediately after an intersection at $\theta = 0°$ and intersecting again at $\theta = 180°$ at a cycle angle of $\boldsymbol{\pi}$, before returning to the starting location at $\theta = 0°$, where the cycle repeats.

The high chemiluminescence intensity and pressure fluctuation amplitude along the broken blue line contrasted with the low amplitude along the red line of Fig. 4.9a and b cor-

roborates the prior observation that the $+\theta$ propagating wave of case B is stronger than the counter-propagating wave. While the $+\theta$ wave persists through the entire cycle, the $-\theta$ wave appears to decay prior to the subsequent intersection event. The different wave strengths, which are observed to persist for hundreds of cycles, could be sustained through a self-reinforcing process coupled to injection dynamics. Consider a region near $\theta = 90°$, offset from the wave intersection point. The high pressure behind the stronger, $+\theta$-propagating detonation near a cycle phase of $\pi/2$ prolongs injector recovery, leaving less reactant for the $-\theta$ wave which will propagate through the same region at a cycle phase of $3\pi/2$. With reduced reactants to support propagation, the $-\theta$ wave releases less energy and produces a lower pressure rise. This results in a shorter injector recovery time, generating a better-prepared mixture for $+\theta$ wave. The alternating cycle between weak and strong waves appears stable so long as the weaker wave doesn't fully decay. Bleumner et al. have alternately suggested that the weak, counter-rotating wave is simply an inert shock, as reviewed in Section 4.1 [80]. Figure 4.9a and b show that the highest pressures and chemiluminescence intensities are found near the wave intersection points, where the measured pressure reaches 2.6 MPa. Combustion at wave nodes proceeds at pressures higher than normal wave propagation due to shock interactions, which could energize both waves for the ensuing cycle. The weaker $-\theta$ wave is then able to continue propagating until the next collision rather than decaying and leaving a single wave.

Figure 4.9c shows that the $+\theta$ wave produces the highest circumferential velocity midway through a wave intersection cycle near a phase angle of $\pi/2$. Conversely, the minimum azimuthal velocity behind the $-\theta$ wave occurs near a cycle angle of π, before the subsequent wave intersection. The azimuthal velocity relaxation occurs faster behind the $+\theta$ wave than the $-\theta$ wave, resulting in a negative V_θ prior to the subsequent $-\theta$ propagating wave. Behind the $-\theta$ wave, the azimuthal velocity remains negative until the next $+\theta$ wave arrives. The higher pressure gradient behind the $+\theta$ wave produces greater flow turning opposite the direction of wave propagation, resulting in the observed difference in circumferential velocity relaxation. At the wave intersection, V_θ drops to zero as the interacting trailing oblique shocks destructively interfere and produce zero flow turning. This explains the period of near-zero azimuthal velocity observed in Fig. 4.4b.3 when the intersection node is aligned

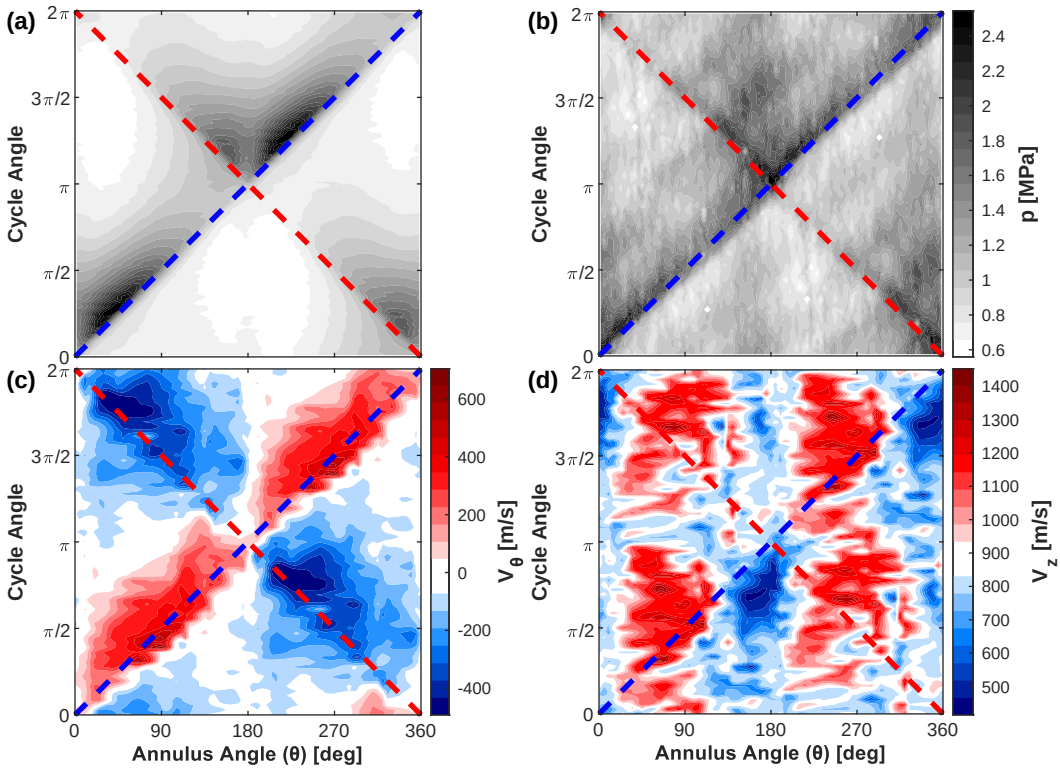

Figure 4.9. Phase-averaged (a) annulus chemiluminescence, (b) pressure, (c) circumferential velocity, and (d) axial velocity around the annulus circumference over the course of a full wave-intersection cycle for Case B.

with $\theta = 180°$ between t = 0.205-0.209 s. During this period, the trailing oblique shocks from the passing waves cancel instead of alternately turning the flow in the $+\theta$ and $-\theta$ directions.

The pattern of wave strengthening and decay observed in the chemiluminescence, pressure, and azimuthal velocity measurements is not present in the phase resolved axial velocity component of Fig. 4.9d. Instead, the profile of V_z around the combustor annulus is almost independent of cycle phase angle, with bands of low velocity aligned with the wave nodes at $\theta = 0°$ and 180° separated by regions of high axial velocity. These regions of high axial velocity are centered near the annulus angle where the strongest azimuthal velocity fluctuations occur.

The transonic exhaust flow producing oblique shocks and associated high azimuthal velocity fluctuations observed in both test cases is likely to challenge system integration efforts with downstream components, particularly turbines [9]. Even for the comparatively simple

scenario of case A, the flow switches swirl direction twice within each wave cycle. Calculating the pointwise flow angle using the velocity profiles of Figs. 4.8 and 4.9 shows variation of $\pm 15°$ and $\pm 30°$ for cases A and B, respectively. This experimental characterization of the downstream boundary condition presented by an operating RDE to an interfacing component illustrates the challenges associated with integrating an RDE into a gas turbine system. Downstream components will also have to accommodate the dramatic variations in flowfield resulting from different wave modes, as shown by the juxtaposition between Fig. 4.8 and Fig. 4.9. One possible solution presented by Stout and Baratta [64] attenuates the unsteadiness via a carefully contoured flowpath between the combustor and downstream components, but it unclear whether the thermodynamic benefit of an RDE can be maintained when the flow has been homogenized [16]. A complete evaluation of any configuration requires careful characterization of the exhaust stream work output potential.

4.3.3 Quantitative Flowfield Evaluation

Experimental quantification of RDE performance has proved challenging due to the unsteady, high-enthalpy flows inherent to the cycle. While directional sensitivities may be captured by direct thrust measurements, this metric provides no indication of whether a pressure gain has been achieved. Furthermore, thrust is not a relevant performance metric for combustion systems where work extraction is the primary objective. Consistent methods of RDE performance analysis must compute the exhaust flow work availability and draw comparison to the system driving potential, typically the reactant manifold pressure, to determine whether a pressure gain has been achieved [56]. A new method of quantifying this work potential in an RDE that employs the phase-resolved velocity measurements extracted in Section 4.3.2 is formulated and applied. While pressure gain combustors produce an unsteady blowdown process wherein work is extracted from a range of total pressures and temperatures [13], [14], a single representative metric of combustor performance is typically sought for ease of interpretation and comparison to existing (constant pressure) devices. One such approach is the Equivalent Available Pressure (EAP) methodology [61], which computes the equivalent, steady total pressure available to produce thrust using either the full flow and

thermodynamic state information available to simulations or experimental measurement of gross thrust. The EAP can then be compared to the reactant manifold pressure to determine whether the combustor produces a pressure gain. The EAP is computed from experimental measurements by rearranging the thrust equation for the exit plane pressure and then correcting to stagnation conditions using isentropic relations, giving

$$EAP = \frac{\frac{F}{A_e} + p_\infty}{\gamma + 1} \left(\frac{\gamma + 1}{2} \right)^{\frac{\gamma}{\gamma - 1}}, \tag{4.3}$$

where F is the gross thrust, A_e is the annulus exit area, p_∞ is the ambient pressure, and γ is the reaction product specific heat ratio. Equation (4.3) relies on an assumption of unity Mach number at the combustor exit plane, which conservatively produces the minimum pressure consistent with the measured thrust. However, this assumption and the associated performance decrement of up to 10% observed in prior numerical studies [61] may prove overly prohibitive to experimental demonstration of a pressure gain.

A new scheme for evaluating RDE performance that leverages the current high-speed velocity measurements is derived for comparison with the EAP method and in-situ validation of its assumed exit Mach number. As with the EAP, the range of total temperatures and pressures driving the RDE exhaust is encapsulated in a single, steady thermodynamic stagnation state representative of the work that can be extracted from the combustor and consistent with the measurements. The analysis starts from the integral form of the conservation equations for mass and momentum, whose global balance is closed by measurement of the flowrate of reactants entering the combustor and the thrust of exiting combustion products, respectively. The conservation of mass and momentum at the outlet of an RDE where the outlet flow is assumed uniform across the width of the annulus but varies temporally and circumferentially, as in case B, can be written as

$$\dot{m} = \frac{A_e f_{cc}}{2\pi} \int_0^{\frac{1}{f_{cc}}} \int_0^{2\pi} \rho_e V_z \partial\theta \partial t, \tag{4.4}$$

$$F = \frac{A_e f_{cc}}{2\pi} \int_0^{\frac{1}{f_{cc}}} \int_0^{2\pi} \left(\rho_e V_z^2 + p_e - p_\infty\right) \partial\theta \partial t, \tag{4.5}$$

where f_{cc} is the limit cycle frequency and p_e, ρ_e are respectively the pressure and density at the RDE exit. Integration averages the mass and momentum flux of exhausting combustion products over the wave period and the annulus circumference. Given that only V_θ and V_z have been measured, isentropic relations and a calorically perfect gas equation of state are used to relate the theoretical, equivalent steady upstream state, p_0, T_0, to the RDE exit plane properties. It should be noted that chamber pressure measurements are not considered quantitative, as discussed in Section 4.2.2, and therefore not used in the following analysis. Rearranging Eq. (4.4) and (4.5) results in relations that can be solved for the total pressure and total temperature,

$$p_0 = \frac{R_u T_0 \dot{m}}{A_e MW} \left(\int_0^1 \int_0^1 V_z \left(\frac{T_e}{T_0}\right)^{\frac{1}{\gamma-1}} \partial\vartheta \partial\tau \right)^{-1}, \tag{4.6}$$

$$F = p_0 A_e \int_0^1 \int_0^1 \left(\frac{MW}{R_u T_0} \left(\frac{T_e}{T_0}\right)^{\frac{1}{\gamma-1}} V_z^2 + \left(\frac{T_e}{T_0}\right)^{\frac{\gamma}{\gamma-1}} \right) \partial\vartheta \partial\tau - p_\infty A_e, \tag{4.7}$$

where the ratio of static to stagnation temperature,

$$\frac{T_e}{T_0} = 1 - \frac{MW \cdot (\gamma - 1)}{\gamma R_u T_0} \cdot \frac{V_z^2 + V_\theta^2}{2}, \tag{4.8}$$

has been used to simplify notation. In Eq. (4.6-4.8), the product gas properties of molecular weight, MW, and the ratio of specific heats, γ, can be computed using NASA CEA [73]. For this application, the combustion product properties are estimated by averaging values computed using equilibrium thermochemistry for a CJ detonation and a constant pressure combustor, which approximately bounds the range of possible values. Furthermore, both

parameters are insensitive to the heat addition process for the reactant mixtures considered here. Averages over the wave period and circumference have been normalized so that the integration limits are (0, 1) and the θ and t differentials have been replaced with ϑ and τ, respectively. The phase resolved RDE exit plane flowfield for each case developed in Section 4.3.2 is used as the input V_z and V_θ profiles. The total temperature is then determined by numerically solving the implicit expression that results from substituting Eq. (4.6) into Eq. (4.7), which subsequently permits recovery of the total pressure using Eq. (4.6).

An uncertainty analysis is conducted for all computed performance parameters to account for contributions from the measured velocity, mass flowrate, and thrust in addition to the estimated exhaust gas properties. The uncertainty of a dependent variable is computed as

$$u_y = \sqrt{\sum_{\mathrm{i}} \left(u_{x_\mathrm{i}} \frac{\partial y}{\partial x_\mathrm{i}} \right)^2}, \tag{4.9}$$

where x_i are the independent variables and u_{x_i} is the corresponding uncertainty [70]. Partial derivatives are evaluated numerically using a central difference scheme to propagate uncertainties through all steps of calculating each parameter, including the numerical solution of Eq. (4.7) for total temperature. Uncertainty in the mass flowrate of reactants and thrust measurements are reported in Table 4.1. Velocity uncertainty for case A uses the bounds shown in Fig. 4.8c, while case B uses the average statistical correlation uncertainty. The uncertainty in product gas properties, MW and γ, is estimated as half the difference between the CJ detonation and constant pressure combustion bounding values used to compute each parameter. Finally, the uncertainty in nozzle throat area is computed using measured part dimensions and an assumed deviation of twice the specified manufacturing tolerance to account for possible degradation during operation.

Results of the performance calculations and associated uncertainties for cases A and B are summarized in Table 4.3. The total pressure produced by the combustor computed using the EAP method (Eq. (4.3)) or the PIV measurements (Eq. (4.6)) is between 35-40% of the air manifold pressure, p_3, measured at transducer port PT-OM of Fig. 4.2. The 60-65% pressure loss is comparable to other recent works, which have focused on readily detonable hydrogen-air reactants [96], [97]. Operation with high-performance combustor

designs remains challenging, particularly with the less-detonable natural gas-air reactants used in this study. The total pressure loss is principally a result of a high-loss injector configuration. Prior work has shown that RDE performance is more sensitive to the area ratio between the combustor exit and reactant inlet than any other parameter [56], where this area ratio is 4.86 for the current injector. This effectively limits the maximum possible combustor performance to a pressure loss of 55-60%, based on an idealized thermodynamic performance model [56]. This also explains the 6% difference in total pressure between cases A and B, despite their significantly different flowfields. The high-loss injector design controls the performance, such that differences in the operating mode can only have a marginal effect. Comparing the two performance metrics shows that the method of Eq. (4.6) computes a total pressure 6% higher than the EAP for case A and 8% higher for case B. The EAP method assumes that the exhaust products are choked at the combustor exit, resulting in a lower total pressure. Incorporating the velocity measurements relaxes this assumption and accounts for a spatio-temporally varying exit Mach number. The EAP then underpredicts the total pressure of the RDE exhaust by 5-10%, consistent with the previously mentioned decrement observed in simulations [61].

The proposed performance analysis method based on PIV measurements made use of two conservation equations whose global balance was closed with integral measurements. Therefore, two independent state variables can be computed which together specify the full state of the hypothetical, steady condition representative of the work that could be extracted from the RDE. As mentioned previously, a total temperature is computed using Eq. (4.7) in addition to the total pressure computed with Eq. (4.6). Prior analysis by Paxson and Kaemming [13] has shown that while PGC cycles extract work from a range of stagnation conditions in an unsteady blowdown process, the mass-averaged total temperature must equal the adiabatic flame temperature for constant pressure combustion. The path of heat addition during combustion does not alter the energy liberated from reactant chemical bonds, only the associated entropy increase. That is, while the heat addition process is unable to affect the energy contained within the flow, it can influence its availability, typically measured by total pressure. The total temperature is then reported relative to the adiabatic flame temperature, T_{ad}, for each condition in Table 4.3. This compares the experimentally determined

mass averaged total temperature to its theoretical counterpart, and can be interpreted as a combustion efficiency. Case B then achieves a combustion efficiency 4% higher than case A, in line with the 6% difference in total pressure.

Table 4.3. Combustor performance for each case. Pressures in MPa, and uncertainty bounds are given using 95% confidence intervals.

Case	p_3	EAP	p_0	T_0/T_{ad}	$p_0\|_{T_0=T_{ad}}$	Swirl
A	2.33	0.81 ±0.012	0.86 ±0.013	0.82 ±0.027	0.91 ±0.013	0.072 ±0.009
B	2.34	0.84 ±0.012	0.91 ±0.011	0.85 ±0.023	0.96 ±0.011	-0.028 ±0.001

The total pressure was also evaluated assuming complete combustion by using the adiabatic flame temperature as the total temperature ($T_0 = T_{ad}$) in Eq. (4.6), in lieu of computing it using Eq. (4.7). This approach simplifies the analysis and eliminates the need for a thrust measurement, but could overestimate the delivered total pressure if the combustion is incomplete. The result is reported as $p_0|_{T_0=T_{ad}}$ in Table 4.3, which demonstrates that assuming complete combustion produces the expected result of increasing the total pressure. Relative to the approach that accounts for the combustion efficiency, the simplification increases the total pressure by 5% for both cases. The performance estimate based on the combined closure of mass and momentum conservation is more conservative than this approach, which only uses the conservation of mass. While the local flow measurements permit reduction in the assumptions made in the analysis of RDE performance and consequently improve its accuracy, they must be anchored by the globally integrated quantities.

Uncertainty bounds for the performance parameters in Table 4.3 are reported using 95% confidence intervals. The absolute uncertainty in stagnation pressure is similar whether computed using the EAP method or Eq. (4.6), resulting in a lower relative uncertainty using the latter method as it predicts a higher total pressure for both cases. This also suggests that any errors in the velocity measurements do not dominate the resultant uncertainty for the proposed method. Indeed, detailed accounting indicated that the uncertainty of total pressure, temperature, and EAP were all dominated by uncertainty in the RDE exit area and measured thrust. Sensitivity analysis further demonstrated that the total pressure is inde-

pendent of the mixture molecular weight, which is not obvious due to the nonlinear, implicit interdependence between Eq. (4.6) and Eq. (4.7). The uncertainty in RDE performance could then be further reduced by reducing the uncertainty of thrust measurements.

The stagnation state conditions are used in conjunction with isentropic relations to further interrogate the RDE exhaust flow and evaluate the axial Mach number at its downstream boundary condition as

$$M_z = \frac{V_z}{\sqrt{\frac{\gamma R_u T_0}{MW} \cdot \frac{T_e}{T_0}}}, \tag{4.10}$$

where T_e/T_0 is given by Eq. (4.8). The distribution of axial Mach number is shown in the histograms of Fig. 4.10a. The samples are computed from the timeseries of PIV measurements during the windows used for phase averaging listed in Table 4.2. As has been observed in simulations [61], [81], the axial Mach number is not precisely unity and instead spans the transonic regime. The significant variation in exit Mach number confirms its role in reducing the EAP relative to the computed total pressure presented in Table 4.3. While the EAP method makes the conservative assumption of unity exit Mach number, the method of Eq. (4.6) accounts for the observed variation.

One approach to addressing the limitations of the Equivalent Available Pressure method accounts for an estimated or experimentally determined Mach number at the RDE exit plane [102]. The Mach-corrected EAP can then be computed as

$$EAP_M = \left(\frac{F}{A_e} + p_\infty\right) \frac{\left(1 + \frac{\gamma-1}{2} M_z^2\right)^{\frac{\gamma}{\gamma-1}}}{1 + \gamma M_z^2}. \tag{4.11}$$

Figure 4.10b plots this relationship between the axial Mach number and the corrected EAP using the thrust and estimated ratio of specific heats for each of the two test cases. The curves with minima located at $M_z = 1$ confirms that the assumption of unity exit Mach number selects the minimum total pressure consistent with the measured thrust. Figure 4.10b also shows that the variation in axial Mach number of ± 0.5 observed in Fig. 4.10a can increase the corrected EAP by 10% relative to its uncorrected counterpart. While the Mach-corrected EAP has previously been evaluated using a single estimate of the exit Mach number

[102], here we use the axial Mach number samples used to compute the distribution of M_z to determine a corresponding distribution of corrected EAP, shown in Fig. 4.10c. The distribution of Mach-corrected EAP is skewed towards lower values because the axial Mach number distribution for both cases is centered near the minimum of Eq. (4.11). While the peak for both cases lies in the minimum bin, both also have tails that extend beyond the total pressure computed using Eq. (4.6). Using the computed distribution, a maximum corrected EAP of 0.95 MPa encompasses 90% of the samples in each case, which is 5-10% higher than the total pressure in Table 4.3 computed using Eq. (4.6). This approach addresses a principal limitation of the EAP method, but it is unclear how to most appropriately average the range of corrected Equivalent Available Pressures to produce a single estimate of the total pressure. As discussed previously, determining a single, representative total pressure is a critical requirement for any method of quantifying RDE performance, so that it can be compared with the manifold pressure to assess the net pressure gain. By explicitly invoking conservation equations for mass and momentum in integral form, averaging across the range of measured flow states is directly incorporated into the proposed method of Eq. (4.6). This results in a method that makes more appropriate use of the velocimetry measurements and removes this ambiguity from the RDE performance assessment.

The distribution of M_z in Fig. 4.10a peaks near unity for case B, while it is centered at higher Mach numbers for case A. The regions of low axial velocity observed in Fig. 4.9d for case B shift the corresponding distribution towards unity. In comparison, the axial velocity component of case A during single-wave periods in Fig. 4.4a.3 shows elevated velocities that would contribute to higher exit plane Mach numbers. The limitations of this analysis should be noted, where the exit plane static temperature and sonic velocity have been computed using the total temperature and local flow velocity. As noted previously, the exhaust from an RDE does not issue from a single thermodynamic stagnation state, but instead from a range of total temperatures and pressures in a continuous blowdown process. While the assumption of a single stagnation state may bias the distributions shown in Fig. 4.10a from their true values, it is apparent that a geometric throat at an RDE outlet does not constrain M_z to unity, as is expected in a constant pressure combustor. Similar to the wide variation

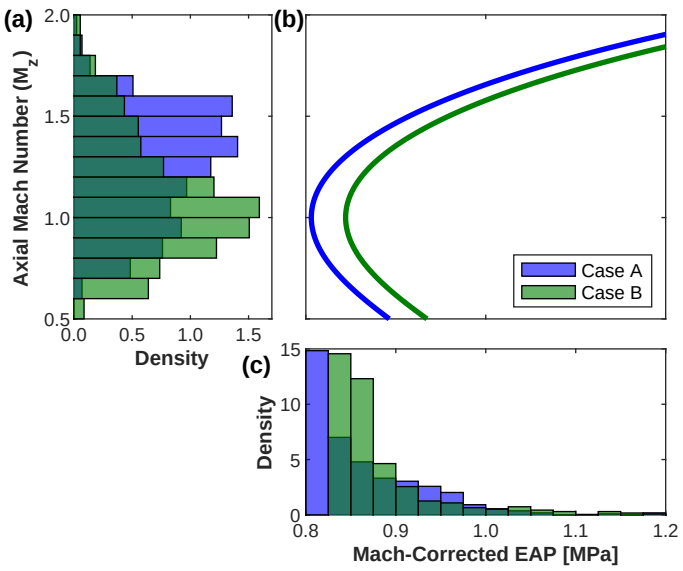

Figure 4.10. Distribution of instantaneous axial Mach numbers (a), relationship between axial Mach number and Mach-corrected EAP for both cases (b), and distribution of resulting Mach-corrected EAP.

in flow angles noted in Section 4.3.2, turbines and expansion nozzles must be able to accept and efficiently expand the transonic exhaust issuing from an RDE [9], [71].

The exit plane PIV measurements can further be applied to quantify the azimuthal momentum balance at the RDE downstream boundary condition and hence assess the claim that no net swirl is produced in an RDE combustor [14]. The instantaneous partitioning of kinetic energy between the axial and azimuthal velocity components is first considered. As shown in Fig. 4.11, the majority of the exhaust flow has low azimuthal kinetic energy. However, the distributions for both cases have significant tails, where the azimuthal kinetic energy is at least 5% of the axial kinetic energy for 20% of the samples. The heavy tails are a result of the strong, but spatially localized, fluctuations in the azimuthal velocity immediately behind the oblique shock waves that extend into the RDE exhaust.

Finally, the azimuthal momentum balance is evaluated by computing the swirl number, the ratio between the axial fluxes of azimuthal and axial momentum [103]. By assuming

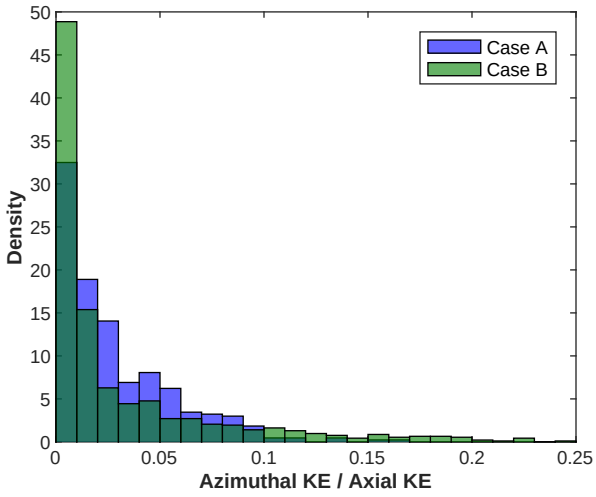

Figure 4.11. Distribution of instantaneous azimuthal kinetic energy as a fraction of the axial kinetic energy.

that the outlet flow is uniform across the annulus width, the equation for the swirl number can be rewritten as

$$S = \frac{\int_0^R \rho V_z V_\theta r^2 \partial r}{R \int_0^R \rho V_z^2 r \partial r} = \frac{\int_0^1 \int_0^1 \rho_e V_z V_\theta \partial\vartheta\partial\tau}{\int_0^1 \int_0^1 \rho_e V_z^2 \partial\vartheta\partial\tau}, \tag{4.12}$$

where ρ_e is computed using Eq. (4.8) in conjunction with the stagnation conditions. The resulting swirl number of the flow exiting the combustor is listed in Table 4.3 for both test cases. The associated uncertainty reported in Table 4.3 was computed using Eq. (4.9) to propagate input uncertainties in the same manner as the other performance parameters. However, this method fails to account for uncertainty that results from the assumptions and simplifications of the underlying the mathematical model. In particular, evaluation of the swirl relied on the assumption that the RDE exhaust could be described by a single stagnation state, such that the exit plane density fluctuations were solely caused by the spatio-temporal velocity variations. While the listed uncertainties are then underestimates, the true uncertainty is likely no more than an order of magnitude larger. Given the limitations of the analysis approach discussed above and the short, 10 ms PBL interrogation window, the swirl number of less than 0.1 for both cases supports the assertion that RDEs

produce no net swirl. The experimental confirmation of zero net swirl informs future efforts towards integrating an RDE into a propulsion or power system [9]. In propulsion systems, a net swirl would produce a torque on the vehicle that could potentially depend on the direction of wave propagation. While turbine performance is particularly sensitive to the instantaneous flow angle [104], a net swirl could require designs tailored to account for the mean direction [9].

The utility of exhaust plane velocity measurements for evaluating the performance and thermodynamics of RDEs has been demonstrated on two test cases, alternately exhibiting predominantly single- and counter-rotating wave modes. While a pressure gain relative to the reactant manifold pressure was not achieved due to the high-loss injector design, the technique may enable a future, positive demonstration that would otherwise be obscured by the limitations of the EAP method. In addition, it is promising that a design with high pressure drop and a relatively simple injection scheme achieves reasonable combustion efficiency within a combustor length of 118 mm, resulting in a thermal power density ten times greater than existing systems [77].

4.4 Conclusions

High-speed (100 kHz) velocimetry measurements were performed at the combustor exit plane of a natural gas-air RDE to characterize the flow structure and combustor performance. Two test conditions were studied, one exhibiting a predominantly single-wave mode with intermittent counter-rotating components, and a second operating in a steady counter-rotating mode. Timeseries analysis using the continuous wavelet transform identified synchronous shifts in the frequency and amplitude of pressure and velocity measurements. Phase averaging the point measurements with respect to the detonation wave location revealed the expected structure during single wave operation, with a steep-fronted rise in pressure and broadband chemiluminescence at the wave front followed by the flow turning downstream and in the direction of wave propagation due to the trailing oblique shock attached to the detonation front. Counter-rotating waves produced a more complex flowfield due to the periodic interactions between detonation fronts. Each wave induced flow turning in its direction

of propagation, resulting in large fluctuations in flow angle around the exhaust annulus, while wave interactions produced a sustained deficit in axial velocity aligned with the wave nodes.

In addition to highlighting the single wave flow structure and counter-rotating wave interactions, a new method for computing combustor performance using the time-resolved velocity measurements was presented. While similar to the established EAP method, eliminating the conservative assumption of unity combustor exit Mach number resulted in a total pressure greater than the EAP. In addition to an estimate of an equivalent, steady total pressure, the proposed method computes a corresponding stagnation temperature that is used to estimate the combustion efficiency. All metrics indicated that the test case with counter-rotating waves delivered 5% greater performance than the single-wave case. The small difference in performance can be attributed to the high-loss injector configuration limiting the contribution of wave mode to the overall performance. Finally, the assertion that RDEs do not generate a net swirl in the exhaust products was confirmed by computing the swirl number using the available measurements and an evaluation of key assumptions in the calculation. Application of high-speed particle image velocimetry provided unique, experimental insight into the relationship between flow structure and combustor performance in a rotating detonation engine.

5. ROTATING DETONATION ENGINE OPERABILITY MODELING

5.1 Introduction

The rotating detonation engine (RDE) is the leading concept to achieve the increased thermodynamic cycle efficiency promised by pressure gain combustion due to its high thermal power density, simple design, and relative compatibility with existing propulsion and power architectures [6], [8], [9]. These advantages provide a variety of benefits across a range of applications, including decreased fuel consumption in propulsion systems [14], reduced pumping or compression requirements [105], enhanced flame stabilization in high-speed air-breathing combustors [106], [107], limited need to mitigate combustion instability during development [16], and wide operational limits [83], [105]. However, these potential advantages are tempered by the challenge of harnessing the nonlinear, limit-cycle saturation of a combustion instability inherent to RDE operation, which traditional (deflagrative) combustors have sought to suppress [9], [108]. The nonlinear detonation wave dynamics give rise to a wide range of RDE operating modes observed in experiments and simulations, including one or multiple detonation fronts propagating in one or both directions of a typically annular chamber [80], [109], [110]. Despite the critical role of wave topology and detonation strength in determining the operability and hence performance of an RDE, current models are either computationally expensive or unable to naturally capture the diversity of observed dynamics while maintaining sufficient fidelity to permit direct comparison with experiments. In this paper, we develop a physically derived, reduced-order model for studying the nonlinear detonation dynamics observed in RDEs with sufficient physical fidelity to capture and study variations in combustor design, operating condition, and reactant selection. The coupling between the flow, chemical kinetics, and inlet/outlet flows of mass, energy, and species are evolved in a quasi-one-dimensional (1D) modeling framework based on the Euler equations, permitting the spontaneous development of propagating detonation fronts without a priori specification of wave topology.

5.1.1 Experiments and Balance Physics

Experimental investigations of RDEs have revealed a broad range of wave topologies and concomitant range of wave strengths, typically characterized by detonation velocity or the amplitude of measured pressure oscillations. The operating mode, defined by the number, direction, and strength of the waves, has been observed to vary with operating condition [7], [80], combustor geometry [16], [62], and reactant selection [34]. Spontaneous transitions have also been observed at otherwise stable operating conditions [20]. Potential wave modes include one or multiple co-rotating waves [7], [16], counter-rotating waves of equal or disparate strength [12], [80], and instabilities that can disrupt wave propagation entirely [111]. While extensive experiments have indicated which factors can influence the naturally selected mode of operation, the trends are not universal. For example, numerous experiments have observed that the number of waves increases with the total mass flowrate of reactants, where the nucleation of new waves is associated with a drop in wave velocity that creates a cascading bifurcation structure [7], [15], [112]. However, an experiment focused on high pressure conditions characteristic of rockets observed no change in wave mode despite a nearly 400% increase in total mass flow [16]. Heuristic design rules have been developed for predicting the number of waves and are typically based on the detonation cell size, an intrinsic lengthscale of the reactant mixture [2]. Early work by Bykovskii et al. provides a guideline for the number of waves in terms of the combustor diameter, d, and detonation cell width, λ, as $n = \pi d/(80 \cdot 2^{\pm 1}\lambda)$ [7]. The number of waves suggested by this guideline varies by a factor of four, restricting its applicability beyond simple estimations for preliminary design. St. George et al. developed a similar criterion by enriching mixtures of hydrogen and air with oxygen to independently vary the cell size and annular combustor gap to show that the number of waves increased when the wave front perimeter normalized by the detonation cell width exceeded a critical value, $p/\lambda = 7.4$ [34]. While simple design rules are appealing, experiments with less-detonable reactants have shown that their utility is limited when counter-rotating wave modes are dominant [12]. Ultimately, these criterion fail to capture the diversity of wave topologies and provide no indication of detonation strength or whether an RDE will be able to operate at a given condition.

Based on the diversity of experimentally observed RDE wave topologies and strengths, operating mode selection is unlikely to be governed by an intrinsic lengthscale of detonation fronts propagating in quiescent, homogeneous mixtures. Instead, the relaxation into limit-cycle or mode-locked detonation propagation results from the interplay and global balance between multiple physical processes operating on distinct spatial and temporal scales. Figure 5.1 provides a conceptual illustration of several processes that potentially influence RDE operating mode selection. The coupled unit physics are explicated by tracing the trajectory of a hypothetical fluid parcel along the depicted, wave-frame streamline through the combustor. Fuel and oxidizer are typically introduced from separate plenums in a non-premixed configuration due to the high likelihood of detonation flashback associated with a premixture [7], [9]. Intense turbulence then mixes the fuel and oxidizer before combustion can occur. While the fresh reactants and products from previous cycles are notionally stratified into separate layers, turbulence from the injectors will entrain some fraction of products from prior wave cycles across the interface [16], [79]. The resulting mass fraction of products intermixed with the reactants will then depend on the details of the injector design, its dynamic response to downstream perturbations, and the RDE operating condition. Mixing of reactants and products will increase the fluid parcel temperature and potentially lead to deflagration burning or autoignition if the period between detonation waves is larger than the fluid parcel ignition delay time. The competition between these timescales is a strong function of the reactant combination [54]. In combination with the initial product recirculation, either mechanism reduces the strength of the detonation, resulting in reduced wavespeeds and peak pressures relative to the Chapman-Jouguet condition for a wave in a homogeneous mixture of the reactants [79], [90]. The detonation then consumes the reactants, transferring the hypothetical fluid parcel to the product region. The detonation products are then expanded and exhausted from the combustor as the pressure decays to the conditions immediately ahead of the detonation.

Despite the linear progression that results from following a single fluid parcel, each unit process is coupled to the rest. Reactant injection is modulated by the detonation overpressure, which is in turn influenced by the mixing of reactant and product gas. The blowdown of products from prior cycles also modifies the introduction of fresh products. The com-

bustion chemistry within the detonation front determines the composition of products that recirculate back to the reactants, affecting the kinetics in subsequent waves. The transport of product gases across the contact surface from the downstream to upstream segments of the streamline in Fig. 5.1 visually depicts the closure of this loop. The tight coupling between hydrodynamics, turbulent mixing, heat release, and inflow/exhuast of reactants then necessitates a global balance between all physical processes. This global balance across a wide range of scales and the separation thereof is a unique aspect of RDEs [113].

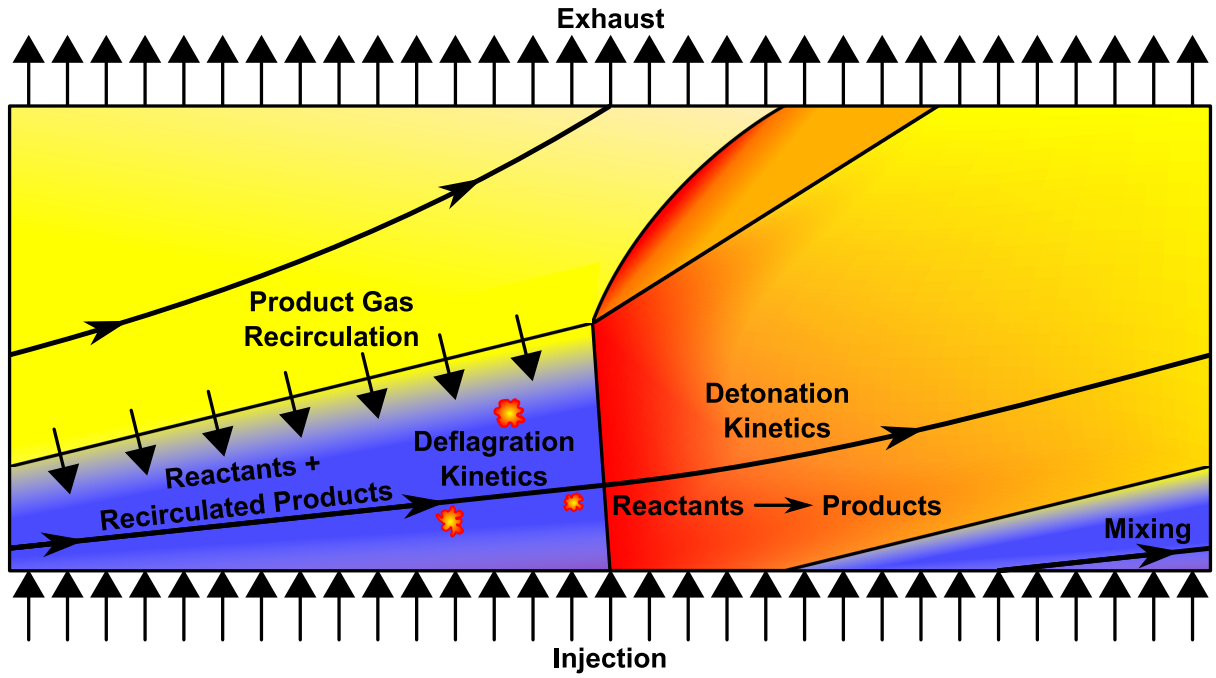

Figure 5.1. Conceptual schematic of physical processes governing RDE mode selection and subsequently dynamics of detonation propagation.

Fig. 5.1 only illustrates the quasi-steady state, limit-cycle operation of an RDE. Operating mode selection is expected to principally occur during initiation and combustor startup, underscoring that any physical model must be capable of capturing this sequence of events. At a global level, rotating detonation waves form due to confinement of energy release in the annular channel, creating sharp gradients in temperature and pressure that self-steepen as a result of Arrhenius kinetics and form shock-coupled reaction fronts in the periodic medium. The coupled evolution of hydrodynamics and chemical kinetics subject to the supply of fresh

reactants by the injection and exhaust of products at the outlet are the same governing processes found in the steady-state discussed above. The physics that govern limit-cycle operation are then the same processes at play during initiation and startup, permitting the natural evolution of the mode-locked equilibrium depicted in Fig. 5.1.

5.1.2 A Hierarchy of Models

A wide variety of computational models have been used in conjunction with experiments to enhance understanding of the physics governing RDE operation. The tradeoff between physical fidelity and computational cost is a principal consideration in the development of any model, particularly for the coupled multi-physics occurring across spatial and temporal scales spanning orders of magnitude found in RDEs. Similar to the hierarchy of models and experiments developed for the study of combustion instability [108], [114], a similar series of models of increasing complexity has been developed for the study of RDEs. The range includes steady-state thermodynamic, dynamic, two-dimensional CFD, and 3D unsteady simulations with detailed injection geometry.

The first and simplest type of model used to study RDEs focus on the thermodynamic cycle and ensuing combustor performance. Such inexpensive models are well suited for parametric studies across multiple variables, including combustor geometry, reactant selection, and operating condition. Specific applications include analysis of flight vehicle performance [68] or nozzle design and propellant selection [65]. Early modeling efforts were conducted by Nicholls et al. [11] and Adamson et al. [115], who developed a steady-state, azimuthally 1D model of the RDE flowfield for preliminary performance estimates. Their analysis considered the limiting cases of perfect mixing between reactants and products and complete stratification between the two, similar to Fig. 5.1. As a steady-state model, a priori specification of wave topology was required, but the authors made the important observation that reactant-product stratification plays a key role in the RDE flow physics. The more recent model of Kaemming et al. [55] follows representative fluid parcels through the multiple, distinct thermodynamic paths found in an RDE to study the effect of loss mechanisms on combustor performance, including deflagration burning, exit flow distortion, lateral relief at

the detonation front, and secondary shocks. As a final example, Fievisohn and Yu developed a model of the RDE flowfield using the Method of Characteristics [116]. This approach accounts for the fundamentally two-dimensional nature of the flowfield, but again requires specification of the operating mode.

Dynamic models form the second class in the RDE modeling hierarchy. These range from approximate, asymptotic model forms to time-dependent solutions of the Euler or Navier Stokes equations with additional modeling terms. Asymptotic models share heritage with the rich field of detonation analogs, which have traditionally been used to study the linear stability, bifurcations, and one- or two-dimensional dynamics of detonations [117]–[119]. Koch et al. [120] recently extended Majda's detonation analog with reactant injection and product exhaust source terms to study the process of RDE mode-locking and subsequent wave bifurcations. The model exhibited qualitative agreement with the transient wave nucleation or destruction process observed in RDEs, as well as the global wave bifurcation structure. While this approach is potentially suitable for a data-fit modeling approach, the asymptotic form inhibits direct comparison with RDE experiments. Fievisohn et al. developed a reactor network model for predicting the RDE wave strength (velocity, pressure oscillation amplitude) [121]. This model uses separate, 0D reactors for the reactants and products to incorporate the key physics of injection, reactant-product stratification and subsequent mixing, and chemical kinetics in both regions. However, the 0D format lacks the azimuthal dynamics required to capture the process of RDE mode selection. Several researchers have developed 1D models based on solving the Euler or Navier Stokes equations in the azimuthal direction of an RDE [113], [122], [123]. Gupta et al. [122] and Humble et al. [123] both incorporated detailed chemical kinetics in their model, but encountered issues with wave failure after a few cycles. Koch and Kutz found greater success with their approach of single-step chemistry in conjunction with modeling terms to emulate non-premixed injection [113]. The model explicitly varied the timescales of injection, reaction, and mixing to observe a range of RDE operating modes comparable to those observed in experiments, including wave bifurcations and counter-rotating modes. However, the 1D format effectively assumes perfect mixing between reactants and products, corresponding to the limiting case considered in the steady-state model of Nicholls [11] and Adamson [115]. The recent successes of dynamic

RDE models are promising, but each approach has required simplifications by removing azimuthal dynamics, or by ignoring the spatial separation between injected reactants and detonation products.

The ratio between the annulus width and mean diameter of a RDE is typically much greater than unity, which permits the domain to be unrolled in the azimuthal direction and reasonably approximated as 2D. This modeling approach was pioneered by Zhdan et al. [124], who continuted to refine the technique and analyze additional conditions as computers became more capable [125], [126]. Two-dimensional simulations have since been used to interrogate the effect of combustor geometry, reactant selection, boundary conditions, and different modeling approaches on the flow physics and thermodynamic processes occuring within RDEs [14], [17], [81], [106], [127], [128]. We highlight several observations derived from these studies pertinent to the present issue of RDE mode selection. Zhdan et al. [124] note the existance of a neutral Mach line (NML), where the detonation products become axially supersonic and hence can no longer influence the upstream wave front dynamics. A similar region appears in the simulations of Schwer et al. [81], where the NML forms immediately downstream of the detonation front. This suggests that the physical processes influencing RDE mode selection must principally occur within the axial length of the detonation front, as downstream perturbations cannot travel upstream past the NML. A unique aspect of the work by Zhdan et al. is the view that the length of the periodic dimension in 2D RDE simulations is not a free parameter and instead must be determined during the course of the simulation [126]. In correlating with experimental results, they conclude that the circumferential domain length must not be greater than twice the minimum dimension capable of supporting a rotating detonation front, as the model format "[does] not contain the mechanism of [Transverse Detonation Wave] multiplication" [126]. This perspective implicitly defines a mode selection criterion that the number of waves in an RDE is determined by the combustor circumference relative to the minimum period. While Zhdan et al. refer to this minimum domain length as an eigenvalue of the system, the absence of an explicitly formulated eigenvalue problem suggests that the minimum period is better described as the "minimal unit" of the rotating detonation, in analogy to the similar concept in turbulence theory [129]. This understanding of RDE mode selection fails to account for the diversity

of experimentally observed wave modes, but highlights potential limitations of 2D RDE simulations for the present problem. For example, recent simulations have used alternating wall/injector boundary conditions to emulate the effect of non-premixed injection schemes typically used in RDEs [127], [128]. However, the mixing both between fuel and oxidizer and between reactants and products will depend on the fundamentally 3D nature of turbulence.

Three-dimensional, time-dependent simulations with detailed injection geometry provide the final, highest-fidelity method of modeling RDEs, but require extensive computational resources. These simulations often use turbulence models based on the large eddy simulation approach in conjunction with detailed models for the chemical kinetics. Typical studies examine instantaneous and averaged snapshots of scalar fields, along with statistical analysis of the flow relative to the wavefront or of global heat release [93], [109], [110], [130]. While parametric surveys of operating condition with comparison to experiment have been conducted for some geometries, the simulations fail to consistently predict the correct number of waves [109], [130]. Though high-fidelity simulations have become increasingly common, the computational cost remains too large to conduct more complete sweeps to determine if trends are captured correctly.

5.1.3 Objective

We seek to develop a reduced-order model that can begin to address the phenomena of RDE mode selection in a manner consistent with the physical processes observed in experiments and detailed simulations. We adopt a quasi-1D framework to reduce the computational cost and permit broad, parametric studies while retaining the key physical features and processes identified in Section 5.1.1 necessary for modeling the nonlinear detonation wave dynamics observed in RDEs. The flow dynamics in the azimuthal direction of the annulus of an RDE are modeled using the Euler equations to allow combustion fronts to form and self-steepen into detonation waves. Stratification between reactants and products is modeled by extending the 1D domain with a second cell in the axial direction. The interface between the two regions is modeled as a contact surface whose axial location evolves in response to the azimuthal dynamics. The reactant and product domains are then coupled by computing

the flux of the conserved quantities between domains when interface displacement produces overlap between adjacent cells. Chemical reactions, injection of reactants, and exhaust of products are finally modeled as source terms in the appropriate region.

Our model builds upon the recent successes in dynamic RDE modeling discussed in Section 5.1.2. Each of the dynamic and quasi-steady state thermodynamic models depended upon one of two major simplifications that limit their applicability when drawing comparison to experiments. Either the wave mode had to be provided as an input to the model, or the model ignored the fundamentally 2D nature of the RDE flowfield that produces stratification between newly injected reactants and detonation products. This simplification corresponds to the perfect mixing limit of the model developed by Nicholls [11]. We address these limitations by creating a model that combines explicit stratification, as in Fievisohn et al. [121], with the Euler equations for 1D azimuthal dynamics, as in Koch and Kutz [113], and hence more faithfully recreates the physics governing RDE mode selection in a computationally tractable manner. The quasi-1D format allows us to further address the limitations of 2D RDE simulations identified in Section 5.1.2 with the inclusion of modeling terms that can be tuned to mimic the global properties of the non-premixed, highly turbulent injection schemes found in experiments that impact the RDE mode-locking process.

We first review the model formulation and numerical implementation. Initial results and verification studies are then presented. Finally, we conclude with a discussion of the unique aspects of the model and areas of future development.

5.2 Model

The model is formulated to resolve the unit physics relevant to the process of RDE mode selection and subsequent limit-cycle propagation discussed in Section 5.1.1 and depicted in Fig. 5.1. In particular, the model must be able to capture the stratification between reactants and products, the azimuthal fluid dynamics responsible for detonation propagation, chemical reactions, and the inflow and outflow of species and energy. The quasi-1D approach to modeling the domain is first introduced in conjunction with the governing equations, followed by the logic and equations that determine the evolution of the interface between reactants

and products. We then describe the source terms that control the injection of reactants and exhaust of products, and conclude with a description of the numerical implementation of the model.

5.2.1 Quasi-1D Domain

The observations from experiments and simulations noted in Section 5.1 have indicated that RDE wave dynamics are governed by the physical processes occurring within the axial length of the detonation front, extending from the injector face at the chamber head end to the NML. While fresh reactants are physically separated from detonation products across a contact surface, axial gradients within this region are otherwise negligible compared to the azimuthal gradients across the detonation front and are therefore neglected. A quasi-1D modeling approach is then adopted where the azimuthal dynamics are simulated while the axial stratification is modeled as separate domains that are nominally labeled "reactants" and "products." The quasi-1D Euler equations are used as the foundation of our model, including additional source terms for reaction chemistry and inflows/outflows:

$$\frac{\partial \mathbf{q}}{\partial t} + \frac{\partial \mathbf{f}}{\partial x} = \mathbf{s}_{chem} + \mathbf{s}_{bc}, \tag{5.1}$$

where

$$\mathbf{q} = \begin{bmatrix} \rho Y_1 \\ \vdots \\ \rho Y_N \\ \rho u \\ \rho \mathrm{e} \end{bmatrix}, \quad \mathbf{f} = \begin{bmatrix} \rho Y_1 u \\ \vdots \\ \rho Y_N u \\ \rho u^2 + p \\ \rho u \mathrm{e} + p u \end{bmatrix}, \tag{5.2}$$

are respectively the conserved state variable and inviscid flux vectors. The model is formulated to permit a thermally perfect gas in conjunction with an ideal gas equation of state,

$$\mathrm{e} = \int_{T_{ref}}^{T} c_v d\tau + \frac{u^2}{2}, \tag{5.3}$$

$$p = \rho R T, \tag{5.4}$$

$$R = R_u \sum_{n=1}^{N} \frac{Y_n}{W_n}, \tag{5.5}$$

where T_{ref} is the reference temperature, R_u is the universal gas constant, and W_n is the molecular weight of the nth species.

The reaction chemistry source term is given as

$$\mathbf{s}_{chem} = \begin{bmatrix} \dot{\omega}_1 \\ \vdots \\ \dot{\omega}_N \\ 0 \\ -\sum_{n=1}^{N} \Delta \mathrm{e}_{f,n}{}^{\circ}\left(T_{ref}\right) \dot{\omega}_n \end{bmatrix}, \tag{5.6}$$

where $\dot{\omega}_n$ and $\Delta \mathrm{e}_{f,n}{}^{\circ}\left(T_{ref}\right)$ are respectively the net production rate and the formation energy at the reference temperature for the nth species. The source term for injection and exhaust, $\mathbf{s}_{bc}$, will be discussed in Section 5.2.3.

The stratification between reactants and products is incorporated in our model by extending the domain with an additional cell in the axial direction, as illustrated in the insets of Fig. 5.2. With injection at the bottom and exhaust at the top of the RDE flowfield schematic of Fig. 5.2, the bottom row of cells then corresponds to a notional reactant region, while the top row will principally consist of detonation products. The height of each individual cell evolves in the course of the simulation according to the rules discussed in Section 5.2.2, though the total height of the domain remains fixed as h_{dom}. The two domains are coupled by evolving the flow not just between adjacent cells within a single domain, but also between domains when the difference between the height of adjacent cells produces overlap between the reactant and product domains. The interface evolves to produce a step change in height

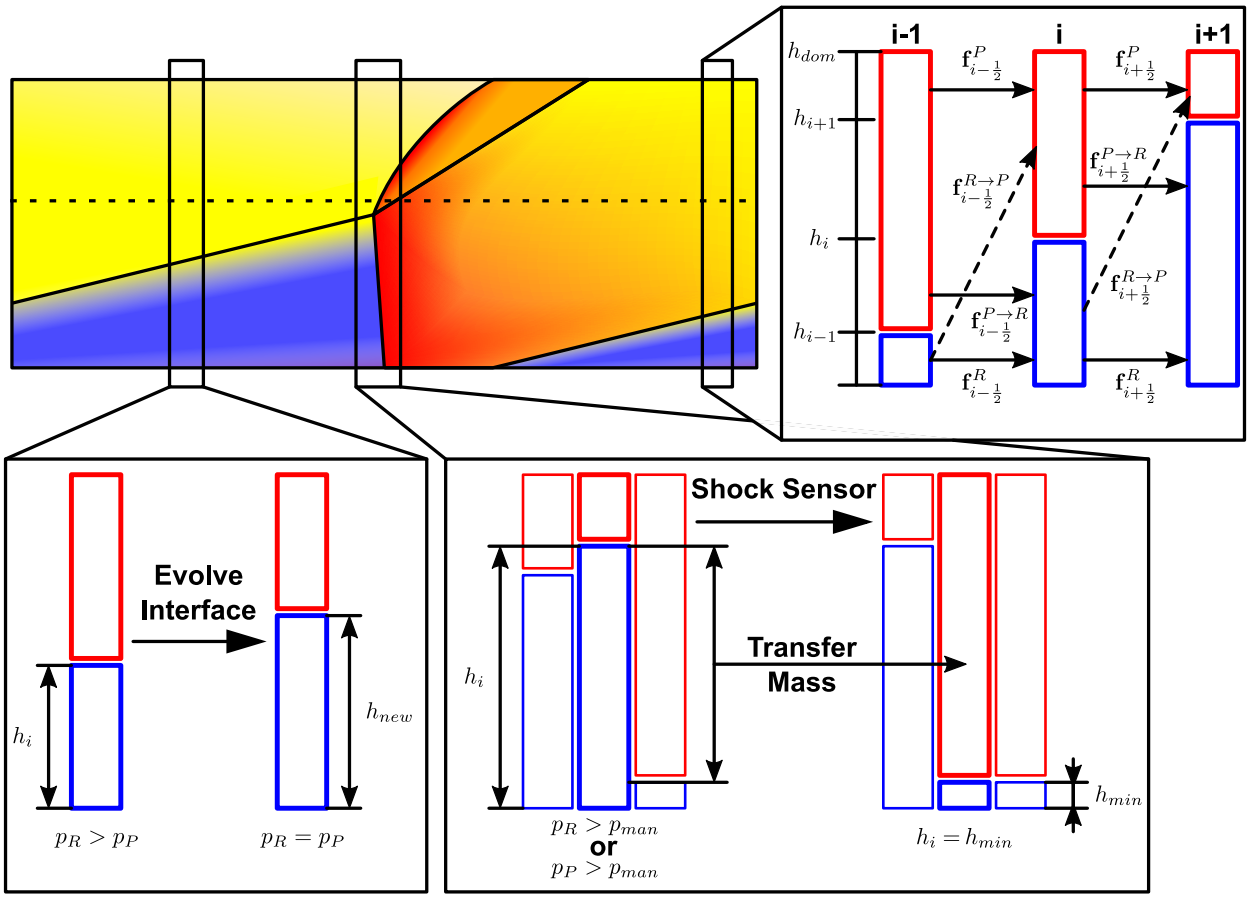

Figure 5.2. Model structure relative to the typical RDE flowfield. Within all insets, blue and red respectively indicate reactant and product domains. Top right inset: Separation of domain into reactant and product regions with intra- and inter-domain fluxes. Bottom right inset: Interface modification by shock sensor for enforcing domain overlap and mass transfer from reactants to products. Bottom left inset: Evolution procedure for interface applied to all cells.

at the detonation front, permitting freshly injected reactants to be transferred to the product region, exothermically converted to products, and exhausted.

The intra- and inter- domain fluxes are illustrated in the top right inset of Fig. 5.2, where the inviscid flux within the reactant (product) domain is denoted $\mathbf{f}^R\left(\mathbf{f}^P\right)$, and the flux from the reactants to the products (products to reactants) is denoted $\mathbf{f}^{R\to P}\left(\mathbf{f}^{P\to R}\right)$. The solid lines show which fluxes would be active given the depicted configuration of cell interface heights, while the broken lines show the remaining, inactive fluxes. Using a finite

volume implementation, the resulting semi-discrete form of the conservation equations for the reactant domain is given as:

$$\frac{\partial \mathbf{q}_{\mathrm{i}}^{R}}{\partial t}+\frac{1}{\Delta x \cdot h_{\mathrm{i}}}\left(A_{\mathrm{i}+\frac{1}{2}}^{R} \cdot \mathbf{f}_{\mathrm{i}+\frac{1}{2}}^{R}-A_{\mathrm{i}-\frac{1}{2}}^{R} \cdot \mathbf{f}_{\mathrm{i}-\frac{1}{2}}^{R}+A_{\mathrm{i}+\frac{1}{2}}^{R \rightarrow P} \cdot \mathbf{f}_{\mathrm{i}+\frac{1}{2}}^{R \rightarrow P}-A_{\mathrm{i}-\frac{1}{2}}^{P \rightarrow R} \cdot \mathbf{f}_{\mathrm{i}-\frac{1}{2}}^{P \rightarrow R}\right)=\mathbf{s}_{\mathrm{i}}^{R}, \tag{5.7}$$

where $\mathbf{q}_{\mathrm{i}}^{R}$ and $\mathbf{s}_{\mathrm{i}}^{R}$ are respectively the state vector of conserved variables and source term for the reactant region. The flux areas, A, are computed as

$$\begin{aligned} A_{\mathrm{i}+\frac{1}{2}}^{R}&=\min\left(h_{\mathrm{i}}, h_{\mathrm{i}+1}\right), \quad A_{\mathrm{i}+\frac{1}{2}}^{R \rightarrow P}=\left(h_{\mathrm{i}}-h_{\mathrm{i}+1}\right) \cdot H\left(h_{\mathrm{i}}-h_{\mathrm{i}+1}-h_{lim}\right), \\ A_{\mathrm{i}-\frac{1}{2}}^{R}&=\min\left(h_{\mathrm{i}}, h_{\mathrm{i}-1}\right), \quad A_{\mathrm{i}-\frac{1}{2}}^{P \rightarrow R}=\left(h_{\mathrm{i}}-h_{\mathrm{i}-1}\right) \cdot H\left(h_{\mathrm{i}}-h_{\mathrm{i}-1}-h_{lim}\right). \end{aligned} \tag{5.8}$$

A Heaviside function, H, has been used in Eq. (5.8) to require a user-defined minimum interface length, h_{lim}, between the reactant and product regions before the inter-domain fluxes are applied. This prevents spurious interaction between the reactant and product regions, such that coupling only occurs at the detonation wavefront. The minimum overlap for reactant-product coupling to activate has been set as 10% of the overall domain height for all reported simulations. The corresponding equations for the evolution of the conserved quantities in product region and associated flux areas are analogous to Eqs. (5.7-5.8).

5.2.2 Interface Dynamics

In order to permit proper coupling between the two domains, the interface must evolve to track the detonation front without a priori specification of the RDE operating mode. The interface evolution procedure is then composed of two components: a heuristic shock sensor to ensure coupling between the domains at the shock front, and a physically derived rule for setting the interface height at all other points. We first describe the heuristic shock sensor, shown schematically in the lower right inset of Fig. 5.2. The shock sensor is activated whenever the pressure in either domain increases above the reactant manifold pressure, p_{man}, as this indicates that reactants have been checked off by the overpressure. In a typical RDE cycle, the pressure behind the leading shock of a detonation front can reach several times

the manifold pressure before quickly decaying, making the selected condition a reasonable indicator of the detonation front. Figure 5.2 shows how when the shock sensor is activated in a given cell, the reactant domain height is immediately set to a user-defined minimum value, h_{min}, and the corresponding conserved quantities are transferred to the product region according to

$$\mathbf{q}_{\mathrm{i}}^{P} = \frac{(h_{dom} - h_{\mathrm{i}})\,\mathbf{q}_{\mathrm{i}}^{P} + (h_{\mathrm{i}} - h_{min})\,\mathbf{q}_{\mathrm{i}}^{R}}{h_{dom} - h_{min}}. \tag{5.9}$$

This approach serves the dual purpose of producing sufficient overlap between domains to ensure transport coupling at the detonation front and assisting in the transfer of fuel and oxidizer to the product region to subsequently be consumed. The minimum interface height, h_{min}, is selected to prevent numerical stiffness in the source terms and has been set to 1% of the total domain height for all reported simulations.

After the shock sensor is applied, the interface position at all cells is evolved to balance the pressure between the reactant and product domains. The reactant-product interface produces a contact surface in the canonical 2D RDE flowfield, where the pressure and velocity are continuous, but discontinuities can exist in species, temperature, and density. While our model also permits a discontinuity in velocity across the interface, balancing the pressure between domains produces a physically consistent method of evolving the interface height. The interface evolution process is illustrated schematically in the bottom left inset of Fig. 5.2 and proceeds as follows. The interface height required for $p_R = p_P$ is first computed assuming isothermal volume change:

$$h_{new} = \frac{h_{dom} \cdot h \cdot p_R}{h_{dom} \cdot p_P + h \cdot (p_R - p_P)}. \tag{5.10}$$

The domain height is then limited so that neither domain becomes too small

$$h_{new} = \min\left(h_{dom} - h_{min}, \max\left(h_{new}, h_{min}\right)\right), \tag{5.11}$$

where h_{min} is the same minimum domain height as before. The cell velocity is also limited to the speed of sound computed using the Roe-averaged state at the domain interface. This

prevents non-physical movement of the contact surface, but the limit is rarely applied in practice. Finally, the solution state is updated by applying isothermal expansion/compression to each domain:

$$\begin{aligned} p_R &= p_R \cdot \frac{h}{h_{new}}, \quad p_P = p_P \cdot \frac{h_{dom} - h}{h_{dom} - h_{new}} \\ \rho_R &= \rho_R \cdot \frac{h}{h_{new}}, \quad \rho_P = \rho_P \cdot \frac{h_{dom} - h}{h_{dom} - h_{new}}. \end{aligned} \tag{5.12}$$

The interface evolution procedure is applied in the order described, where the shock sensor is first used to account for the updated location of the detonation front, and the pressure is then isothermally equillibrated between domains to enforce the physical requirement of a contact surface.

5.2.3 Injection and Exhaust

The injection of fuel and oxidizer into the reactant domain and exhaust of combustion products from the product region are modeled as source terms applied to the respective domain. The injection of reactants is modeled as a series of micro-nozzles with specified throat area supplied by a premixed reactant manifold with known stagnation conditions, T_{man}, p_{man}, consistent with the method used in 2D RDE simulations [14], [81], [124]. The Mach number of reactants entering the reactant region is then given as

$$M_{\text{in}} = \min \left[1, \sqrt{\frac{2}{\gamma_{man} - 1} \left(\left(\frac{p_{man}}{\min\left(p_R, p_{man}\right)} \right)^{\frac{\gamma_{man}-1}{\gamma_{man}}} - 1 \right)} \right], \tag{5.13}$$

where p_R is the pressure in the reactant domain and γ_{man} is the ratio of specific heats for the premixed reactants at the manifold stagnation conditions. The pressure in Eq. (5.13) has been limited to prevent imaginary results and the Mach number has been limited to one to produce choked flow. The mass flux of reactants is then

$$\dot{m}_{\text{in}} = \frac{A_{\text{i}}}{A_c} p_{man} \sqrt{\frac{\gamma_{man}}{R_{man} T_{man}}} M_{\text{in}} \left(1 + \frac{\gamma_{man} - 1}{2} M_{\text{in}}^2 \right)^{-\frac{\gamma_{man}+1}{2(\gamma_{man}-1)}}, \tag{5.14}$$

where A_i/A_c is the area ratio between the injector throat and chamber cross section. This implementation of the injector boundary condition neglects any backflow of fluid into the injector resulting from the high pressure behind the detonation wave. The source term for the reactant domain is now

$$\mathbf{s}_{bc}^{R} = \frac{\dot{m}_\mathrm{in}}{h} \cdot \begin{bmatrix} Y_1^{man} \\ \vdots \\ Y_N^{man} \\ 0 \\ \frac{R_{man} T_{man}}{\gamma_{man}-1} \end{bmatrix}, \tag{5.15}$$

where the inlet mass flux is divided by the reactant layer height because it is not a volumetric source, but instead emulates an upstream boundary condition.

Similar to the reactant injection, the Mach number of the exhaust from the product region is computed as

$$M_{out} = \min \left[1, \sqrt{\frac{2}{\gamma_P - 1} \left(\left(\frac{p_P}{\min\left(p_P, p_\infty\right)} \right)^{\frac{\gamma_P - 1}{\gamma_P}} - 1 \right)} \right], \tag{5.16}$$

and the corresponding mass flux is

$$\dot{m}_{out} = \frac{A_\mathrm{e}}{A_c} p_P \sqrt{\frac{\gamma_P}{R_P T_P}} M_{out} \left(1 + \frac{\gamma_P - 1}{2} M_{out}^2 \right)^{-\frac{\gamma_P + 1}{2(\gamma_P - 1)}}. \tag{5.17}$$

Here, p_∞ is the ambient pressure and A_e/A_c is the area ratio between the RDE exit and chamber area. The source term for the product domain is then computed as

$$\mathbf{s}_{bc}^{P} = -\frac{\dot{m}_{out}}{h_{dom} - h} \cdot \begin{bmatrix} Y_1^{P} \\ \vdots \\ Y_N^{P} \\ 0 \\ \frac{R_P T_P}{\gamma_P - 1} \end{bmatrix}, \tag{5.18}$$

where the height of the product domain has been accounted for to again emulate a boundary flux instead of a volumetric source.

5.2.4 Numerical Implementation

We conclude our discussion of the model formulation with a brief description of the numerical methods employed and other implementation details. The open-source StanShock solver [131] for 1D, compressible, reacting flows is used as the foundation for the model. The governing equations are discretized using the finite volume method, where a fifth-order WENO scheme is used to reconstruct the cell edge states. This scheme ensures that spurious oscillations are not introduced at the expected shock fronts. In addition, the WENO interpolation is conducted using the characteristic variables, which has been found to assist in the reduction of oscillations near discontinuities [132]. The double-flux model is used in conjunction with the Harten-Lax-van Leer contact (HLLC) approximate Riemann solver to compute the cell fluxes, as implemented in the original StanShock solver [131]. The double-flux model requires two evaluations of the flux per cell face instead of one, but reduces pressure oscillations for multicomponent flows with variable specific heats [132]. Finally, the species thermodynamic properties and reaction kinetics are evaluated using Cantera [133].

The advection and source terms are advanced in time using an operating splitting framework to permit application-specific integration schemes. The advection terms are advanced using a third-order strong stability preserving Runge-Kutta scheme commonly used in compressible, reacting flow simulations [132]. The injection and exhaust source term, $\mathbf{s}_{bc}$, is advanced using a second-order Runge-Kutta scheme, as the limit on minimum cell size eliminates potential sources of stiffness. In contrast, the reaction chemistry results in a stiff system of differential equations that must be advanced implicitly. Two integration schemes are implemented and can be selected depending on the expected timestep. Large timesteps are best handled using the Cantera reactor class, which uses CVODE [133]. However, the multistep BDF scheme in CVODE has a high startup cost and therefore can be suboptimal for compressible, reacting flow simulations, where the CFL criterion requires small timesteps for the advection terms [134]. An additional, semi-implicit Rosenbrock-Krylov integration

scheme, ROK4E [134], is then available for when the timestep becomes sufficiently small, typically $\Delta t < 30\ ns$.

The operating splitting scheme then advances the different physical processes in the following order:

$$\mathbf{q}\left(t + 2\Delta t\right) = \mathcal{S}_{\Delta t} \circ \mathcal{N}_{\Delta t} \circ \mathcal{S}_{\Delta t} \circ \mathcal{C}_{2\Delta t} \circ \mathcal{N}_{\Delta t} \circ \mathbf{q}\left(t\right), \tag{5.19}$$

where $\mathcal{N}$, $\mathcal{C}$, and $\mathcal{S}$ are the respectively the operators for advection, chemistry, and the combination of the inlet/outlet source term and interface advancement. Reaction chemistry is only advanced in the product domain for all reported simulations. The timestep, Δt, is set by CFL condition and user selected Courant number. The order was selected to reduce the frequency of chemistry integration steps, which are found to be the largest contributor to the computational cost of the simulation. In preliminary testing, the solution was found to be most sensitive to the coupling between the advection and interface evolution. The operators are therefore ordered such that the interface is always updated immediately before the advection is advanced. It was further found that this coupling also drives the timestep requirements to achieve a temporally converged solution, supporting the selected operator splitting sequence.

The underlying StanShock solver is written in object-oriented Python for portability and modularity, and our model maintains this implementation approach and philosophy to streamline additional development for subsequent studies. While the ROK4E integration scheme requires interfacing with an external, compiled library, the simulation is able to fall back on the built in integrator included with Cantera. The solver has also been modified to distribute the domain across multiple cores via MPI for Python [135], which enables use of fine grids required to resolve the detonation front and long integration times required for the waves to reach a mode-locked equilibrium.

5.3 Verification and Sensitivity Analysis

A formal verification of the model is non-trivial because the dynamic interface and complex source terms preclude an analytic solution or canonical test case for comparison. We

therefore take a multistep approach to verifying the model. We first note that the underlying numerical methods for WENO interpolation, flux calculation, thermophysical property evaluation, and reaction chemistry have been verified in the original StanShock solver, and remained unchanged in the current model [131]. We next enumerate the physical and user-specified parameters required as model inputs and review a test case using a notional, baseline RDE configuration to demonstrate that the model is capable of naturally producing detonation wave dynamics representative of RDEs without a priori specification of operating mode. Results from a spatial and temporal convergence study are presented. Finally, we conduct sensitivity studies to investigate the impact of the user-specified parameters on model results.

5.3.1 Model Parameters

The outcome of each numerical experiment conducted with our model is a function of the parameters that define the RDE geometry, operating condition, user-defined model settings, and inputs to control the numerical methods. We describe all required parameters vis-à-vis the baseline RDE configuration, which are subsequently summarized in Table 5.1. The first set of parameters are set by the RDE design and geometry. The length of the periodic model domain is set as the annulus centerline diameter, selected as 300 mm to correspond with a 95 mm diameter combustor. The combustor annular gap is set as 5 mm, but is only used in post-processing for performance calculations such as computing the delivered thrust or total mass flowrate of reactants. The inlet area ratio, A_i/A_c, is set as 0.2 and the outlet area ratio, A_e/A_c, is unity, corresponding to a combustor with no geometric exit contraction.

The second set of parameters determines the operating condition and principally influences the premixed reactant manifold state. This includes the choice of reactants, selected as methane and oxygen for the baseline configuration, and equivalence ratio, which is set as unity. The manifold temperature and pressure are respectively set as 300 K and 1 MPa, while the ambient pressure is set as 100 kPa. The model requires several user-defined parameters for controlling the interface evolution, including the total domain height, minimum domain height, and minimum height for inter-domain coupling to be activated in Eqs. (5.7-

5.8). The domain height is set as 50 mm, while the minimum domain and coupling heights are respectively set as 1% and 10% of the domain height for the baseline RDE, as noted in Section 5.2.1 and 5.2.2. Reaction kinetics calculations use the FFCMy-12 model [136], which has previously been used for 3D RDE simulations [110]. Finally, the simulation spatial resolution and timestep are set by the number of cells and Courant number.

Table 5.1. Simulation parameters for baseline RDE.

Parameter	Value	Description
$L = \pi D_c$	300 mm	Domain length
Δ	5 mm	Annulus gap
A_i/A_c	0.2	Inlet to chamber area ratio
A_e/A_c	1	Outlet to chamber area ratio
Fuel	CH_4	Species
Oxidizer	O_2	Species
ϕ	1	Equivalence ratio
P_{man}	1 MPa	Reactant manifold pressure
T_{man}	300 K	Reactant manifold temperature
P_∞	100 kPa	Ambient pressure
h_{dom}	50 mm	Total domain height
h_{min}/h_{dom}	1%	Minimum domain height
h_{lim}/h_{dom}	10%	Minimum coupling height
Mechanism	FFCMy-12	Reaction chemistry model
N	2000	Number of cells
CFL	0.2	Courant number

5.3.2 Typical Results

The baseline RDE geometry and operating conditions enumerated in Table 5.1 are used as the initial test conditions for the model. Unless noted otherwise, all simulations are initiated using an manufactured blast profile. The peak pressure of the blast is set as $10P_{man}$ (10 MPa for the baseline configuration) and is centered at $0.45L < x < 0.55L$ in both the reactant and product domains. The temperature of the product domain in this region is set as 2000 K, while it is set to T_{man} elsewhere. The pressure and temperature profiles are generated using hyperbolic tangent functions to prevent the spectrum of the initial condition from changing with grid refinement. The initial species in the reactant domain are set as a mixture of the

selected fuel and oxidizer at the specified equivalence ratio, modulated by a sinusoidal profile of water vapor to break the symmetry of the initial conditions. The product domain is set as pure water vapor. Finally, the interface height is set as half the total domain height, expect where the pressure exceeds P_{man}, where it is set as h_{min} in accordance with the shock front evolution procedure described in Section 5.2.2.

Figure 5.3 illustrates the startup transient and progression to a stable limit-cycle with two waves propagating in the $-x$ direction using contours of pressure in the product domain. The initial shocks propagating in both directions are nonreactive, but chemical reactions initiate at the wave fronts after the first collision near $t = 0.1$ ms. An additional $-x$ wave nucleates shortly after the second interaction of the original shock fronts and subsequently strengthens over several cycles. The initial $+x$ wave eventually dissipates after repeated interactions with the $-x$-running waves, leaving the two waves to enter a mode-locked equilibrium. The detonation fronts propagate with a velocity of 1980 m/s, which is 82% of the Chapman-Jouguet velocity of 2420 m/s for the reactant mixture. The total flowrate of reactants, 0.55 kg/s for this baseline RDE condition, is not specified as an input and is instead an outcome of the simulation due to the implementation of the reactant injection source term.

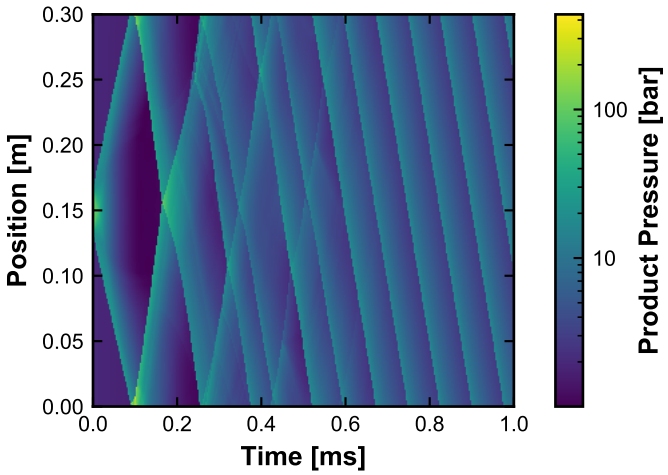

Figure 5.3. Product region pressure $\theta - t$ diagram illustrating startup transient and establishment of a steady, limit-cycle with 2 waves for baseline RDE configuration.

Representative solution profiles after the detonation waves have stabilized in a limit-cycle are shown in Fig. 5.4. The contours of Fig. 5.4a display the density in each region of the model, with the red profile demarcating the boundary between the reactant and product domains. While the product domain extends to a height of 50 mm, the vertical axis has been truncated for clarity. The interface develops a shape similar to that shown in the conceptual schematic of Fig. 5.1, with a step change in height at the wavefronts near $x = 0.1, 0.25$ m producing vertical overlap between adjacent cells in the two domains, followed by expansion back to the maximum height as the pressure behind the wavefront decays and fresh reactants are injected into the reactant domain. The detonation front stabilizes at a height of 10 mm, which is dynamically set by the balance between the blowdown of products and injection of reactants. The pressure profiles of Fig. 5.4c demonstrate that the pressure in the two domains can become mismatched at the wavefront. This results from the minimum domain height, as once the interface has been set to the minimum height at the shock front it is unable to further compress the reactant domain to match the elevated product domain pressure. Additional reactants are then injected until reactant domain pressure reaches P_{man} and the injection is checked off. The pressures are then equalized behind the wave front after sufficient products have been exhausted to permit interface movement. The temperature in the reactant domain remains near the manifold temperature for the entirety of the cycle, while the product region temperature remains near its maximum. The product domain temperature is momentarily reduced as reactants are transferred at the detonation front, but the highly concentrated heat release rate shown in Fig. 5.4e indicates that the fresh reactants are immediately consumed behind the wave front. The heat release rate profile indicates that reactions have completed in the first few cells behind the wave front.

5.3.3 Convergence

Model convergence is assessed by conducting a series of simulations starting from the limit-cycle solution shown in Fig. 5.4. While the simulation presented in Section 5.3.2 uses a mesh resolution of 2000 cells and Courant number of 0.2, the convergence study uses a Courant number of 0.4 and span of mesh resolutions from 1000 to 32000 cells with a

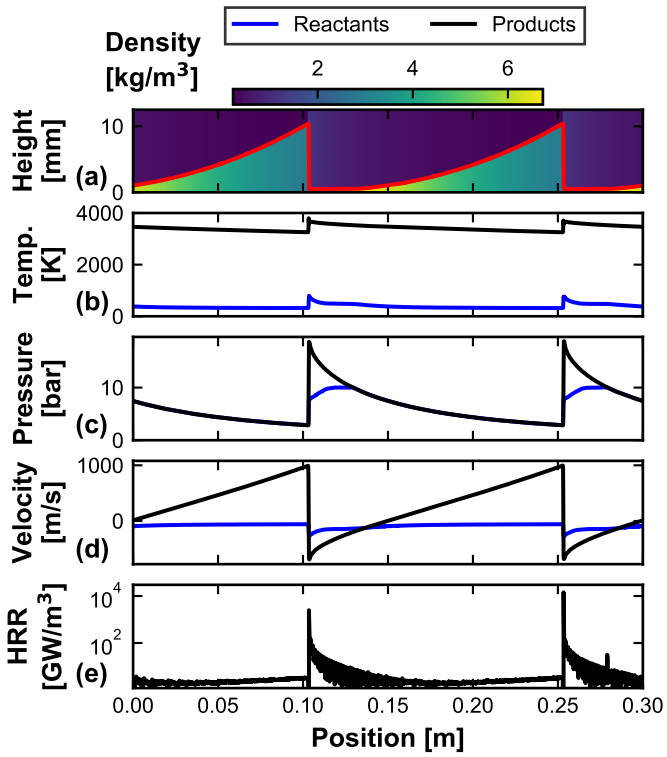

Figure 5.4. Instantaneous profiles of (a) interface location, (b) temperature, (c) pressure, (d) velocity, and (e) heat release rate. Contours in panel (a) show density in reactant and product regions.

refinement factor of two between successive cases. Each case is advanced by 0.2 ms, or approximately one full wave revolution. The profiles of interface height and product domain pressure for each simulation are overlaid in Fig. 5.5. While it is evident that all profiles are similar, the detonation wave leading edge is shifted in each simulation, where a log-scale is used to emphasize the relatively small differences. A quantitative comparison between solutions would reveal the expected, first-order convergence due to the use of a shock capturing scheme [137]. Therefore, we evaluate convergence by inspecting the peak shock pressure and the final location of the shock front near $x = 0$, measured by position where the shock sensor is first activated. Both values are plotted with respect to the number of cells in Fig. 5.6. The final shock location initially asymptotes to a value of 5.5 mm upon successive grid refinement. However, continued refinement establishes a non-monotonic trend that brings the degree of convergence into question. The maximum pressure does not appear to converge, likely as

a result of the highly concentrated heat release noted in Fig. 5.4. The strong dependence of maximum pressure on mesh resolution indicates that a very fine mesh would be required to resolve the von Neumann post-shock conditions and ensuing thermally neutral induction region of the detonation front. While this analysis only considers a single Courant number, similar convergence is observed as the timestep is reduced.

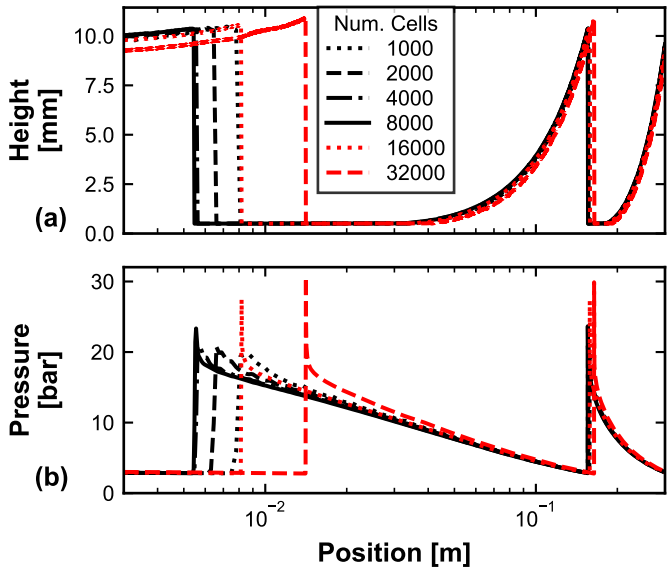

Figure 5.5. Profiles of (a) interface height and (b) product domain pressure for successive levels of mesh refinement.

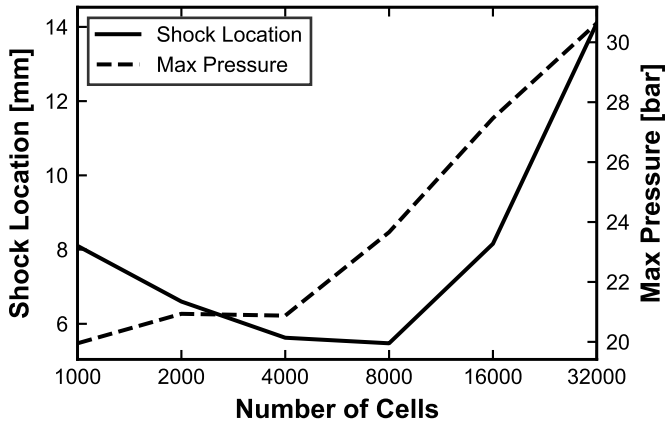

Figure 5.6. Final shock location after 0.2 ms and peak pressure at shock front with respect to mesh resolution.

5.3.4 Sensitivity of Domain Height

Since the total domain height, h_{dom}, does not evolve naturally as the model is advanced in time and is instead set as user-defined parameter, we conduct a sensitivity study to evaluate its effect on the solution. The study is conducted by continuing the simulation of Section 5.3.2 with the baseline domain height of 50 mm. The domain height is ramped continuously from 50 mm to a final height of 25 mm over 0.5 ms, as shown by the broken line of Fig. 5.7. Figure 5.7 further shows that the velocity of both waves, arbitrarily labeled 1 and 2, increases linearly with the linear reduction in domain height. From the initial steady state at a domain height of 50 mm to the later steady state at 25 mm, the wave velocity increases by 8% from 1980 m/s to 2140 m/s. The overlaid solution profiles from snapshots at t = 1.0 ms and t = 2.0 ms in Fig. 5.8 highlight significant changes in the waveform. The most important changes include the increased wave height, lower minimum temperatures in the product domain, increased peak pressure at the detonation front, a lower minimum pressure immediately ahead of the detonation wave, and significantly higher azimuthal velocities.

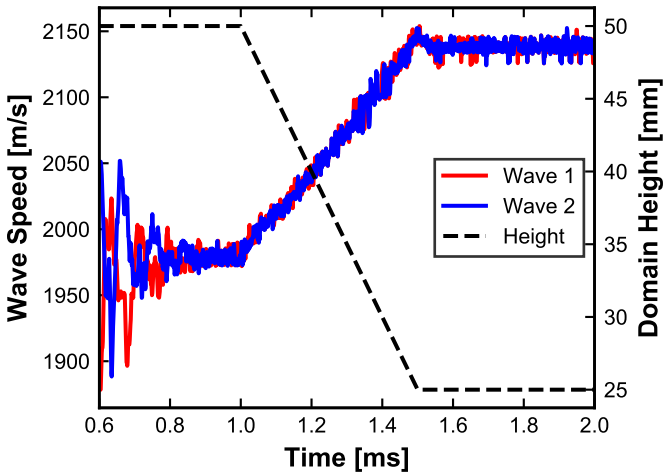

Figure 5.7. Wave velocities as domain height is reduced from 50 mm to 25 mm.

The changes in waveforms and detonation velocity highlight the important role of the total domain height within the model and in particular, its height relative to that of the wave. At the wave front, fuel and oxidizer are transferred from the reactant to product domains, where they are then converted to products in the detonation front. However, as

the product region is much taller than the reactant region at the wave front, a significant fraction of the mixture is still composed of products after the shock sensor has initiated the transfer. The residual products have two effects on the ensuing reactions. First, they increase the initial temperature behind the shock front, activating the kinetics and pushing the reactions to completion much faster than in a laminar detonation. This causes the extremely narrow heat release rate profile of Fig. 5.4e. Second, the heat release per unit mass behind the detonation front is much lower as the reactants have been diluted by the residual products. This reduces the strength of the detonation wave and is similar to the product gas recirculation mechanism of reducing wave strength [79], [90], [121], though by a non-physical mechanism. The reduced product gas fraction resulting from a shorter product region relative to the wave height then causes the observed increase in wave speed and pressure ratio across the detonation front.

In addition to affecting the fraction of residual products in the product region, changing the domain height affects the model in several other ways. The decreased domain height reduces the time required for the product domain to exhaust, resulting in the taller wavefront of Fig. 5.8a and lower pressure immediately ahead of the wave in Fig. 5.8c. As shown in Fig. 5.8d, the azimuthal velocity in the product domain also increases significantly, reaching a peak in excess of 2000 m/s. Further decreases in domain height were found to create instability in the solution profiles, as the azimuthal velocity continues to increase and results in the flow kinetic energy becoming comparable to the sensible energy.

The dependence on a user-specified domain height is a key limitation of the proposed quasi-1D modeling approach. As discussed in Section 5.1.2, a Neutral Mach Line is established at the top of the detonation wave front that isolates the detonation driving zone from downstream products. In our model, the product domain extends far beyond the axial location of the NML, producing the noted issue with residual product gases. Furthermore, it is not possible to simply set the total domain height to the detonation wave height, as it is not know a priori, and would produce the aforementioned instability as the domain height approaches the wave height.

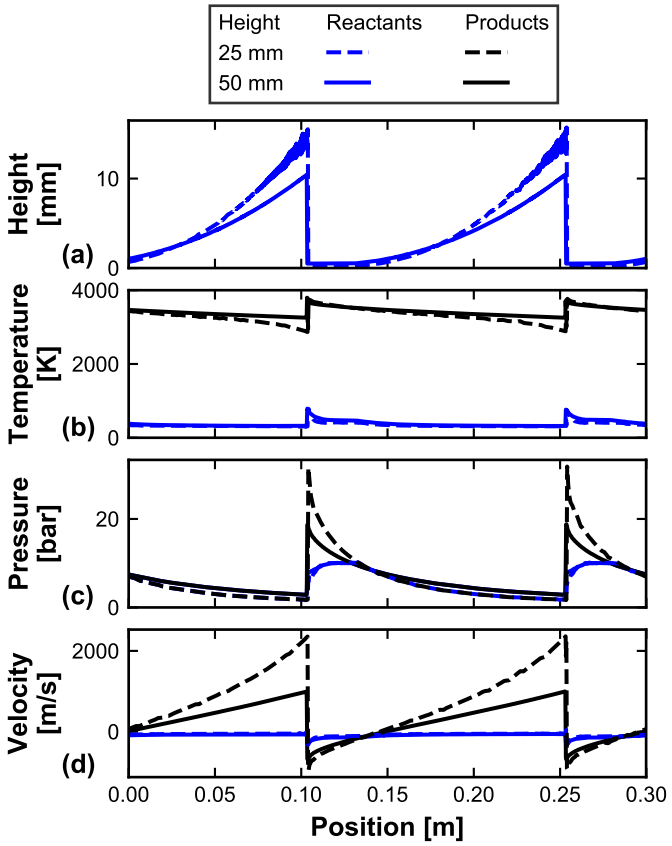

Figure 5.8. Instantaneous solution profiles of (a) interface height, (b) temperature, (c) pressure, and (d) velocity comparing domain heights of 50 mm and 25 mm.

5.4 Conclusions

Our development of a reduced-order model of RDE operation was motivated by current limitations in predicting the number and strength of detonation waves observed in experimental combustors. Critical review of the potential physical processes governing RDE mode selection and the assumptions and limitations of existing models informed the required physical fidelity and guided model development. In particular, we identified that prior models either lacked stratification between reactants and products or required a priori specification of the combustor wave mode, precluding the desired, natural evolution of limit-cycle wave dynamics. We therefore used the Euler equations as the foundation of our model to simulate the flow dynamics along the circumference of an RDE and developed a dynamic

interface model that separates reactant and product domains to address these limitations. Injection, exhaust, and reaction chemistry source terms completed the model specification to incorporate important RDE geometric parameters and define the operating condition.

Our reduced-order model is intended to bridge the divide between 1D and 2D models of RDE operation while addressing disadvantages of each. Fully 1D models correspond to the limit of perfect mixing between reactants and products [11], such that the detonation propagates into its own tail, where residual products reduce the wave strength. Reactant-product stratification is then required for accurate modeling of the detonation wave strength (speed, pressure amplitude), as it ensures that the wave propagates into the correct mixture and thereby produces the correct profiles of heat release and flow expansion that drive its continued propagation. This unique feature of the RDE flow field is therefore expected to be critical for the prediction of RDE wave modes, as the wave speed sets the most important timescale of RDE operation, the wave arrival frequency. This timescale subsequently determines the time available for mixing between fuel and oxidizer, product gas recirculation, and potential autoignition in the reactant region. While each of these processes further influence the wave strength [90], [121], autoignition could result in nucleation of a new wave if the reaction front is able to steepen and transition from a deflagration to detonation [138]. These factors delineate our motivation for including separate reactant and product domains, despite the increased model complexity.

In comparison to 2D simulations that unwrap the annular geometry of RDEs, our model is designed to reduce the computational cost of simulations while retaining the key flow physics described above. In addition, the quasi-1D format permits explicit modeling approaches to bypass the limitations associated with 2D simulations discussed in Section 5.1.2. As noted, reactant injection generates intense turbulence that mixes fuel and oxidizer and recirculates detonation products into the reactant region in a process that is fundamentally 3D. Even with novel boundary conditions that emulate non-premixed injection, 2D simulations will be unable to match the mixing characteristics of real injection schemes. Instead, our quasi-1D modeling approach can include these processes via source terms that explicitly vary the rate or timescale of reactant mixing or product gas recirculation. Explicit rate parameters can

then be tuned based on experimental measurements of the modeled, unit processes or via interrogation of 3D simulations.

After developing the model format, initial tests demonstrated that the model was capable of progressing through a startup transient and forming propagating detonation waves for a baseline RDE configuration. Inspection of limit-cycle solution profiles demonstrated that the model produces the expected sequence of shock-induced combustion followed by exhaustion of products and injection of fresh reactants, producing modulation of the reactant interface surface. While a mesh refinement study was unable to demonstrate quantitative convergence in terms of the location or peak pressure of the leading shock, the solution profiles had qualitatively converged. A sensitivity study dynamically varied the total domain height to investigate its effect on the model, as it does not evolve as part of the solution. Comparison of wave speeds and solution profiles revealed significant differences due to simultaneous reduction of residual detonation products in the product domain and of the product domain exhaust timescale as the domain height was decreased.

While the presented model addresses a principal limitation of existing reduced-order models for RDE wave dynamics and mode selection, several aspects restrain the model from the desired level of general applicability. The most important factor stems from the discussed dependence of wave strength on the domain height. The prescribed domain height causes the model to violate the RDE flowfield physics, as it prevents formation of a Neutral Mach Line to isolate the detonation driving zone from downstream products. The current model formulation also does not include the important physics of product gas recirculation. As discussed in Section 5.1.1, turbulent mixing of combustion products across the contact surface and into the fresh reactants will influence the detonation strength. Furthermore, this mixing can lead to incipient autoignition in the reactant mixture and potentially induce a deflagration to detonation transition that produces an additional detonation wave. Other limitations are the result of intentional simplifications to the model, particularly the source terms. The current format assumes premixed reactants, while nearly all RDE experiments use a non-premixed injection scheme. The injector flow model assumes that the injector flowrate responds instantaneously to the downstream pressure. While a reasonable approximation for the high-loss injectors typical of current experiments, flow inertia will become

important for injector designs with low pressure drop required to realize the thermodynamic advantages of RDEs. These same conditions will also potentially allow backflow of combustion products into the injector as the detonation wave passes over a given injector site. Finally, the quasi-1D model format assumes that the detonation dynamics can be sufficiently described by a 1D, laminar detonation model. Instead, the structure of gaseous detonations is always fully 3D, where the additional dimensions and ensuing turbulence significantly modify the propagation limits [139].

The limitations of our model described above naturally correspond to potential areas for future development. In particular, the key issues involved with the fixed domain height provide a clear starting point for future attempts to improve the model. Allowing the total domain height to vary with position is the most promising avenue to address the issues. However, physically-derived rules for evolving the height of the product domain are less clear for this modeling approach. In comparison, exhaust gas recirculation into the reactant domain is relatively straightforward to implement via a direct transfer using the model source terms. The rate of product gas transfer could then be set by a tuned parameter, permitting variation to match experimental observations of global wave dynamics, direct experimental measurements using laser-based diagnostics [90], or mixing characteristics derived from detailed simulations. These two modifications should then permit a robust comparison to well-characterized RDE experiments.

Further developments could then modify source terms to address the noted model simplifications. A mixing model could be implemented to emulate non-premixed reactant injection, possibly as part of the kinetic mechanism. Similar to the proposed modeling approach for product gas recirculation, direct modification of reactant mixing rates or timescales would be more insightful than a mechanistic approach. A direct approach produces readily interpretable, user-tuned parameters that enable comparison with advanced experimental measurements or post-processing of detailed simulations. An injector backflow model would require tracking the total mass of products that have passed upstream of the injector throat and then ejecting them before a given injector site begins to introduce fresh reactants. Finally, the injector dynamic response to passing detonation waves could be modeled using an empirical response function akin to that used in the study of combustion stability [108].

Depending on the level of desired fidelity, the response function could be fit to dedicated experiments or simulations.

The reduced-order model we have developed shows significant promise for helping to elucidate the factors governing RDE wave dynamics and hence combustor operability. While additional work is required to achieve the objective of a robust, generally applicable modeling tool, the identified areas for further development would enable the model to help identify an avenue towards delivering the long-sought total pressure gain.

6. CONCLUSIONS

This study has sought to advance understanding of rotating detonation engine operation and performance at conditions representative of gas turbine combined cycle power plants. Such conditions are not conducive to RDE operation due to the low relative detonability of natural gas in air, the reactant combination of choice for the application. However, pressure-gain combustion could increase the cycle thermodynamic efficiency by 3-5%, providing significant incentive towards developing and deploying RDEs in this application. To this end, a combustor and associated test facility were developed to investigate the unique challenges associated with RDEs in terrestrial power generation systems. The combustor design enabled operation with natural gas and preheated air across a broad range of flow conditions and with chamber pressures up to 2 MPa. The experiments have provided unique insight into the operation of RDEs with less-detonable reactants, while complementary modeling helped to generalize the observations.

The requirement of operating with natural gas-air reactants drove primary combustor design, where the detonation cell size at the target operating conditions was estimated and used to set the scale of the RDE. Two injector concepts, denoted "axial" and "sting," were then developed to permit investigation of the sensitivity of detonation wave dynamics and combustor operation to the mixing field. Multiple backpressure nozzles were used to further probe the effect of the chamber bulk flowfield. Detonation wave dynamics were characterized using high-frequency pressure measurements and imaging of the combustion annulus for direct visualization. Combustor performance was assessed using thrust measurements.

The natural gas-air RDE was tested across a range of conditions, in a parametric survey to characterize sensitivity of combustor operability and performance to the injector design, mass flux of reactants, oxygen mass fraction in the oxidizer flow, oxidizer temperature, equivalence ratio, and mass fraction of hydrogen in the fuel. Two metrics were developed to characterize combustor operation across the wide range of test conditions and observed operating modes. The strength of propagating detonation waves, or any other chamber dynamics that developed, was evaluated using the amplitude of measured pressure oscillations. The stability of a particular operating mode was characterized using a novel metric called

the power fraction, which computes the fraction of spectral power associated with the primary chamber dynamics in a given signal. Tests on synthetic data demonstrated that the power fraction was insensitive to random noise, but acutely sensitive to waveform dephasing characteristic of marginal combustor operation. Sensitivity of RDE performance to hardware configuration and operating condition was evaluated using the Equivalent Available Pressure methodology, which computes the hypothetical, steady total pressure, the EAP, required to match the measured thrust. This pressure can then be compared to the reactant manifold pressure to assess the delivered net pressure gain.

Across the range of hardware configurations and operating conditions tested in the parametric survey, chamber wave dynamics were typically characterized by multiple, counter-rotating detonation wave heads. However, a limited range of lean conditions using the "sting" injector design and backpressure nozzle with the largest throat exhibited sustained operation with a single detonation wave. Global evaluation of trends in wave strength and stability across all tested conditions revealed a minimum observed wave velocity of approximately 50% of the mixture Chapman-Jouguet detonation velocity, which may correspond to the Chapman-Jouguet deflagration velocity. Global trends in RDE operability and performance indicated that the detonation cell size is an at-best approximate scaling parameter for RDE design with less-detonable reactants. Detonative combustor operation with reasonable performance was observed once the cell size decreased to a similar scale as the combustion annulus gap, but further decreases failed to guarantee high-order detonation waves or increased performance. The reduced importance of the cell size for less-detonable reactants is unsurprising, as the cellular structure of such reactants exhibits a broad range of lengthscales and because the flow and boundary conditions of RDEs are far removed from the canonical setting of cell size measurements.

Independent variation of operating parameters revealed that RDE operability was strongly sensitive to the reactant mixture reaction kinetics and mixing, while combustor performance was only weakly sensitive to the flow conditions. Elevated mean chamber pressures through increased reactant mass flux appeared to suppress the detonation fronts, but had no effect on the delivered pressure gain. Parametric variation of the oxidizer oxygen mass fraction and inlet air temperature demonstrated that the "axial" injector required sensitization of

the reactant mixture kinetics to achieve stable detonations, while the "sting" injector did not. Furthermore, the "sting" injector with the most open backpressure nozzle produced stronger detonations at fuel-lean conditions, while the "axial" injector quickly reverted to deflagrative operation as the equivalence ratio deviated from stoichiometric. These trends collectively suggested that the "sting" injector better mixed the reactants, as any method of sensitizing the mixture kinetics produced deflagration. Variations in equivalence ratio or oxygen mass fraction had minimal effect on performance for either injector configuration. Instead, the injector and backpressure nozzle configuration were found to have the greatest impact on the delivered net pressure gain. However, all tested conditions were observed to produce a stagnation pressure loss relative to the reactant manifold.

While the observed trends in RDE operability are likely the result of the details of turbulent mixing, reaction chemistry, and the injector dynamic response and are hence beyond simple explanation, thermodynamic modeling was applied to assist interpretation of the observed performance trends. A simple performance model was developed to predict the pressure gain, or loss, at conditions matched to the experiment. Comparison of results across the range of conditions tested in the parametric survey revealed that the "sting" injector better followed the trends predicted by the model, supporting the observation that the operation and performance of the "axial" injector is likely limited by reactant mixing. Though useful for informing the observed experimental performance trends, applying the model to a generic RDE provided significant insight into RDE performance measurement and the design of high-performance combustors. The analysis first highlighted the necessity of normalizing any RDE performance metric by the driving system potential, typically the reactant manifold pressure. Parametric variation of the model parameters further demonstrated that the area ratio between the combustion chamber exit and inlet is the most important parameter influencing RDE pressure gain, consistent with the experimental observation of the performance sensitivity to the backpressure nozzle. The thermodynamic performance model was applied to identify the range of area ratios that would produce a pressure gain for several different reactant combinations.

A pair of test conditions using the "sting" injector that alternately exhibited a single and counter-rotating wave mode were then selected for application of high-speed particle image

velocimetry at the RDE exit plane to characterize the exhaust flow for contrasting wave dynamics. In conjunction with high-frequency pressure and aft-end imaging, the velocity measurements were phase averaged with respect to the instantaneous detonation front location. The single wave case exhibited the canonical, self-similar RDE exhaust flow structures, with an oblique shock wave sweeping through the products and into the exhaust. In contrast, the counter-rotating detonation fronts of the second case produced shock interactions that generated destructive interference in the azimuthal velocity component, but resulted in an axial velocity component independent of wave location. A new method for experimentally quantifying RDE performance was then developed to remove conservative assumptions involved in the EAP method used throughout the rest of study. The performance analysis computes a hypothetical, steady stagnation pressure and temperature by leveraging the phase resolved velocity profiles to balance the global conservation of mass and momentum against the measured reactant flowrate and thrust.

The final component of the study developed a reduced-order model for investigating RDE operability. Circumferential detonation wave dynamics are simulated using the Euler equations, while axial stratification between reactants and products is captured using a dynamic interface between two domains that become coupled at the detonation front. Additional source terms govern reaction chemistry, injection of reactants, and exhaust of products. The model format permits natural evolution of the diverse range of wave modes observed in RDEs while maintaining sufficient physical fidelity to facilitate direct comparisons with experiments. Preliminary verification and sensitivity studies are presented, establishing that the model is able to naturally develop wave dynamics similar to those observed in RDEs without a priori specification of the operating mode. Areas of further development so that the model can be applied for comparison with experiments, design exploration, and optimization are identified.

In summary, the key contributions of this thesis are as follows. First, a natural gas-air RDE was developed and used to demonstrate operation at a wide range of flow conditions, providing insight into the unique challenges of RDE operation with less-detonable reactants. Second, it has advanced fundamental understanding of RDE performance and provided the necessary tools to experimentally demonstrate a pressure gain. The identified

relationship between combustor performance and the outlet-to-inlet area ratio provides a quantitative design parameter to guide development of a RDE for this purpose, while the novel method of performance quantification using exhaust plane velocity measurements provides a more accurate method for its experimental verification. In addition, the need to normalize RDE performance by the driving system potential further provides a necessary condition for demonstrating the cycle thermodynamic advantages. Finally, the reduced-order operability model is an initial step towards developing the understanding of RDE mode selection required to facilitate development of a combustor capable of operating at the low-loss conditions necessary to achieve a pressure gain.

REFERENCES

[1] National Academies of Science, Engineering, and Medicine, *Advanced Technologies for Gas Turbines*. National Academies Press, Mar. 2020. DOI: 10.17226/25630.

[2] J. H. Lee, *The Detonation Phenomenon*, 1st. Cambridge: Cambridge University Press, 2008, ISBN: 9780521897235. DOI: 10.1017/CBO9780511754708.

[3] J. Shepherd and E. Wintenberger, "Thermodynamic analysis of combustion processes for propulsion systems," 42nd AIAA Aerospace Sciences Meeting and Exhibit, AIAA 2004-1033, 2004. DOI: 10.2514/6.2004-1033.

[4] P. Akbari and M. R. Nalim, "Review of recent developments in wave rotor combustion technology," *Journal of Propulsion and Power*, vol. 25, no. 4, pp. 833–844, Jul. 2009. DOI: 10.2514/1.34081.

[5] G. Roy, S. Frolov, A. Borisov, and D. Netzer, "Pulse detonation propulsion: Challenges, current status, and future perspective," *Progress in Energy and Combustion Science*, vol. 30, no. 6, pp. 545–672, Jan. 2004. DOI: 10.1016/j.pecs.2004.05.001.

[6] P. Wolanski, "Detonative propulsion," *Proc. Combust. Inst.*, vol. 34, pp. 125–158, 2013, ISSN: 15407489. DOI: 10.1016/j.proci.2012.10.005.

[7] F. A. Bykovskii, S. A. Zhdan, and E. F. Vedernikov, "Continuous Spin Detonations," *Journal of Propulsion and Power*, vol. 22, no. 6, pp. 1204–1216, 2006, ISSN: 0748-4658. DOI: 10.2514/1.17656.

[8] F. K. Lu and E. M. Braun, "Rotating Detonation Wave Propulsion: Experimental Challenges, Modeling, and Engine Concepts," *Journal of Propulsion and Power*, vol. 30, no. 5, pp. 1125–1142, 2014, ISSN: 0748-4658. DOI: 10.2514/1.b34802.

[9] V. Anand and E. Gutmark, "Rotating detonation combustors and their similarities to rocket instabilities," *Progress in Energy and Combustion Science*, vol. 73, pp. 182–234, 2019, ISSN: 0360-1285. DOI: https://doi.org/10.1016/j.pecs.2019.04.001.

[10] B. Voitsekhovskii, "Stationary spin detonation," *Soviet Journal of Applied Mechanics and Technical Physics*, vol. 3, pp. 157–164, 1960.

[11] J. Nicholls and R. Cullen, *The Feasibility of a Rotating Detonation Wave Rocket Motor*, The University of Michigan RPL-TDR-64-113, 1964.

[12] I. V. Walters, C. L. Journell, A. Lemcherfi, R. M. Gejji, S. D. Heister, and C. D. Slabaugh, "Operability of a natural gas–air rotating detonation engine," *Journal of Propulsion and Power*, vol. 36, no. 3, pp. 453–464, 2020. DOI: 10.2514/1.B37735.

[13] D. E. Paxson and T. Kaemming, "Influence of Unsteadiness on the Analysis of Pressure Gain Combustion Devices," *Journal of Propulsion and Power*, vol. 30, no. 2, pp. 377–383, 2014, ISSN: 0748-4658. DOI: 10.2514/1.b34913.

[14] C. A. Nordeen, "Thermodynamics of a Rotating Detonation Engine," Doctoral Dissertation, University of Connecticut, Storrs, CT, 2013.

[15] B. A. Rankin, D. R. Richardson, A. W. Caswell, A. G. Naples, J. L. Hoke, and F. R. Schauer, "Chemiluminescence imaging of an optically accessible non-premixed rotating detonation engine," *Combust. Flame*, vol. 176, pp. 12–22, 2017, ISSN: 15562921. DOI: 10.1016/j.combustflame.2016.09.020.

[16] D. P. Stechmann, "Experimental Study of High-Pressure Rotating Detonation Combustion in Rocket Environments," Doctoral Dissertation, Purdue University, West Lafayette, IN, 2017.

[17] K. Kailasanath and D. A. Schwer, "High-fidelity simulations of pressure-gain combustion devices based on detonations," *Journal of Propulsion and Power*, vol. 33, no. 1, pp. 153–162, 2017, ISSN: 0748-4658. DOI: 10.2514/1.B36169.

[18] M. D. Bohon, R. Bluemner, C. O. Paschereit, and E. J. Gutmark, "High-speed imaging of wave modes in an RDC," *Experimental Thermal and Fluid Science*, vol. 102, no. August 2018, pp. 28–37, 2019, ISSN: 08941777. DOI: 10.1016/j.expthermflusci.2018.10.031.

[19] M. L. Fotia, J. Hoke, and F. Schauer, "Experimental performance scaling of rotating detonation engines operated on gaseous fuels," *Journal of Propulsion and Power*, vol. 33, no. 5, pp. 1187–1196, Sep. 2017. DOI: 10.2514/1.b36213.

[20] J. W. Bennewitz, B. R. Bigler, J. J. Pilgram, and W. A. Hargus, Jr., "Modal Transitions in Rotating Detonation Rocket Engines," *International Journal of Energetic Materials and Chemical Propulsion*, vol. 18, no. 2, pp. 91–109, 2019, ISSN: 2150-766X. DOI: 10.1615/intjenergeticmaterialschemprop.2019027880.

[21] J. Tobias, D. Depperschmidt, C. Welch, R. Miller, M. Uddi, A. K. Agrawal, and R. Daniel, "Oh* chemiluminescence imaging of the combustion products from a methane-fueled rotating detonation engine," *Journal of Engineering for Gas Turbines and Power*, vol. 141, no. 2, Oct. 2018. DOI: 10.1115/1.4041143.

[22] F. A. Bykovskii, S. A. Zhdan, E. F. Vedernikov, and A. N. Samsonov, "Scaling factor in continuous spin detonation of syngas–air mixtures," *Combustion, Explosion, and Shock Waves*, vol. 53, no. 2, pp. 187–198, Mar. 2017. DOI: 10.1134/s0010508217020095.

[23] F. A. Bykovskii, S. A. Zhdan, and E. F. Vedernikov, "Continuous Detonation of Methane/Hydrogen–Air Mixtures in an Annular Cylindrical Combustor," *Combustion, Explosion, and Shock Waves*, vol. 54, no. 4, pp. 472–481, 2018, ISSN: 0010-5082. DOI: 10.1134/s0010508218040111.

[24] F. A. Bykovskii and S. A. Zhdan, "Continuous spin detonation of poorly detonable fuel-air mixtures in annular combustors," *Journal of Physics: Conference Series*, vol. 899, p. 042 002, Sep. 2017. DOI: 10.1088/1742-6596/899/4/042002.

[25] A. Roy, D. H. Ferguson, T. Sidwell, B. O'Meara, P. Strakey, C. Bedick, and A. Sisler, "Experimental study of rotating detonation combustor performance under preheat and back pressure operation," 55th AIAA Aerospace Sciences Meeting, AIAA 2017-1065, Jan. 2017. DOI: 10.2514/6.2017-1065.

[26] A. Roy, D. Ferguson, T. Sidwell, and P. Strakey, "Characteristics of a non-premixed rotating detonation combustor using natural gas-hydrogen blend at elevated air-preheat temperature and backpressure," in *Volume 8A: Heat Transfer and Thermal Engineering*, American Society of Mechanical Engineers, Nov. 2018. DOI: 10.1115/imece2018-88569. [Online]. Available: https://doi.org/10.1115/imece2018-88569.

[27] S. E. Meyer, S. D. Heister, C. Slabaugh, R. P. Lucht, A. Pratt, R. M. Gejji, M. Bedard, and A. Lemcherfi, "Design and Development of the High Pressure Combustion Laboratory at Purdue University," 53rd AIAA/SAE/ASEE Joint Propulsion Conference, AIAA 2017-4965, 2017. DOI: 10.2514/6.2017-4965.

[28] C. D. Slabaugh, A. C. Pratt, R. P. Lucht, S. E. Meyer, M. Benjamin, K. Lyle, and M. Kelsey, "The development of an optically accessible, high-power combustion test rig," *Review of Scientific Instruments*, vol. 85, no. 3, p. 035 105, 2014. DOI: 10.1063/1.4867084.

[29] Vectern Energy Delivery, *Tuscola East Mainline PEPL Daily Average Gas Quality Info*, 2017. [Online]. Available: https://peplmessenger.energytransfer.com.

[30] International Standards Organization, *Measurement of Gas Flow by Means of Critical Flow Venturi Nozzles*, Brussels, 2005.

[31] E. Lemmon, *Nist reference fluid thermodynamic and transport properties database: Version 9.0, nist standard reference database 23*, en, 1989. DOI: 10.18434/T4JS3C.

[32] S. Kline and F. McClintock, "Describing Uncertainties in Single-Sample Experiments," *Mechanical Engineering*, vol. 75, no. January, pp. 3–8, 1953.

[33] S. J. Miller, "Design and Testing of an H2/O2 Predetonator for a Simulated Rotating Detonation Engine Channel," Masters Thesis, Air Force Institute of Technology, Dayton, OH, 2013, p. 106.

[34] A. St. George, R. Driscoll, V. Anand, and E. Gutmark, "On the existence and multiplicity of rotating detonations," *Proc. Combust. Inst.*, vol. 36, no. 2, pp. 2691–2698, 2017. DOI: 10.1016/j.proci.2016.06.132.

[35] M. I. RADULESCU, G. J. SHARPE, C. K. LAW, and J. H. S. LEE, "The hydrodynamic structure of unstable cellular detonations," *Journal of Fluid Mechanics*, vol. 580, pp. 31–81, May 2007. DOI: 10.1017/s0022112007005046.

[36] M. Kaneshige and J. Shepherd, *Detonation Database*, 1997.

[37] C. A. Stevens, J. Hoke, and F. Schauer, "Propane-air cell size correlation to temperature and pressure," 54th AIAA Aerospace Sciences Meeting, AIAA 2016-1400, 2016. DOI: 10.2514/6.2016-1400.

[38] P. A. Bauer, H. N. Presles, O. Heuze, and C. Brochet, "Measurement of cell lengths in the detonation front of hydrocarbon oxygen and nitrogen mixtures at elevated initial pressures," *Combustion and Flame*, vol. 64, no. 1, pp. 113–123, 1986, ISSN: 00102180. DOI: 10.1016/0010-2180(86)90102-1.

[39] S. Siwiec and P. Wolańskl, "Detonation cell structure in CH4-air mixture at high pressure," *Archivum Combustionis*, vol. 4, no. 3, pp. 249–252, 1984.

[40] "Chemical kinetics of propane oxidation in gaseous detonations," in *Dynamics of Shock Waves, Explosions, and Detonations*, American Institute of Aeronautics and Astronautics, Jan. 1985, pp. 151–174. DOI: 10.2514/5.9781600865695.0151.0174. [Online]. Available: https://doi.org/10.2514/5.9781600865695.0151.0174.

[41] "Chemical kinetics in LNG detonations," in *Gasdynamics of Detonations and Explosions*, American Institute of Aeronautics and Astronautics, Jan. 1981, pp. 193–206. DOI: 10.2514/5.9781600865497.0193.0206. [Online]. Available: https://doi.org/10.2514/5.9781600865497.0193.0206.

[42] V. R. Katta, K. Y. Cho, J. L. Hoke, J. R. Codoni, F. R. Schauer, and W. M. Roquemore, "Effect of increasing channel width on the structure of rotating detonation wave," *Proceedings of the Combustion Institute*, vol. 37, no. 3, pp. 3575–3583, 2019. DOI: 10.1016/j.proci.2018.05.072.

[43] S. Frolov, V. Aksenov, V. Ivanov, and I. Shamshin, "Large-scale hydrogen–air continuous detonation combustor," *International Journal of Hydrogen Energy*, vol. 40, no. 3, pp. 1616–1623, Jan. 2015. DOI: 10.1016/j.ijhydene.2014.11.112.

[44] J. Sun, J. Zhou, S. Liu, Z. Lin, and W. Lin, "Effects of air injection throat width on a non-premixed rotating detonation engine," *Acta Astronautica*, vol. 159, pp. 189–198, Jun. 2019. DOI: 10.1016/j.actaastro.2019.03.067.

[45] I. V. Walters, C. Journell, A. Lemcherfi, R. Gejji, S. D. Heister, and C. D. Slabaugh, "Experimental investigation of a piloted, natural gas-air rotating detonation wave combustor," 2018 Joint Propulsion Conference, AIAA 2018-4782, 2018. DOI: 10.2514/6.2018-4782.

[46] F. A. Bykovskii, S. A. Zhdan, E. F. Vedernikov, A. N. Samsonov, A. I. Sychev, and A. E. Tarnaikin, "Pressure measurement by fast-response piezo-electric sensors during continuous spin detonation in the combustor," *Combustion, Explosion, and Shock Waves*, vol. 53, no. 1, pp. 65–73, 2017, ISSN: 0010-5082. DOI: 10.1134/S0010508217010105.

[47] R. M. Gejji, I. V. Walters, S. Beard, A. Lemcherfi, S. V. Sardeshmukh, S. D. Heister, and C. D. Slabaugh, "Transducer Installation Effects on Pressure Measurements in PGC Devices," 2018 AIAA Aerospace Sciences Meeting, AIAA 2018-0158, 2018. DOI: 10.2514/6.2018-0158.

[48] J. W. Bennewitz, B. R. Bigler, S. A. Schumaker, and W. A. Hargus, "Automated image processing method to quantify rotating detonation wave behavior," *Review of Scientific Instruments*, vol. 90, no. 6, p. 065 106, 2019. DOI: 10.1063/1.5067256.

[49] I. V. Walters, C. L. Journell, A. Lemcherfi, R. Gejji, S. D. Heister, and C. D. Slabaugh, "Parametric survey of a natural gas-air rotating detonation engine at elevated pressure," AIAA Scitech 2019 Forum, AIAA 2019-1510, 2019. DOI: 10.2514/6.2019-1510.

[50] K. Schwinn, R. Gejji, B. Kan, S. Sardeshmukh, S. Heister, and C. D. Slabaugh, "Self-sustained, high-frequency detonation wave generation in a semi-bounded channel," *Combustion and Flame*, vol. 193, pp. 384–396, Jul. 2018. DOI: 10.1016/j.combustflame.2018.03.022.

[51] S. Pincus, "Approximate entropy (ApEn) as a complexity measure," *Chaos: An Interdisciplinary Journal of Nonlinear Science*, vol. 5, no. 1, pp. 110–117, Mar. 1995. DOI: 10.1063/1.166092.

[52] R. Chue, J. Clarke, and J. H. Lee, "Chapman-Jouguet Deflagrations," *Proceedings: Mathematical and Physical Sciences*, vol. 441, no. 1913, pp. 607–623, 1993. DOI: 10.1098/rspa.1993.0082.

[53] D. E. Paxson and D. A. Schwer, "Operational stability limits in rotating detonation engine numerical simulations," AIAA Scitech 2019 Forum, AIAA 2019-0748, 2019. DOI: 10.2514/6.2019-0748.

[54] D. P. Stechmann, S. Sardeshmukh, S. D. Heister, and K. Mikoshiba, "Role of ignition delay in rotating detonation engine performance and operability," *Journal of Propulsion and Power*, vol. 35, no. 1, pp. 125–140, Jan. 2019. DOI: 10.2514/1.b37117.

[55] T. Kaemming, M. L. Fotia, J. Hoke, and F. Schauer, "Thermodynamic Modeling of a Rotating Detonation Engine Through a Reduced-Order Approach," *Journal of Propulsion and Power*, vol. 33, no. 5, pp. 1170–1178, 2017, ISSN: 0748-4658. DOI: 10.2514/1.b36237.

[56] I. V. Walters, A. Lemcherfi, R. M. Gejji, S. D. Heister, and C. D. Slabaugh, "Performance characterization of a natural gas-air rotating detonation engine," *Journal of Propulsion and Power*, vol. 37, no. 2, pp. 292–304, Mar. 2021. DOI: 10.2514/1.b38087.

[57] F. Chacon, A. Feleo, and M. Gamba, "Impact of Inlet Area Ratio on the Operation of an Axial Air Inlet Configuration Rotating Detonation Combustor," AIAA Propulsion and Energy 2019 Forum, AIAA 2019-4450, 2019. DOI: 10.2514/6.2019-4450.

[58] A. Roy, C. R. Bedick, D. H. Ferguson, T. Sidwell, and P. A. Strakey, "Investigating Instabilities in a Rotating Detonation Combustor Operating With Natural Gas–Hydrogen Fuel Blend—Effect of Air Preheat and Annulus Width," *Journal of Engineering for Gas Turbines and Power*, vol. 141, no. 11, Oct. 2019, 111017, ISSN: 0742-4795. DOI: 10.1115/1.4044980.

[59] C. L. Journell, R. M. Gejji, I. V. Walters, A. I. Lemcherfi, C. D. Slabaugh, and J. B. Stout, "High-speed diagnostics in a natural gas–air rotating detonation engine," *Journal of Propulsion and Power*, vol. 36, no. 4, pp. 498–507, 2020. DOI: 10.2514/1.B37740.

[60] W. Y. Peng, S. J. Cassady, C. L. Strand, C. S. Goldenstein, R. M. Spearrin, C. M. Brophy, J. B. Jeffries, and R. K. Hanson, "Single-ended mid-infrared laser-absorption sensor for time-resolved measurements of water concentration and temperature within the annulus of a rotating detonation engine," *Proc. Combust. Inst.*, vol. 37, no. 2, pp. 1435–1443, 2019, ISSN: 1540-7489. DOI: https://doi.org/10.1016/j.proci.2018.05.021.

[61] T. A. Kaemming and D. E. Paxson, "Determining the Pressure Gain of Pressure Gain Combustion," 2018 Joint Propulsion Conference, AIAA 2018-4567, 2018. DOI: 10.2514/6.2018-4567.

[62] E. Bach, P. Stathopoulos, C. O. Paschereit, and M. D. Bohon, "Performance analysis of a rotating detonation combustor based on stagnation pressure measurements," *Combust. Flame*, vol. 217, pp. 21–36, 2020, ISSN: 0010-2180. DOI: https://doi.org/10.1016/j.combustflame.2020.03.017.

[63] J. A. TenEyck, "Determination of Effective Available Pressure of a Rotating Detonation Engine," Masters Thesis, Naval Postgraduate School, Monterey, CA, 2019.

[64] J. B. Stout and A. Baratta, "Demonstrated low loss and low equivalence ratio operation of a rotating detonation engine for power generation," AIAA Scitech 2020 Forum, AIAA 2020-1173, 2020. DOI: 10.2514/6.2020-1173.

[65] D. P. Stechmann, S. D. Heister, and A. J. Harroun, "Rotating Detonation Engine Performance Model for Rocket Applications," *Journal of Spacecraft and Rockets*, vol. 56, no. 3, pp. 887–898, 2019. DOI: 10.2514/1.a34313.

[66] C. A. Nordeen, D. Schwer, F. Schauer, J. Hoke, T. Barber, and B. Cetegen, "Thermodynamic model of a rotating detonation engine," *Combustion, Explosion, and Shock Waves*, vol. 50, no. 5, pp. 568–577, Sep. 2014. DOI: 10.1134/s0010508214050128.

[67] J. E. Shepherd and J. Kasahara, *Analytical Models for the Thrust of a Rotating Detonation Engine Jiro Kasahara Professor of Aerospace Engineering California Institute of Technology*, 2017. DOI: 10.7907/DNVT-PY80.

[68] E. M. Braun, F. K. Lu, D. R. Wilson, and J. A. Camberos, "Airbreathing Rotating Detonation Wave Engine Cycle Analysis," *Aerospace Science and Technology*, vol. 27, pp. 201–208, 2013. DOI: 10.1016/j.ast.2012.08.010.

[69] *Measurement of Gas Flow by Means of Critical Flow Venturis and Critical Flow Nozzles*, ASME MFC-7-2016, American Society of Mechanical Engineers, New York, August, 2016.

[70] *Evaluation of measurement data - Guide to the expression of uncertainty in measurement*, JCGM 100:2008, Joint Committee for Guides in Metrology, September, 2008.

[71] A. J. Harroun, "Investigation of Nozzle Performance for Rotating Detonation Rocket Engines," Masters Thesis, Purdue University, West Lafayette, IN, 2019.

[72] D. Schwer and K. Kailasanath, "Fluid dynamics of rotating detonation engines with hydrogen and hydrocarbon fuels," *Proceedings of the Combustion Institute*, vol. 34, no. 2, pp. 1991–1998, Jan. 2013. DOI: 10.1016/j.proci.2012.05.046.

[73] S. Gordon and B. J. McBride, *Computer Program for Calculation of Complex Chemical Equilibrium Compositions and Applications*, NASA Reference Publication 1311, NASA, Cleveland, OH, 1994.

[74] R. C. Kimura, E. J. Paulson, and V. Sankaran, "A Parametric Analysis of a Rotating Detonation Rocket Engine Cycle using CEA," AIAA Scitech 2019 Forum, AIAA 2019-1741, 2019. DOI: 10.2514/6.2019-1741.

[75] J. Sosa, R. Burke, K. A. Ahmed, D. J. Micka, J. W. Bennewitz, S. A. Danczyk, E. J. Paulson, and W. A. Hargus, "Experimental evidence of h2/o2 propellants powered rotating detonation waves," *Combustion and Flame*, vol. 214, pp. 136–138, Apr. 2020. DOI: 10.1016/j.combustflame.2019.12.031.

[76] V. Anand, A. S. George, R. Driscoll, and E. Gutmark, "Investigation of rotating detonation combustor operation with h 2 -air mixtures," *International Journal of Hydrogen Energy*, vol. 41, no. 2, pp. 1281–1292, Jan. 2016. DOI: 10.1016/j.ijhydene.2015.11.041.

[77] O. Lammel, H. Schütz, G. Schmitz, R. Lückerath, M. Stöhr, B. Noll, M. Aigner, M. Hase, and W. Krebs, "FLOX® Combustion at High Power Density and High Flame Temperatures," *Journal of Engineering for Gas Turbines and Power*, vol. 132, no. 12, p. 121 503, 2010, ISSN: 07424795. DOI: 10.1115/1.4001825.

[78] I. V. Walters, R. M. Gejji, S. D. Heister, and C. D. Slabaugh, "Flow and performance analysis of a natural gas-air rotating detonation engine with high-speed velocimetry," *Combustion and Flame*, 2021. DOI: 10.1016/j.combustflame.2021.111549.

[79] B. D. Edwards, "Maintained detonation waves in an annular channel: A hypothesis which provides the link between classical acoustic combustion instability and detonation waves," *Symp. (Int.) Combust.*, vol. 16, no. 1, pp. 1611–1618, 1977, ISSN: 0082-0784. DOI: https://doi.org/10.1016/S0082-0784(77)80440-2.

[80] R. Bluemner, M. Bohon, C. Paschereit, and E. Gutmark, "Counter-rotating wave mode transition dynamics in an RDC," *International Journal of Hydrogen Energy*, vol. 44, no. 14, pp. 7628–7641, 2019, ISSN: 0360-3199. DOI: https://doi.org/10.1016/j.ijhydene.2019.01.262.

[81] D. Schwer and K. Kailasanath, "Numerical investigation of the physics of rotating-detonation-engines," *Proc. Combust. Inst.*, vol. 33, no. 2, pp. 2195–2202, 2011, ISSN: 1540-7489. DOI: https://doi.org/10.1016/j.proci.2010.07.050.

[82] B. A. Rankin, J. R. Codoni, K. Y. Cho, J. L. Hoke, and F. R. Schauer, "Investigation of the structure of detonation waves in a non-premixed hydrogen-air rotating detonation engine using mid-infrared imaging," *Proc. Combust. Inst.*, vol. 37, pp. 3479–3486, 2019, ISSN: 15407489. DOI: 10.1016/j.proci.2018.09.036. [Online]. Available: https://doi.org/10.1016/j.proci.2018.09.036.

[83] H.-Y. Peng, W.-D. Liu, S.-J. Liu, H.-L. Zhang, and L.-X. Jiang, "Hydrogen-air, ethylene-air, and methane-air continuous rotating detonation in the hollow chamber," *Energy*, vol. 211, p. 118 598, 2020, ISSN: 0360-5442. DOI: https://doi.org/10.1016/j.energy.2020.118598.

[84] D. Schwer and K. Kailasanath, "Feedback into mixture plenums in rotating detonation engines," 50th AIAA Aerospace Sciences Meeting including the New Horizons Forum and Aerospace Exposition, AIAA 2012-0617, 2012. DOI: 10.2514/6.2012-617.

[85] Z. Xia, X. Tang, M. Luan, S. Zhang, Z. Ma, and J. Wang, "Numerical investigation of two-wave collision and wave structure evolution of rotating detonation engine with hollow combustor," *International Journal of Hydrogen Energy*, vol. 43, no. 46, pp. 21 582–21 591, 2018, ISSN: 0360-3199. DOI: https://doi.org/10.1016/j.ijhydene.2018.09.165.

[86] X.-Y. Liu, Y.-L. Chen, Z.-J. Xia, and J.-P. Wang, "Numerical study of the reverse-rotating waves in rotating detonation engine with a hollow combustor," *Acta Astronautica*, vol. 170, pp. 421–430, 2020, ISSN: 0094-5765. DOI: https://doi.org/10.1016/j.actaastro.2020.02.008.

[87] K. D. Rein, S. Roy, S. T. Sanders, A. W. Caswell, F. R. Schauer, and J. R. Gord, "Measurements of gas temperatures at 100 kHz within the annulus of a rotating detonation engine," *Applied Physics B: Lasers and Optics*, vol. 123, no. 3, pp. 1–9, 2017, ISSN: 09462171. DOI: 10.1007/s00340-017-6647-5.

[88] S. J. Cassady, W. Y. Peng, C. L. Strand, D. F. Dausen, J. R. Codoni, C. M. Brophy, and R. K. Hanson, "Time-resolved, single-ended laser absorption thermometry and H2O, CO2, and CO speciation in a H2/C2H4-fueled rotating detonation engine," *Proc. Combust. Inst.*, 2020, ISSN: 1540-7489. DOI: https://doi.org/10.1016/j.proci.2020.06.125.

[89] A. P. Nair, D. D. Lee, D. I. Pineda, J. Kriesel, W. A. Hargus, J. W. Bennewitz, S. A. Danczyk, and R. M. Spearrin, "MHz laser absorption spectroscopy via diplexed RF modulation for pressure, temperature, and species in rotating detonation rocket flows," *Applied Physics B*, vol. 126, no. 8, p. 138, Jul. 2020, ISSN: 1432-0649. DOI: 10.1007/s00340-020-07483-8.

[90] C. A. Fugger, J. G. Lopez, K. D. Rein, S. Roy, and A. W. Caswell, "The dynamics of a non-premixed rotating detonation engine from time-resolved temperature measurements," *Proc. Combust. Inst.*, 2020, ISSN: 1540-7489. DOI: https://doi.org/10.1016/j.proci.2020.06.373.

[91] D. Depperschmidt, R. Miller, J. Tobias, M. Uddi, A. K. Agrawal, and J. B. Stout, "Time-resolved piv diagnostics to measure flow field exiting methane-fueled rotating detonation combustor," AIAA Scitech 2019 Forum, AIAA 2019-1514, 2019. DOI: 10.2514/6.2019-1514.

[92] C. F. Lietz, Y. Desai, R. Munipalli, S. A. Schumaker, and V. Sankaran, "Flowfield analysis of a 3d simulation of a rotating detonation rocket engine," AIAA Scitech 2019 Forum, AIAA 2019-1009, 2019. DOI: 10.2514/6.2019-1009.

[93] P. A. Cocks, A. T. Holley, and B. A. Rankin, "High Fidelity Simulations of a Non-Premixed Rotating Detonation Engine," 54th AIAA Aerospace Sciences Meeting, AIAA 2016-0125, 2016. DOI: 10.2514/6.2016-0125.

[94] T. Sato and V. Raman, "Detonation structure in ethylene/air-based non-premixed rotating detonation engine," *Journal of Propulsion and Power*, vol. 36, no. 5, pp. 752–762, 2020. DOI: 10.2514/1.B37664.

[95] T. Sato, F. Chacon, L. White, V. Raman, and M. Gamba, "Mixing and detonation structure in a rotating detonation engine with an axial air inlet," *Proc. Combust. Inst.*, 2020, ISSN: 1540-7489. DOI: https://doi.org/10.1016/j.proci.2020.06.283.

[96] E. Bach, C. Oliver Paschereit, P. Stathopoulos, and M. D. Bohon, "An empirical model for stagnation pressure gain in rotating detonation combustors," *Proc. Combust. Inst.*, 2020, ISSN: 1540-7489. DOI: https://doi.org/10.1016/j.proci.2020.07.071.

[97] R. T. Fievisohn, J. Hoke, and A. T. Holley, "Equivalent Available Pressure Measurements on a Laboratory RDE," AIAA Scitech 2020 Forum, AIAA 2020-2285, 2020. DOI: 10.2514/6.2020-2285.

[98] A. Melling, "Tracer particles and seeding for particle image velocimetry," *Measurement Science and Technology*, vol. 8, no. 12, pp. 1406–1416, Dec. 1997. DOI: 10.1088/0957-0233/8/12/005.

[99] B. Wieneke, "PIV uncertainty quantification from correlation statistics," *Measurement Science and Technology*, vol. 26, no. 7, p. 074 002, Jun. 2015. DOI: 10.1088/0957-0233/26/7/074002.

[100] D. Schwer and K. Kailasanath, "Modeling exhaust effects in rotating detonation engines," 48th AIAA/ASME/SAE/ASEE Joint Propulsion Conference & Exhibit, AIAA 2012-3943, 2012. DOI: 10.2514/6.2012-3943.

[101] P. S. Addison, *The Illustrated Wavelet Transform Handbook*, 2nd. Boca Raton: CRC Press, 2017, ISBN: 9781315372556. DOI: 10.1201/9781315372556.

[102] A. Feleo, F. Chacon, and M. Gamba, "Uncertainties in Thrust and EAP Measurements of a Rotating Detonation Combustor with Axial Air Inlet," AIAA Propulsion and Energy 2020 Forum, AIAA 2020-3856, 2020. DOI: 10.2514/6.2020-3856.

[103] S. Candel, D. Durox, T. Schuller, J.-F. Bourgouin, and J. P. Moeck, "Dynamics of swirling flames," *Annual Review of Fluid Mechanics*, vol. 46, no. 1, pp. 147–173, 2014. DOI: 10.1146/annurev-fluid-010313-141300.

[104] Z. Liu, J. Braun, and G. Paniagua, "Performance of axial turbines exposed to large fluctuations," 53rd AIAA/SAE/ASEE Joint Propulsion Conference, AIAA 2017-4817, 2017. DOI: 10.2514/6.2017-4817.

[105] B. A. Rankin, M. L. Fotia, A. G. Naples, C. A. Stevens, J. L. Hoke, T. A. Kaemming, S. W. Theuerkauf, and F. R. Schauer, "Overview of performance, application, and analysis of rotating detonation engine technologies," *Journal of Propulsion and Power*, vol. 33, no. 1, pp. 131–143, Jan. 2017. DOI: 10.2514/1.b36303.

[106] A. K. Gupta and D. A. Schwer, "Rotating detonation engine concept: Direct combustion of supersonic inflow," *Journal of Propulsion and Power*, vol. 34, no. 2, pp. 562–564, Mar. 2018. DOI: 10.2514/1.b36545.

[107] S. Frolov, V. Zvegintsev, V. Ivanov, V. Aksenov, I. Shamshin, D. Vnuchkov, D. Nalivaichenko, A. Berlin, V. Fomin, A. Shiplyuk, and N. Yakovlev, "Hydrogen-fueled detonation ramjet model: Wind tunnel tests at approach air stream mach number 5.7 and stagnation temperature 1500 k," *International Journal of Hydrogen Energy*, vol. 43, no. 15, pp. 7515–7524, Apr. 2018. DOI: 10.1016/j.ijhydene.2018.02.187.

[108] T. Poinsot, "Prediction and control of combustion instabilities in real engines," *Proc. Combust. Inst.*, vol. 36, no. 1, pp. 1–28, 2017. DOI: 10.1016/j.proci.2016.05.007.

[109] C. Lietz, Y. Desai, W. A. Hargus, and V. Sankaran, "Parametric investigation of rotating detonation rocket engines using large eddy simulations," AIAA Propulsion and Energy 2019 Forum, AIAA 2019-4129, Aug. 2019. DOI: 10.2514/6.2019-4129.

[110] S. Prakash, V. Raman, C. F. Lietz, W. A. Hargus, and S. A. Schumaker, "Numerical simulation of a methane-oxygen rotating detonation rocket engine," *Proceedings of the Combustion Institute*, vol. 38, no. 3, pp. 3777–3786, 2021. DOI: 10.1016/j.proci.2020.06.288.

[111] V. Anand, A. S. George, R. Driscoll, and E. Gutmark, "Characterization of instabilities in a rotating detonation combustor," *International Journal of Hydrogen Energy*, vol. 40, no. 46, pp. 16 649–16 659, Dec. 2015. DOI: 10.1016/j.ijhydene.2015.09.046.

[112] B. R. Bigler, J. W. Bennewitz, S. A. Danczyk, and W. A. Hargus, "Rotating detonation rocket engine operability under varied pressure drop injection," *Journal of Spacecraft and Rockets*, vol. 58, no. 2, pp. 316–325, 2021. DOI: 10.2514/1.A34763.

[113] J. Koch and J. N. Kutz, "Modeling thermodynamic trends of rotating detonation engines," *Physics of Fluids*, vol. 32, no. 12, p. 126 102, 2020. DOI: 10.1063/5.0023972.

[114] J. Portillo, J. Sisco, Y. Yu, V. Sankaran, and W. Anderson, "Application of a generalized instability model to a longitudinal mode combustion instability," 43rd AIAA/ASME/SAE/ASEE Joint Propulsion Conference & Exhibit, AIAA 2007-5651, 2007. DOI: 10.2514/6.2007-5651.

[115] T. Adamson and G. Olsson, "Performance analysis of a rotating detonation wave rocket engine," *Astronautica Acta*, vol. 13, pp. 405–415, 1967.

[116] R. T. Fievisohn and K. H. Yu, "Steady-state analysis of rotating detonation engine flowfields with the method of characteristics," *Journal of Propulsion and Power*, vol. 33, no. 1, pp. 89–99, 2017. DOI: 10.2514/1.B36103.

[117] W. Fickett, "Detonation in miniature," *American Journal of Physics*, vol. 47, no. 12, pp. 1050–1059, Dec. 1979. DOI: 10.1119/1.11973.

[118] A. Majda, "A qualitative model for dynamic combustion," *SIAM Journal on Applied Mathematics*, vol. 41, no. 1, pp. 70–93, Aug. 1981. DOI: 10.1137/0141006.

[119] L. M. Faria, A. R. Kasimov, and R. R. Rosales, "Theory of weakly nonlinear self-sustained detonations," *Journal of Fluid Mechanics*, vol. 784, pp. 163–198, Nov. 2015. DOI: 10.1017/jfm.2015.577.

[120] J. Koch, M. Kurosaka, C. Knowlen, and J. N. Kutz, "Mode-locked rotating detonation waves: Experiments and a model equation," *Phys. Rev. E*, vol. 101, p. 013 106, 1 Jan. 2020. DOI: 10.1103/PhysRevE.101.013106.

[121] R. T. Fievisohn, J. Hoke, and S. A. Schumaker, "Product recirculation and incipient autoignition in a rotating detonation engine," AIAA Scitech 2020 Forum, AIAA 2020-2286, 2020. DOI: 10.2514/6.2020-2286.

[122] P. Gupta, K. S. Schwinn, G. Lodato, C. D. Slabaugh, and C. Scalo, "Numerical investigation of sustained planar detonation waves in a periodic domain," 2018 Fluid Dynamics Conference, AIAA 2018-3240, 2018. DOI: 10.2514/6.2018-3240.

[123] J. Humble, S. Sardeshmukh, and S. Heister, "Reduced order modeling of rotational detonation engines," AIAA Scitech 2019 Forum, AIAA 2019-0201, 2019. DOI: 10.2514/6.2019-0201.

[124] S. A. Zhdan, A. M. Mardashev, and V. V. Mitrofanov, "Calculation of the flow of spin detonation in an annular chamber," *Combustion, Explosion, and Shock Waves*, vol. 26, no. 2, pp. 210–214, 1990. DOI: 10.1007/bf00742414.

[125] S. A. Zhdan, F. A. Bykovskii, and E. F. Vedernikov, "Mathematical modeling of a rotating detonation wave in a hydrogen-oxygen mixture," *Combustion, Explosion, and Shock Waves*, vol. 43, no. 4, pp. 449–459, Jul. 2007. DOI: 10.1007/s10573-007-0061-y.

[126] S. A. Zhdan and A. S. Syryamin, "Numerical modeling of continuous detonation in non-stoichiometric hydrogen-oxygen mixtures," *Combustion, Explosion, and Shock Waves*, vol. 49, no. 1, pp. 69–78, Jan. 2013. DOI: 10.1134/s0010508213010085.

[127] J. Fujii, Y. Kumazawa, A. Matsuo, S. Nakagami, K. Matsuoka, and J. Kasahara, "Numerical investigation on detonation velocity in rotating detonation engine chamber," *Proceedings of the Combustion Institute*, vol. 36, no. 2, pp. 2665–2672, 2017. DOI: 10.1016/j.proci.2016.06.155.

[128] M. Zhao, M. J. Cleary, and H. Zhang, "Combustion mode and wave multiplicity in rotating detonative combustion with separate reactant injection," *Combustion and Flame*, vol. 225, pp. 291–304, Mar. 2021. DOI: 10.1016/j.combustflame.2020.11.001.

[129] J. Jiménez and P. Moin, "The minimal flow unit in near-wall turbulence," *Journal of Fluid Mechanics*, vol. 225, pp. 213–240, Apr. 1991. DOI: 10.1017/s0022112091002033.

[130] T. Sato, F. Chacon, M. Gamba, and V. Raman, "Mass flow rate effect on a rotating detonation combustor with an axial air injection," *Shock Waves*, Feb. 2021. DOI: 10.1007/s00193-020-00984-7.

[131] K. Grogan and M. Ihme, "StanShock: A gas-dynamic model for shock tube simulations with non-ideal effects and chemical kinetics," *Shock Waves*, vol. 30, no. 4, pp. 425–438, Jan. 2020. DOI: 10.1007/s00193-019-00935-x.

[132] R. W. Houim and K. K. Kuo, "A low-dissipation and time-accurate method for compressible multi-component flow with variable specific heat ratios," *Journal of Computational Physics*, vol. 230, no. 23, pp. 8527–8553, Sep. 2011. DOI: 10.1016/j.jcp.2011.07.031.

[133] D. G. Goodwin, R. L. Speth, H. K. Moffat, and B. W. Weber, *Cantera: An object-oriented software toolkit for chemical kinetics, thermodynamics, and transport processes*, https://www.cantera.org, Version 2.5.1, 2021. DOI: 10.5281/zenodo.4527812.

[134] H. Wu, P. C. Ma, and M. Ihme, "Efficient time-stepping techniques for simulating turbulent reactive flows with stiff chemistry," *Computer Physics Communications*, vol. 243, pp. 81–96, Oct. 2019. DOI: 10.1016/j.cpc.2019.04.016.

[135] L. D. Dalcin, R. R. Paz, P. A. Kler, and A. Cosimo, "Parallel distributed computing using python," *Advances in Water Resources*, vol. 34, no. 9, pp. 1124–1139, Sep. 2011. DOI: 10.1016/j.advwatres.2011.04.013.

[136] G. Smith, Y. Tao, and H. Wang, *Foundational fuel chemistry model version 1.0 (ffcm-1)*, http://nanoenergy.stanford.edu/ffcm1, 2016.

[137] J. Greenough and W. Rider, "A quantitative comparison of numerical methods for the compressible euler equations: Fifth-order WENO and piecewise-linear godunov," *Journal of Computational Physics*, vol. 196, no. 1, pp. 259–281, May 2004. DOI: 10.1016/j.jcp.2003.11.002.

[138] X. Shi, J. Crane, and H. Wang, "Deflagration-to-detonation transition inside reactant-product mixing layers," AIAA Scitech 2021 Forum, AIAA 2021-1147, 2021. DOI: 10.2514/6.2021-1147.

[139] M. I. Radulescu, "A detonation paradox: Why inviscid detonation simulations predict the incorrect trend for the role of instability in gaseous cellular detonations?" *Combustion and Flame*, vol. 195, pp. 151–162, Sep. 2018. DOI: 10.1016/j.combustflame.2018.05.002.

VITA

Ian Vincent Walters was born March 20, 1994 to Janice and John Walters. He earned an Honors Bachelor of Science degree in Mechanical Engineering from Oregon State University in 2016, where he researched turbulent Bunsen flames under the direction of Dr. David Blunck. He began graduate studies in Aeronautical and Astronautical Engineering with a focus in propulsion that same year at Purdue University. He worked with Dr. Carson Slabaugh on the research and development of rotating detonation engines in pursuit of a doctorate. Ian is married to Madeline Walters.

PUBLICATIONS

Journal

- Ian Walters, Christopher Journell, Aaron Lemcherfi, Rohan Gejji, Stephen Heister, and Carson Slabaugh, "Operability of a Natural Gas-Air Rotating Detonation Engine," Journal of Propulsion and Power, 2020
- Ian Walters, Aaron Lemcherfi, Rohan Gejji, Stephen Heister, and Carson Slabaugh, "Performance Characterization of a Natural Gas-Air Rotating Detonation Engine," Journal of Propulsion and Power, 2021
- Ian Walters, Rohan Gejji, Stephen Heister, and Carson Slabaugh, "Flow and Performance Analysis of a Natural Gas-Air Rotating Detonation Engine with High-Speed Velocimetry," Combustion and Flame, (Accepted)
- Christopher Journell, Rohan Gejji, Ian Walters, Aaron Lemcherfi, Carson Slabaugh, and Jeffrey Stout, "High Speed Diagnostics in a Natural Gas-Air Rotating Detonation Engine," Journal of Propulsion and Power, 2020

Conference

- Ian Walters, Christopher Journell, Aaron Lemcherfi, Rohan Gejji, Stephen Heister, and Carson Slabaugh, "Experimental Investigation of a Piloted, Natural Gas-Air Rotating Detonation Wave Combustor," AIAA Propulsion & Energy Forum, 2018
- Ian Walters, Christopher Journell, Aaron Lemcherfi, Rohan Gejji, Stephen Heister, and Carson Slabaugh, "Parametric Survey of a Natural Gas-Air Rotating Detonation Engine at Elevated Pressure," AIAA SciTech, 2019
- Ian Walters, Christopher Journell, Aaron Lemcherfi, Rohan Gejji, Stephen Heister, and Carson Slabaugh, "Performance Characterization of a Natural Gas-Air Rotating Detonation Engine," AIAA Propulsion & Energy Forum, 2019